



NATIONAL AND KAPODISTRIAN UNIVERSITY OF ATHENS

**SCHOOL OF SCIENCE
DEPARTMENT OF INFORMATICS AND TELECOMMUNICATIONS**

**MASTER'S PROGRAM IN
MICROELECTRONICS**

MASTER'S THESIS

**Simulation of surface charging during plasma etching
of dielectric microstructures**

Georgios K. Memos

Supervisor: George Kokkoris, Research Fellow, NCSR "Demokritos"

ATHENS

JANUARY 2014



ΕΘΝΙΚΟ ΚΑΙ ΚΑΠΟΔΙΣΤΡΙΑΚΟ ΠΑΝΕΠΙΣΤΗΜΙΟ ΑΘΗΝΩΝ

**ΣΧΟΛΗ ΘΕΤΙΚΩΝ ΕΠΙΣΤΗΜΩΝ
ΤΜΗΜΑ ΠΛΗΡΟΦΟΡΙΚΗΣ ΚΑΙ ΤΗΛΕΠΙΚΟΙΝΩΝΙΩΝ**

**ΔΙΑΤΜΗΜΑΤΙΚΟ ΠΡΟΓΡΑΜΜΑ ΜΕΤΑΠΤΥΧΙΑΚΩΝ ΣΠΟΥΔΩΝ ΣΤΗ
ΜΙΚΡΟΗΛΕΚΤΡΟΝΙΚΗ**

ΔΙΠΛΩΜΑΤΙΚΗ ΕΡΓΑΣΙΑ

**Προσομοίωση του φαινόμενου επιφανειακής
φόρτισης κατά την εγχάραξη διηλεκτρικών
μικροδομών με πλάσμα**

Γεώργιος Κ. Μέμος

**Επιβλέπων: Γεώργιος Κόκκορης, Συνεργαζόμενος Ερευνητής,
ΕΚΕΦΕ "Δημόκριτος"**

ΑΘΗΝΑ

ΙΑΝΟΥΑΡΙΟΣ 2014

MASTER'S THESIS

Simulation of surface charging during plasma etching of dielectric microstructures

Georgios K. Memos
R.N.: MM196

SUPERVISOR: **George Kokkoris**, Research fellow, NCSR "Demokritos"

EXAMINING COMMITTEE:

- **Angeliki Arapoyanni**, Professor, Department of Informatics and Telecommunications, N.K.U.A
- **Evangelos Gogolides**, Director of Research, N.C.S.R. "Demokritos"
- **Angeliki Tserepi**, Director of Research, N.C.S.R. "Demokritos"
- **Vassilios Constantoudis**, Researcher, N.C.S.R. "Demokritos"
- **George Kokkoris**, Research fellow, N.C.S.R. "Demokritos"

JANUARY 2014

ΔΙΠΛΩΜΑΤΙΚΗ ΕΡΓΑΣΙΑ

Προσομοίωση του φαινομένου επιφανειακής φόρτισης
κατά την εγχάραξη διηλεκτρικών μικροδομών με πλάσμα

Γεώργιος Κ. Μέμος
Α.Μ.: MM196

ΕΠΙΒΛΕΠΩΝ: **Γεώργιος Κόκκορης**, Συνεργαζόμενος Ερευνητής,
ΕΚΕΦΕ "Δημόκριτος"

ΕΞΕΤΑΣΤΙΚΗ ΕΠΙΤΡΟΠΗ:

- **Αγγελική Αραπογιάννη**, Καθηγήτρια, Τμήμα Πληροφορικής και Τηλεπικοινωνιών, ΕΚΠΑ
- **Ευάγγελος Γογγολίδης**, Διευθυντής Ερευνών, ΕΚΕΦΕ "Δημόκριτος"
- **Αγγελική Τσερέπη**, Διευθύντρια Ερευνών, ΕΚΕΦΕ "Δημόκριτος"
- **Βασίλειος Κωνσταντούδης**, Ερευνητής, ΕΚΕΦΕ "Δημόκριτος"
- **Γεώργιος Κόκκορης**, Συνεργαζόμενος Ερευνητής, ΕΚΕΦΕ "Δημόκριτος"

ΙΑΝΟΥΑΡΙΟΣ 2014

ABSTRACT

When the plasma etching of a dielectric trench takes place, the trench sidewalls restrict the flux of the isotropic electrons to the upper parts of sidewalls; due to electron shadowing only a small fraction of electrons reach the trench bottom. Simultaneously, due to their anisotropy, (positive) ions accumulate at the trench bottom. Positive charge will continue to build up until the bottom dielectric surface obtains a potential large enough to repel a sufficient number of ions. This is because the ion and electron currents to the bottom surface of the microstructure must balance at the steady state. Owing to the electrostatic repulsion, ultimately, a vast amount of ions impinge at the trench sidewall surface or even return to the plasma bulk. This phenomenon, known as microstructure charging, can lead to profile irregularities during etching, electrostatic etch stop or even oxide degradation and breakdown.

The aim of this work is the development and implementation of a model for the simulation of surface charging on plasma "wetted" 2-dimensional (2d) microstructures. The algorithm is applied to the investigation of the charging in dielectric trenches. The impact of charging under different conditions and cases is investigated. In particular, the effect of a) the shape of the ion energy distribution function (IEDF), b) the average ion energy, c) the electron temperature (T_e), and d) the aspect ratio (AR) of the feature on the local ion fluxes, etching yields, and rates is examined.

The charging simulation model consists of three sub-models. The first sub-model is the particle trajectories calculation model where the ion and electron trajectories are calculated by solving Newton equations of motion. In the second sub-model, the surface charge density on the dielectric trench is calculated. The third sub-model is the charging potential model and includes the calculation of the space potential and electric field induced by the surface charging. The space potential and electric field is not only affected by the surface charge but it also affects it: the electric force coming from the field affects the trajectory calculation in the first sub-model. A sequential solution of the three sub-models, i.e. a charging step, is performed for several times until the steady state (current balance at the bottom) is achieved. A number of equal number of ions and electrons are released at each charging step.

A Matlab code is developed for the first and second sub-models. The computations in the third sub-model are realized by Comsol Multiphysics 4.3b. During the repetitive charging process, all models cooperate with each other through the Matlab programming environment.

Summarizing the basic results of the calculations, a narrower IEDF, a smaller average ion energy, a greater T_e , and a greater trench AR leads to a smaller ion flux and etching rate at the trench bottom.

SUBJECT AREA: Plasma etching

KEY WORDS: charging, electron shadowing, dielectric trench , particle trajectories, Laplace equation, numerical simulation

ΠΕΡΙΛΗΨΗ

Κατά την εγχάραξη αυλακιού από διηλεκτρικό υλικό με πλάσμα, η σκίαση της ιστροπικής ροής των ηλεκτρονίων μειώνει σημαντικά το πλήθος αυτών που φτάνουν στον πυθμένα του αυλακιού. Ταυτόχρονα, λόγω της ανισοτροπίας της ροής τους, τα (θετικά) ιόντα συσσωρεύονται στον πυθμένα του αυλακιού. Η συσσώρευση θετικού φορτίου στον πυθμένα του αυλακιού συνεχίζεται μέχρι το θετικό δυναμικό να μπορεί να απωθεί τον απαιτούμενο αριθμό ιόντων ώστε οι ροές των ηλεκτρονίων και των ιόντων να είναι ίσες. Λόγω της ηλεκτροστατικής απώθησης, τα ιόντα προσπίπτουν στα τοιχώματα του αυλακιού ή επιστρέφουν στον κύριο όγκο του πλάσματος. Το φαινόμενο αυτό, γνωστό ως φαινόμενο φόρτισης κατά την εγχάραξη μικροδομών μπορεί να οδηγήσει σε αποκλίσεις από το συνήθως επιθυμητό ορθογωνικό προφίλ, σε παύση της εγχάραξης ή ακόμα και σε κατάρρευση του διηλεκτρικού.

Ο στόχος της εργασίας είναι η ανάπτυξη μοντέλου προσομοίωσης του φαινομένου επιφανειακής φόρτισης κατά την εγχάραξη δισδιάστατων (2D) μικροδομών με πλάσμα. Για την διερεύνηση του φαινομένου, το μοντέλο εφαρμόζεται στην εγχάραξη αυλακιού από διηλεκτρικό. Εξετάζεται η επίδραση της φόρτισης για διάφορες συνθήκες και περιπτώσεις. Συγκεκριμένα, εξετάζεται η επίδραση α) της ενεργειακής κατανομής και β) της μέσης ενέργειας των ιόντων, γ) της θερμοκρασίας των ηλεκτρονίων και δ) του λόγου ασυμμετρίας (ΛΑ) του αυλακιού (βάθος/πλάτος αυλακιού) στην τοπική ροή των ιόντων καθώς και στον τοπικό ρυθμό εγχάραξης στην επιφάνεια του αυλακιού.

Το μοντέλο αποτελείται από 3 υπο-μοντέλα. Στο πρώτο υπο-μοντέλο υπολογίζονται οι τροχιές των ιόντων και των ηλεκτρονίων με την επίλυση των εξισώσεων κίνησης του Νεύτωνα. Στο δεύτερο υπο-μοντέλο υπολογίζεται η επιφανειακή πυκνότητα φορτίου στη μικροδομή (αυλάκι). Το τρίτο υπο-μοντέλο περιλαμβάνει τον υπολογισμό του ηλεκτρικού δυναμικού στο εσωτερικό του αυλακιού. Το δυναμικό αυτό είναι αποτέλεσμα του συσσωρευμένου φορτίου στην επιφάνεια του αυλακιού. Το ηλεκτρικό δυναμικό όχι μόνο επηρεάζεται από το επιφανειακό φορτίο αλλά ταυτόχρονα το επηρεάζει: Η ηλεκτρική δύναμη που απορρέει από το προκύπτον ηλεκτρικό πεδίο επηρεάζει τις τροχιές των φορτισμένων σωματιδίων στο πρώτο υπο-μοντέλο. Η διαδοχική επίλυση των τριών υπο-μοντέλων πραγματοποιείται επανειλημμένα έως ότου επιτευχθεί μόνιμη κατάσταση δηλαδή εξίσωση ροών ιόντων και ηλεκτρονίων στον πυθμένα του αυλακιού.

Τα δύο πρώτα υπο-μοντέλα αναπτύχθηκαν σε κώδικα Matlab και το τρίτο υλοποιήθηκε με τον εμπορικό κώδικα Comsol Multiphysics 4.3b. Τα υπο-μοντέλα επικοινωνούν με κώδικα Matlab.

Συνοψίζοντας τα βασικά αποτελέσματα της μελέτης, μικρότερο εύρος στην ενεργειακή κατανομή των ιόντων, μικρότερη μέση ενέργεια ιόντων, μεγαλύτερη θερμοκρασία ηλεκτρονίων και μεγαλύτερος ΛΑ οδηγεί σε μείωση της ροής των ιόντων και του ρυθμού εγχάραξης στον πυθμένα του αυλακιού.

ΘΕΜΑΤΙΚΗ ΠΕΡΙΟΧΗ: Εγχάραξη με πλάσμα

ΛΕΞΕΙΣ ΚΛΕΙΔΙΑ: φόρτιση, σκίαση, διηλεκτρικό αυλάκι, τροχιές σωματιδίων εξίσωση Laplace, αριθμητική προσομοίωση

CONTENTS

PROLOGUE	19
1. INTRODUCTION.....	20
1.1 The plasma state.....	20
1.2 Plasma etching in the industry.....	21
1.2.1 Introduction.....	21
1.2.2 The plasma reactor	22
1.2.3 Mechanisms of plasma etching.....	24
1.3 Microstructure charging: origin and effects.....	26
1.4 Previous works on microstructure charging	28
1.5 The aim and the structure of this work.....	31
2. THE ORIGIN OF MICROSTRUCTURE CHARGING.....	33
2.1 Introduction	33
2.2 Ion and electron dynamics in an RF sheath	33
2.2.1 Why RF plasma?.....	33
2.2.2 The mathematical expression of the RF self bias	37
2.3 The directionality difference between ions and electron fluxes at the wafer	39
2.4 Electron shadowing effect.....	42
3. THE DESCRIPTION OF THE MODEL.....	44
3.1 Introduction.....	44
3.2 Particle trajectories calculation model.....	47
3.2.1 The acceptance-rejection method.....	47
3.2.1.1 Introduction	47
3.2.1.2 The algorithm of the acceptance-rejection method	47
3.2.2 Ion energy and angular distribution function	49
3.2.2.1 introduction. Why a bimodal ion energy distribution function (IEDF)?.....	49
3.2.2.2 Ion velocities at the inlet of the domain	52
3.2.2.3 Electron velocities at the inlet of the domain.....	56
3.2.3 Ion and electron trajectories simulation.....	59
3.2.4 The utility of superparticles	64
3.3 Surface charge density calculation model.....	65
3.3.1 Particle distribution on the down boundary.....	65
3.3.1.1 Introduction	65
3.3.1.2 The segmentation of the boundary.....	65

3.3.1.3 The particle distribution algorithm.....	66
3.3.1.3 The particle distribution algorithm.....	66
3.3.2.1 Using linear instead of surface charge density.....	67
3.3.2.2 The method of calculation.....	68
3.4 Charging potential calculation model.....	68
3.4.1 Imposing the proper boundary conditions.....	68
3.4.2 The mesh of the simulation domain.....	72
3.5 Computational cost and parallel implementation.....	73
4. VERIFICATION AND RESULTS	74
4.1 Introduction.....	74
4.2 Conditions, inputs and post data process of the simulation.....	74
4.3 Verification of the model.....	75
4.3.1 Comparison with Hwang and Giapis work.....	75
4.3.2 Self-consistency check.....	79
4.3.2.1 Aspect ratio dependent charging.....	79
4.3.2.2 The effect of the simulation randomness on the results.....	81
4.3.3 The effect of the inlet position on the charging process.....	82
4.4 The effect of the IEDF shape on microstructure charging.....	83
4.5 The effect of the average ion energy on the microstructure charging	
.....	89
4.6 The effect of the electron temperature on microstructure charging	94
4.7 The effect of the aspect ratio on microstructure charging.....	99
5. CONCLUSIONS AND FUTURE WORKS	107
APPENDIX I	112
APPENDIX II	115
APPENDIX III.....	117
APPENDIX IV	120
APPENDIX V	122
REFERENCES	125

TABLE OF FIGURES

Figure 1.2: Range of temperature, electron density, and Debye length for typical plasmas in nature and in technological applications. It should be mentioned that only states to the left of the quantum degeneracy line are considered plasmas and can be treated with formulations from classical physics. Reproduced from [5]21

Figure 1.3: The number of transistor per IC for various microprocessors versus their release date [6]. The fact that transistors per IC is growing exponential (Moore's Law) is more than evident.....22

Figure 1.4: Sketch of a parallel plate triode plasma etcher [8]. The typical processes that take place both in the bulk of the plasma and the wafer are shown [3].23

Figure 1.5: Coburn and Winters measured silicon etching rate under independent and concurrent exposure to XeF₂ gas and 450 eV Ar⁺ ion beams. They observed that the etching rate under simultaneous exposure to both the beams was nearly six times the sum of the etch rates under exposure to the individual beams. Taken from [10].....25

Figure 1.6: Microstructure charging process. High aspect ratio microstructures receive reduced electron flux at the lower trench sidewalls and bottom due to shadowing effects. For the case of insulating materials in either of these regions, surface charging phenomena can result [11].26

Figure 1.7: The simulation domain used by Kinoshita et al. [24]......29

Figure 2.1: Schematic of electrode configuration for an RF glow discharge. An RF power supply is capacitively coupled to the electrodes. Taken from [43]35

Figure 2.2: a) Electrode's voltage and current waveforms when the circuit of figure is squared wave excited. b) On each half cycle, the current decays as the capacitor charges from the plasma. Taken from [43].35

Figure 2.3: Self bias and DC offset of a sine wave driven system. The RF signal is superimposed on the RF self bias level. Taken from [43]36

Figure 2.4: Floating potential for a sinusoidally modulated sheath in an Ar plasma; the floating potential approaches the RF amplitude V_1 at high bias

while at very low bias the RF self bias becomes negligible and the floating potential approaches the DC value. Reproduced from [45].39

Figure 2.5: Depiction of the electron and ion angular distribution functions at the sheath edge and at the unpatterned wafer surface. The anisotropy of both distributions is evident. Nonetheless, ions are much more directional than electrons. The part of the electron angular distribution that will arrive at the wafer surface is denoted by ϕ . [18].....41

Figure 2.6: (a) Ion (Cl^+) and (b) electron distribution angular distribution at the sheath lower boundary as calculated by Hwang and Giapis [12]......41

Figure 2.7: Depiction of the difference in the degree of anisotropy between ions and electrons. Almost all of the ions arrive at the segment ΔS at angles of incidence smaller than a few degrees from normal, while the majority of the electrons impinge at angles that deviate significantly from $\theta = 0^\circ$. The dashed-line arrows describe electron flux while the solid-line arrows depict ion flux. Decreasing length of the dashed lines indicates smaller electron flux. Taken from [18]......42

Figure 2.8: Schematic illustration of steady-state current balances at an insulating surface segment next to a single insulating feature of rectangular cross section. The dashed-line arrows describe electron flux while the solid-line arrows depict ion flux. Decreasing length of the dashed lines indicates smaller electron flux. The ion and electron fluxes are not to scale. Taken from [18]42

Figure 2.9: Schematic illustration of steady-state current balances at an insulating surface segment confined by two insulating features, forming a trench. The dashed-line arrows describe electron flux while the solid-line arrows depict ion flux. Decreasing length of the dashed lines indicates smaller electron flux. Taken from [18].43

Figure 3.1: Schematic of the simulator algorithm.44

Figure 3.2: The simulation domain.45

Figure 3.3: application of acceptance-rejection method on an arbitrary pdf. The rejection of a sample is denoted with the symbol x . The Y random numbers are generated from a uniform distribution on the interval $[0,100]$49

Figure 3.4: A bimodal IEDF. The two peaks in the distribution correspond to the minimum and maximum sheath drops i.e. where the voltage is most slowly varying. Taken from [53].51

Figure 3.5: (a) The trajectories of two ions in a DC sheath, the second one is shifted in time crossing into the sheath at some later time. The rapid steepening of the curves indicates acceleration. (b) and (c) Schematic ion trajectories in temporally modulated sheaths, $\omega \sim \omega_{pi}$ and $\omega \gg \omega_{pi}$ respectively. In both cases, the ions are being repeatedly overtaken by the oscillating sheath. In the latter case the ion motion in this regime is effectively governed by the average fields (see section 2.2) so that the trajectories closely resemble those of a steady sheath. Reproduced from [45]......52

Figure 3.6: Depiction of the curve that corresponds to the theoretical pdf of ion energy, superimposed on the probability density histogram of the generated random numbers.....53

Figure 3.7: The curve that corresponds to the theoretical pdf of ion angular distribution, superimposed on the probability density histogram of the generated random numbers.....54

Figure 3.8: IEADF, coming from equations 3.14, 3.15, and 3.16.55

Figure 3.9: The probability density histogram corresponding to the IEADF of figure 3.8. The sampling is implemented by the acceptance-rejection method. 1000 samples were used.55

Figure 3.10: Depiction of the curve that corresponds to the theoretical pdf of electron energy, superimposed on the probability density histogram of the generated random numbers.....57

Figure 3.11: The curve that corresponds to the theoretical pdf of electron angular distribution, superimposed on the probability density histogram of the generated random numbers.....58

Figure 3.12: The EEADF, coming from the equation 3.21, 3.22 and 3.24.....58

Figure 3.13: Depiction of the probability density histogram corresponding to the above mentioned EEADF. The sampling is implemented by the acceptance-rejection method. 1000 samples were used.59

Figure 3.14: Signed distance from a trench boundary61

Figure 3.15: Calculated trajectories of ions starting at the inlet, after steady state has been reached.62

Figure 3.16: Calculated trajectories of electrons starting at the inlet, after steady state has been reached. Some electrons come from the side boundaries due to particle continuity.....	63
Figure 3.17: Potential distribution map at steady state charging. Notice how the most positive and negative regions influence ions and electrons respectively in regard to figures 3.15 and 3.16.	63
Figure 3.18: Generating equal and equidistant segments across the arc length of the boundary. These segments will be utilized for the distribution of the particles on the boundary. It should be mentioned that in the above picture, for the coordinates extraction a coarse mesh was used so that the distinguish between coordinates and limits of the segments be illustrative. During the simulation process, a extremely dense mesh is used.	66
Figure 3.19: Charge distribution at the bottom of a random 2d trench.	67
Figure 3.20: Ensuing charge distribution at the bottom of the aforementioned 2d trench when extending to 3 dimensions. The length of the out of plane thickness is indicative. The result is the same for any value. The shape of the charge function is random.....	68
Figure 3.21: Boundary conditions imposed on the entire simulation domain.	70
Figure 3.22: the electric displacement field always undergoes a discontinuity when you cross a surface charge σ . [55]	70
Figure 3.23: example of the electrostatic potential evolution during sequential charging steps. Results are obtained from comsol multiphysics software 4.3b.	71
Figure 3.24: A triangulation of the simulation domain consisting of 13600 triangular elements. This triangulation was created using Comsol Multiphysics 4.3b.....	72
Figure 3.25: Parallel and sequential computation time comparison.	73
Figure 4.1: The geometry that determines the simulation domain of the model.	74
Figure 4.2: The initial IEDF that Hwang and Giapis used in their charging simulation process [15].	76
Figure 4.3: Charging potential distributions along the trench surface at AR (1.5:0.5). The length scales have been normalized by the length of the top segment in order to facilitate comparisons. Inset at the left top: The top,	

sidewall, and bottom segments of the trench arclength are denoted by a, b, and c.....	76
Figure 4.4: The energy distribution of ions arriving at the trench bottom. In our simulation, due to the lower steady state potential, the maximum is displaced to a higher energy.....	77
Figure 4.5: Charging potential distributions along the trench surface at AR (1.5:0.5). A narrow IADF has been used. The length scales have been normalized by the length of the top segment in order to facilitate comparisons. Inset at the left top: The top, sidewall, and bottom segments of the trench arclength are denoted by a, b, and c.....	78
Figure 4.6: The energy distribution of ions arriving at the trench bottom. The utilization of a narrow IADF, leads to a better agreement.	78
Figure 4.7: Charging potential distributions along the trench surface as a function of the trench width at constant AR that is equal to 3. Surface currents [15, 32] or sidewalls conductivity [16] are neglected. Obviously, ARDE holds.	80
Figure 4.8: The energy distribution of ions arriving at the trench bottom as a function of the trench width (a) 0.5 μm and (b) 0.3 μm at constant AR (3).Apparently, etching rate does not change for microstructures of same AR, irrespective of the absolute feature size.....	80
Figure 4.9: Charging potential distribution along the trench surface for two different runs conducted under the same conditions.....	81
Figure 4.10: The energy distribution of ions arriving at the trench bottom for two different runs conducted under the same conditions.	82
Figure 4.11: Charging potential distributions along the trench surface as a function of the inlet position.	83
Figure 4.12: the four different energy distributions that are utilized in the charging process. Their common feature is the average ion energy which is equal to 70eV.....	84
Figure 4.13: Charging potential distributions along the trench surface as a function of the IEDF shape.	85
Figure 4.14: Normalized local ion fluxes along the trench surface as a function of IEDF shape. The flux in the case of no charging is also depicted. Charging has a severe impact on the ion flux. Namely, 60% of the ions that would reach	

trench bottom without charging, is repulsed either out of the trench or towards the sidewalls by the steady state potential. For that reason, ion flux is increased approximately by 10% to the sidewalls for all cases. Inset at the left top: the trench arclength. Inset at the left top: The top, sidewall, and bottom segments of the trench arclength are denoted by a, b, and c.86

Figure 4.15: Normalized local electron fluxes along the trench surface as a function of IEDF shape. The no charging case flux is also depicted. Charging has a quite important impact on the electron flux. Electron shadowing seems to be restricted if a positive potential exists. Indeed, the electron flux is increased at the trench bottom and simultaneously is reduced at the sidewalls due to attraction. However, the change in the IEDF shape seems to leave the electron flux unaffected.86

Figure 4.16: The energy distribution of ions arriving at the trench bottom as a function of the initial IEDF shape. The narrower the initial IEDF is, the less energetic the impinging ions at the trench bottom will be.87

Figure 4.17: Normalized etching yield along the surface of structure as a function of the IEDF shape. The respective no charging cases are also depicted.88

Figure 4.18: Normalized etching rate along the surface of structure as a function of the IEDF shape. The respective no charging cases are also depicted.88

Figure 4.19: the three different energy distributions that are utilized in the charging process. The average ion energy is gradually increased (70eV,120eV,180eV).89

Figure 4.20: Charging potential distributions along the trench surface as a function of the ion average energy.90

Figure 4.21: Normalized local ion fluxes along the trench surface as a function of the ion average energy. The flux in the case of no charging is also depicted. As the energy grows, the total ion flux augments. The system's delay to stabilize ion and electron fluxes is responsible for this fact.91

Figure 4.22: Normalized local electron fluxes along the trench surface as a function of ion average energy. The flux in the case of no charging is also depicted. As the energy grows, the total electron flux augments. The system's delay to stabilize ion and electron fluxes is responsible for this fact.91

Figure 4.23: The evolution of the normalized ion and electron fluxes to the bottom SiO₂ surface of the trench during the charging process. During steady state, the fluctuations in the fluxes are a result of the stochastic nature of the process. The average steady-state charging potentials are insensitive to such small fluctuations.92

Figure 4.24: The energy distribution of ions arriving at the trench bottom as a function of the ion average energy. The smaller the ion average energy is, the less energetic the impinging ions at the trench bottom will be.92

Figure 4.25: Normalized etching yield along the surface of the structure as a function of the ions average energy . The no charging respective cases are also depicted.....93

Figure 4.26: Normalized etching rate along the surface of structure as a function of the IEDF shape. The no charging respective cases are also depicted.93

Figure 4.27: The corresponding electron energy distribution function (EEDF) for various electron temperatures, as indicated.94

Figure 4.28: Charging potential distributions along the trench surface as a function of the electron temperature.95

Figure 4.29: The evolution of the normalized ion and electron fluxes to the bottom SiO₂ surface of the trench during the charging process. During steady state, the fluctuations in the fluxes are a result of the stochastic nature of the process. The average steady-state charging potentials are insensitive to such small fluctuations.95

Figure 4.30: Normalized local ion fluxes along the trench surface as a function of the electron temperature. The flux in the case of no charging is also depicted. As the electron temperature grows, the total ion flux decreases. The electron flux decline due to the enlargement of the negative entrance potential is responsible for this fact.96

Figure 4.31: As the electron temperature grows, the total electron flux lessens. The more energetic electrons enhance electron shadowing effect. .97

Figure 4.32: The energy distribution of ions arriving at the trench bottom as a function of the electron temperature. The larger the electron temperature is, the less energetic the impinging ions at the trench bottom will be.97

Figure 4.33: Normalized etching yield along the surface of structure as a function of the electron temperature. The respective no charging cases are also depicted.....	98
Figure 4.34: Normalized etching rate along the surface of structure as a function of the electron temperature. The respective no charging cases are also depicted.....	98
Figure 4.35: Charging potential distributions along the trench surface as a function of the trench AR. The length scales have been normalized by the length of the top segment of AR=3 case in order to facilitate comparisons. ..	99
Figure 4.36: The potential distribution along the line connecting the top corners of the sidewalls. The trench width is 0.5 μ m in all cases. It starts at 0.875 μ m and ends at 1.375 μ m.	100
Figure 4.37: The evolution of the normalized ion and electron fluxes to the bottom SiO ₂ surface of the trench during the charging process. During steady state, the fluctuations in the fluxes are a result of the stochastic nature of the process. The average steady-state charging potentials are insensitive to such small fluctuations.	101
Figure 4.38: Normalized local ion and electron fluxes along the trench surface for the AR=1 case. The fluxes in the case of no charging is also depicted. .	101
Figure 4.39: Normalized local ion and electron fluxes along the trench surface for the case of AR=3. The fluxes in the case of no charging is also depicted.	102
Figure 4.40: Normalized local ion and electron fluxes along the trench surface for the case of AR=5. The fluxes in the case of no charging is also depicted.	102
Figure 4.41: The energy distribution of ions arriving at the trench bottom as a function of the AR. The larger the AR is, the less energetic the impinging ions at the trench bottom will be.	103
Figure 4.42: Normalized etching yield along the surface of structure for the AR=1 case. The respective no charging case is also depicted.....	104
Figure 4.43: Normalized etching rate along the surface of structure for the AR=1 case. The respective no charging case is also depicted.....	104
Figure 4.44: Normalized etching yield along the surface of structure for the AR=3 case. The respective no charging cases is also depicted.	105

Figure 4.45: Normalized etching yield along the surface of structure for the AR=3 case. The no charging respective case is also depicted.	105
Figure 4.46: Normalized etching yield along the surface of structure for the AR=5 case. The no charging respective case is also depicted.	106
Figure 4.47: Normalized etching yield along the surface of structure for the AR=5 case. The no charging respective case is also depicted.	106
Figure 5.1: Average potential at the trench bottom as a function of the IEDF shape	107
Figure 5.2: Average ER (normalized with respect to the value at open area) at the trench bottom as a function of the IEDF shape.	108
Figure 5.3: Average potential at the trench bottom as a function of the average ion energy.	108
Figure 5.4: Average ER (normalized with respect to the value at open area) at the trench bottom as a function of the average ion energy.	109
Figure 5.5: Average potential and at the trench bottom as a function of T_e	109
Figure 5.6: Average ER (normalized with respect to the value at open area) at the trench bottom as a function of T_e	110
Figure 5.7: a) Average potential at the trench bottom as a function of the AR.	110
Figure 5.8: average ER (normalized with respect to the value at open area) at the trench bottom as a function of the AR.	111

TABLE OF IMAGES

Image 1.1: Example of plasma. (a) Coronal loops filled with hot plasma that emits in the soft X-ray regime. Observed at 17.1 nm wavelength by the Transition Region and Coronal Explorer (TRACE) satellite [2]. (b) Inductively coupled plasma reactor for microfabrication processing (Institute of Advanced Materials, Physicochemical Processes, Nanotechnology, and Microsystems, Department of Microelectronics, National Center for Scientific Research Demokritos) [3].....	20
Image 1.2: (a) Example of the notch which is the opening of a narrow groove in a conductive material at the interface with an underlying insulator. Taken from reference [20]. (b) Experimental results from Oxford Instruments Plasma technology, reproduced from the paper of Ishchuk et al. [19].	27
Image 1.3: (a) Microtrenching profile due to the differential charging mechanism in the absence of a magnetic field. The local electric fields in the feature deflect ions from the centre towards the negatively charged sidewalls, resulting in symmetric microtrenching. (b) Schematic view of differential charging in the presence of a magnetic field. The Lorentz force F_L deflects electrons, resulting in an asymmetric electron angular distribution, resulting in asymmetric microtrenching. See reference [21] for more details.	27
Image 1.4: As the (a) SiO ₂ and (b) Si ₃ N ₄ trenches become deeper, the differences in trench depths of the 2 μm and 7 μm wide trenches become more obvious due to RIE lag [23].....	28

PROLOGUE

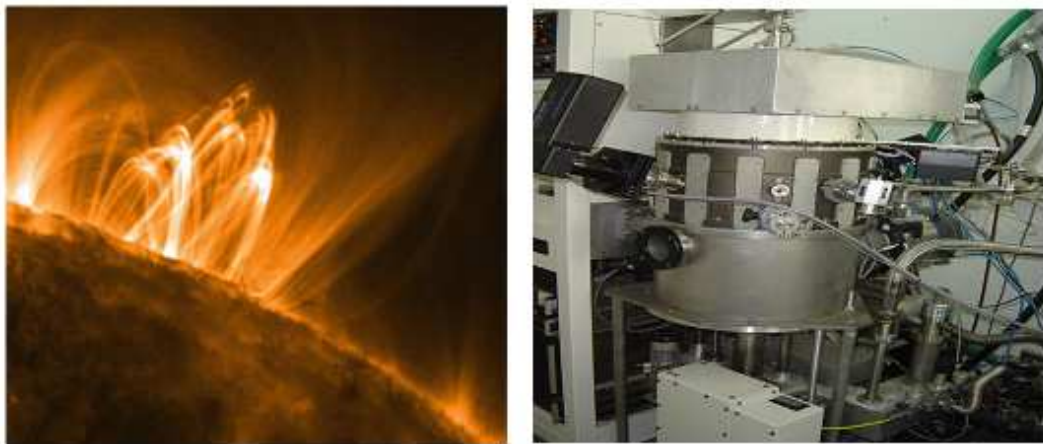
This thesis was held at the Department of Microelectronics or the Institute of Advanced Materials, Physicochemical Processes, Nanotechnology & Microsystems of NCSR Demokritos during the joint master's program in Microelectronics of the National and Kapodistrian University of Athens with NCSR Demokritos, the Institute National Polytechnique De Grenoble, and the Institute of Communication and Computer Systems of the National Technical University of Athens.

I would like to thank my supervisor, Dr. George Kokkoris. Without his great help, the completion of this work would not have been possible. I would also like to thank my family for their support and encouragement. Finally, I dedicate this work to Katerina.

1 INTRODUCTION

1.1 The plasma state

Plasma is a gaseous mixture of positive ions and electrons. Plasmas can be fully ionized, as the plasma of the Sun, or partially ionized, as the plasma reactors that are used in microfabrication. Specifically, the plasma which is useful to ultra large scale integration (ULSI) processing is a weakly ionized plasma, i.e. a plasma where the ionization fraction is less than 1% [1].



(a)

(b)

Image 1.1: Example of plasma. (a) Coronal loops filled with hot plasma that emits in the soft X-ray regime. Observed at 17.1 nm wavelength by the Transition Region and Coronal Explorer (TRACE) satellite [2]. (b) Inductively coupled plasma reactor for microfabrication processing (Institute of Advanced Materials, Physicochemical Processes, Nanotechnology, and Microsystems, Department of Microelectronics, National Center for Scientific Research Demokritos) [3].

In order for the plasma to be formed, the atoms or molecules within a gas must be heated to or beyond the ionization energy. The result is a huge number of charged particles that interact by electric forces. This is in contrast to a neutral gas where particles interact only during a collision, i.e. when two gas atoms "feel" the short-range Van der Waals force,¹ which decays with the interparticle distance as r^{-6} . This means that two neutral atoms are not affecting one another until they collide. On the other hand, the electrostatic interaction decays as r^{-2} which makes it a long range force. Considering this situation, in the plasma state, charged particles produce a long-range field (like Coulomb field), which can affect many particles at a distance. In this sense, the plasma state is able to react to an external stimulation in a collective manner [2].

¹ From a physics point of view, the Van der Waals force is the spontaneous formation of dipoles due to distortion of electron clouds of adjacent atoms.

Several varieties of plasmas exist, characterized by their electron densities and temperatures. Figure 1.2 shows the ranges of electron temperature, electron density, and Debye length² [4] for typical plasmas found in nature and in technological applications [5].

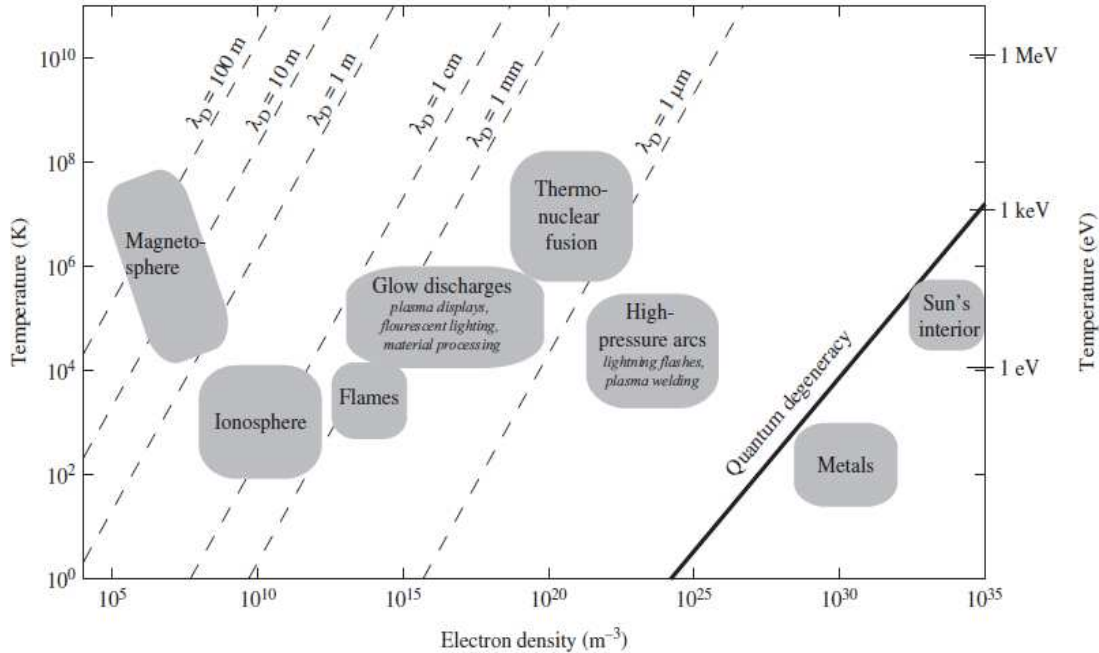


Figure 1.1: Range of temperature, electron density, and Debye length for typical plasmas in nature and in technological applications. It should be mentioned that only states to the left of the quantum degeneracy line are considered plasmas and can be treated with formulations from classical physics. Reproduced from [5]

1.2 Plasma etching in the industry

1.2.1 Introduction

Nearly half century has passed since Gordon Moore realized that the number of transistors in an integrated circuit (IC) had the tendency to double approximately every year. Based on this observation, he successfully predicted that IC transistor density would have an exponential growth in the future. This estimation has been known as Moore's Law, and the IC industry has followed this trend so far. Figure 1.3 presents the number of transistors in different microprocessors versus their introduction date.

² The Debye length λ_{De} tells us how rapidly a potential perturbation is attenuated in the plasma. Over a distance λ_{De} , the perturbation is reduced to $1/e$ of its initial value. In particular, the variation of the potential around a perturbation is given by

$$\Delta V(x) = \Delta V_0 \exp\left(-\frac{|x|}{\lambda_{De}}\right).$$

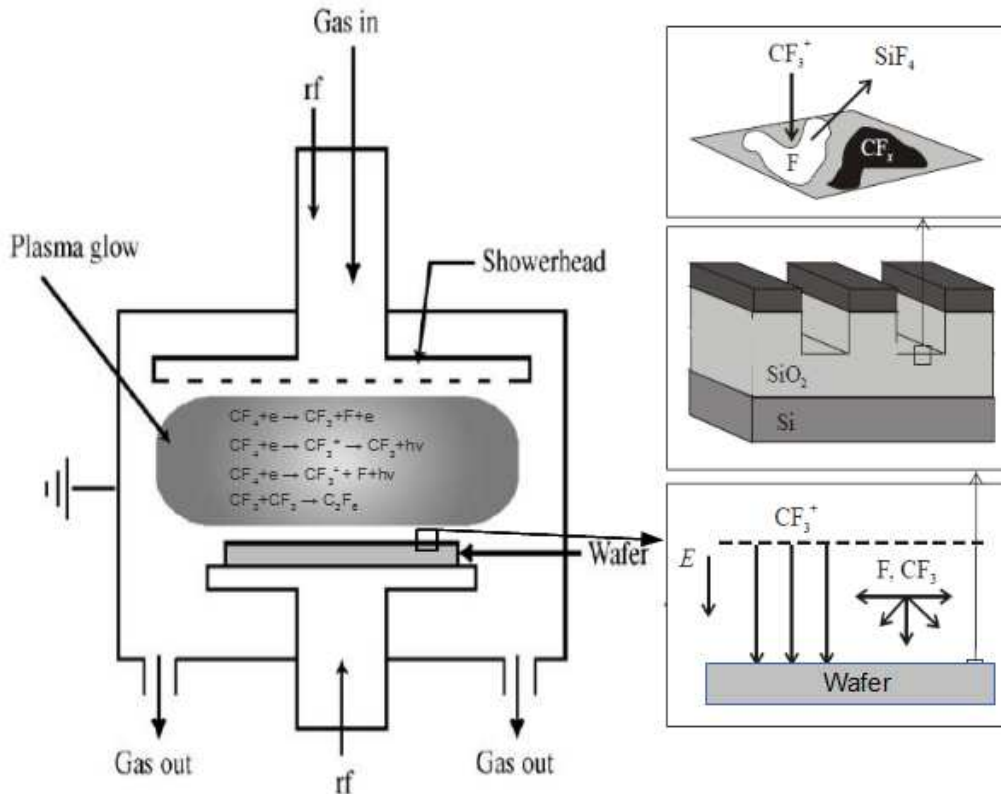


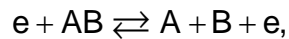
Figure 1.3: Sketch of a parallel plate triode plasma etcher [8]. The typical processes that take place both in the bulk of the plasma and the wafer are shown [3].

The wafer that is intended to be processed is deposited on one of the two electrodes. A proper pumping system holds the pressure at very low levels. When a voltage is applied in the chamber which contains the gas, a discharge will flash between the two electrodes. This discharge will create a large number of ions and free electrons. Two regions can be distinguished in the plasma. In the first one, which is called the bulk of the plasma, the densities of ions and electrons are equal. The second one, which is located just above the electrodes is called the plasma sheath. Due to electron depletion, this region precludes optical emission. A large electric field is developed in the sheath region. Ions that drift and diffuse to the edge of this region are accelerated rapidly toward the electrodes. If the electrode is covered with wafers, this ion bombardment can be used in order to drive various processes.

To maintain a steady state of electron and ion densities in the bulk of the plasma, the recombination process must be balanced by an ionization process, i.e. an external energy source is required. In practice this energy source is an electric field which can act directly on the charged particles only. Provided that the ion mass is much larger than the electron mass, it is obvious that the action of the field is primarily to give energy to the electrons (2-8eV)

[4].⁴ Although electrons collide with neutral atoms and ions, only a very small energy transfer to the heavy particle can take place [4].⁵ This is also the reason why the containing vessel of the plasma is not melting. Indeed, only a small amount of energy is transferred to the reactor walls or the wafer atoms. Ultimately, since the ions are able to receive some energy from the external field, their temperature is above the ambient temperature.

The types of processes that may arise in the plasma can be differentiated as dissociation



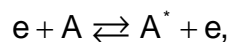
atomic ionization



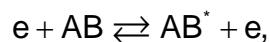
molecular ionization



atomic excitation



and molecular excitation



where e denotes an electron, AB denotes a molecule of a neutral gas and the superscript (*) denotes that a species is at an excited state. Dissociated atoms (or fragments of AB molecule) like A and B are called radicals. Radicals have an incomplete bonding state and are extremely reactive. Ions are charged atoms or molecules such as A^+ or AB^+ .

1.2.3 Mechanisms of plasma etching

The mechanisms of plasma etching can be categorized into physical (mechanical) sputtering, pure chemical (thermal), and ion-enhanced etching [9].

⁴ The work done by the electric field on an initially stationary particle with mass m , and hence the energy transferred to this particle can be easily proved that is equal to $\frac{(Eet)^2}{2m}$, where E is the magnitude of the electric field, e is the electronic charge, and t is the time.

⁵ The energy transfer from an electron to an ion is expressed by the equation $\frac{E_{ion}}{E_{electron}} = \frac{4m_{electron}m_{ion}}{(m_{electron} + m_{ion})^2} \cos^2 \theta$ where θ is the angle of incidence.

Physical sputtering results from the physical ejection of material due to bombarding with high energy ions. More precisely, when high energetic ions impact on a wafer surface, their kinetic energy is absorbed by the lattice atoms. In order for the crystal to dissipate this energy, a particle or more must be ejected from the solid. The number of particles that are removed per incident ion is expressed by the sputtering yield. The direction of etching is that of the bombarding ions. The selectivity⁶ of this mechanism is low.

Pure chemical or thermal etching occurs through a chemical surface reaction between neutral species with volatile products. Typically, there is no significant difference with wet etching in the sense that both advance through chemical interaction with the surface. Consequently, owing to their deficiency in directionality,⁷ pure chemical etching is mainly utilized in cases where isotropic etching is needed.

As far as the ion-enhanced is concerned, interestingly enough, both chemical and physical surface interactions are important in this process. Indeed, Coburn and Winters showed that the chemical and physical attributes of ion-enhanced etching are not simply additive but act in synergy, something that is clearly illustrated in figure 1.5 [10].

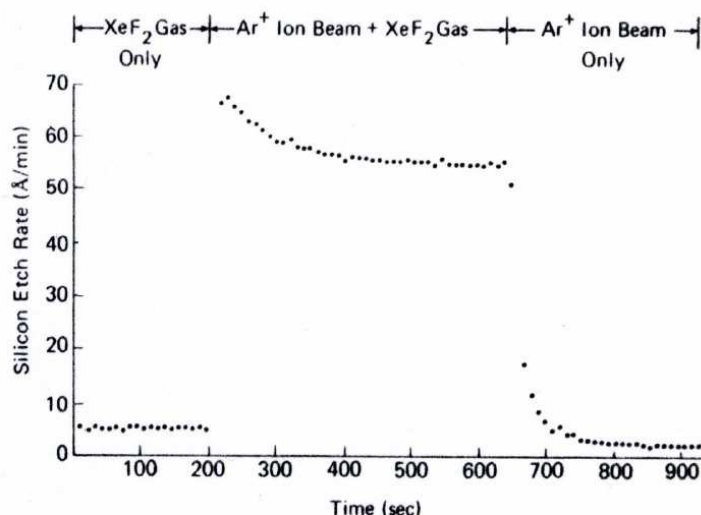


Figure 1.4: Coburn and Winters measured silicon etching rate under independent and concurrent exposure to XeF₂ gas and 450 eV Ar⁺ ion beams. They observed that the etching rate under simultaneous exposure to both the beams was nearly six times the sum of the etch rates under exposure to the individual beams. Taken from [10].

Ion-enhanced etching is an anisotropic etching process. The selectivity obtained in this occasion is significantly reduced in comparison to a thermal process.

⁶ Etching selectivity of material A to B is the ratio of etching rates of A to B.

⁷ Directionality describes the relative etch rates in the vertical and horizontal directions. An isotropic process etches at the same rate in both the vertical and horizontal directions.

1.3 Microstructure charging: origin and effects

Directional etching is the outcome of a robustly anisotropic ion angular distribution, developed while ions are accelerated through the sheath. On the other hand, electrons are decelerated in the sheath and their angular distribution is considerably more isotropic. This directionality difference between ion and electron fluxes is the origin of dielectric microstructure charging.

When the plasma etching of a dielectric trench takes place, the trench sidewalls restrict the flux of the isotropic electrons to the upper parts of sidewalls (see figure 1.6); due to electron shadowing only a small fraction of electrons reach the trench bottom. Simultaneously, due to their anisotropy, (positive) ions accumulate at the trench bottom. Positive charge will continue to build up until the bottom dielectric surface obtains a potential large enough to repel a sufficient number of ions. This is because the ion and electron currents to the bottom surface of the microstructure must balance at the steady state. Owing to the electrostatic repulsion, ultimately, a vast amount of ions impinge at the trench sidewall surface or even return to the plasma bulk. This phenomenon, known as microstructure charging, can lead to profile irregularities during etching, electrostatic etch stop or even oxide degradation and breakdown.

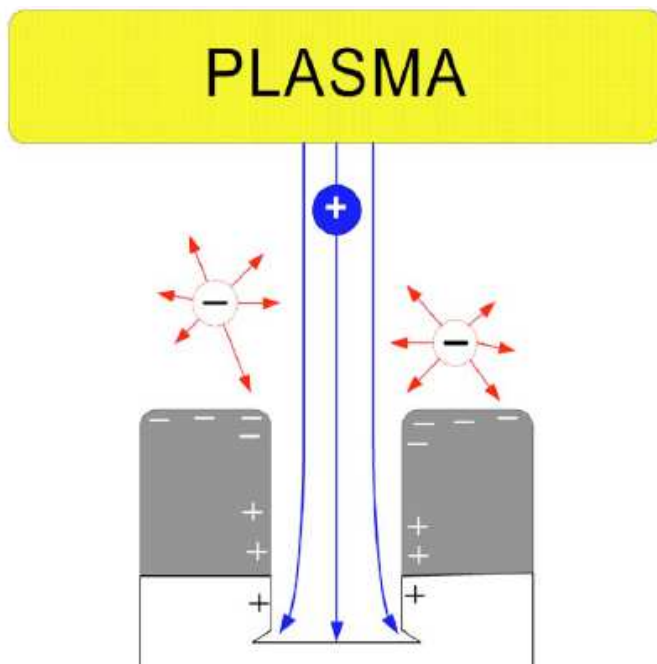


Figure 1.5: Microstructure charging process. High aspect ratio microstructures receive reduced electron flux at the lower trench sidewalls and bottom due to shadowing effects. For the case of insulating materials in either of these regions, surface charging phenomena can result [11].

Microstructure charging can lead to profile irregularities during etching, such as notching [12], microtrenching [13], or even etch-stop in dielectrics [14-17]. Apart from the distortion of profiles, charging can also lead to oxide

degradation and breakdown due to large Fowler-Nordheim (F-N) tunnelling currents which may flow in response to potential differences across the oxide [18].

The notching effect can be characterized as the formation of a long narrow wedge (the "notch") in a conductive material at the interface with an underlying insulator [12]. Commonly, it is developed at the inner sidewall foot of the outermost feature in a L&S pattern neighbouring an open area, as shown in image 1.2 [19, 20].

Microtrenching describes the appearance of narrow grooves at the edges of the feature bottom during ion bombardment. Pattern dependent charging can lead to such a damage as ions are deflected due to the mask negative charging and subsequently are scattered at the microstructure sidewalls [13]. Cases of microtrenching damage in view of charging are shown in image 1.3 [21].

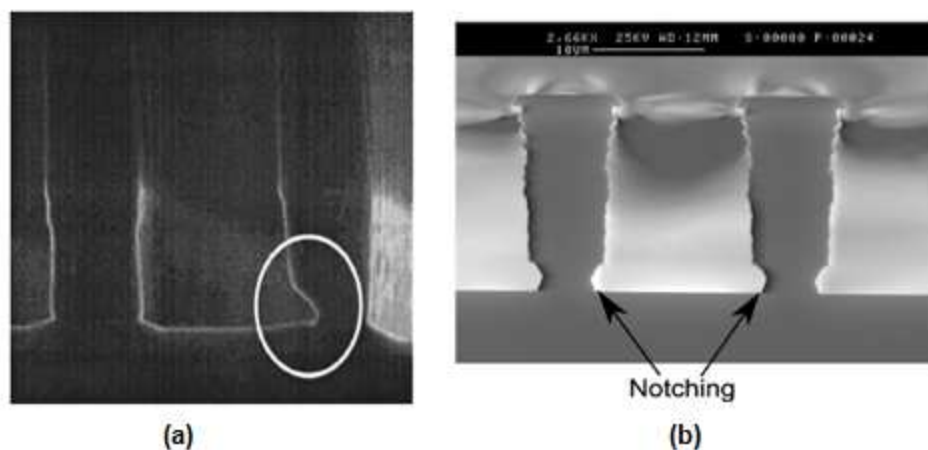


Image 1.2: (a) Example of the notch which is the opening of a narrow groove in a conductive material at the interface with an underlying insulator. Taken from reference [20]. (b) Experimental results from Oxford Instruments Plasma technology, reproduced from the paper of Ishchuk et al. [19].

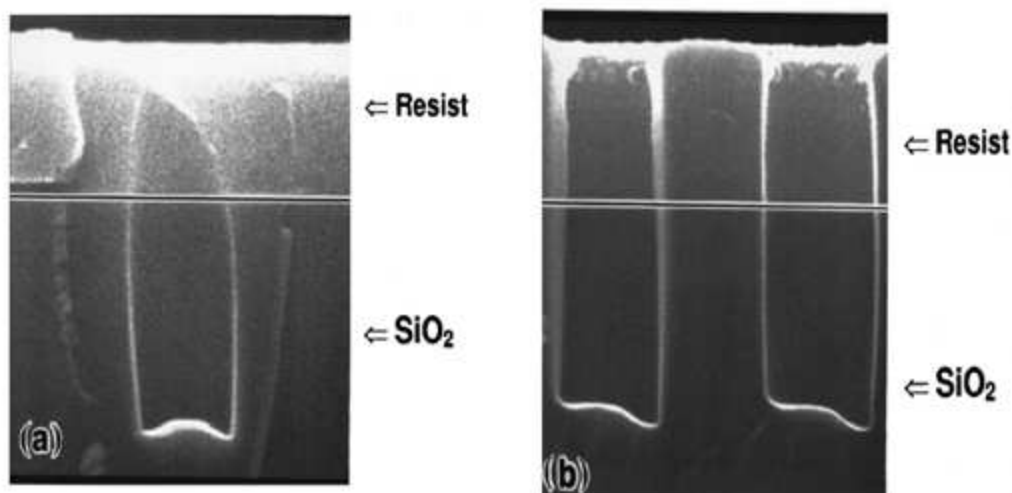


Image 1.3: (a) Microtrenching profile due to the differential charging mechanism in the absence of a magnetic field. The local electric fields in the feature deflect ions from the

centre towards the negatively charged sidewalls, resulting in symmetric microtrenching. (b) Schematic view of differential charging in the presence of a magnetic field. The Lorentz force F_L deflects electrons, resulting in an asymmetric electron angular distribution, resulting in asymmetric microtrenching. See reference [21] for more details.

Differential microstructure charging has also been reported as a significant factor for reactive ion etching (RIE) lag in dielectrics [22]; RIE lag describes the situation where the wider features are etched at a higher rate (image 1.4) compared to the narrower ones. The accumulation of positive charge at the trench or via bottom can deflect ions to the sidewalls or reduce their translational energy and consequently decrease the etching rate.

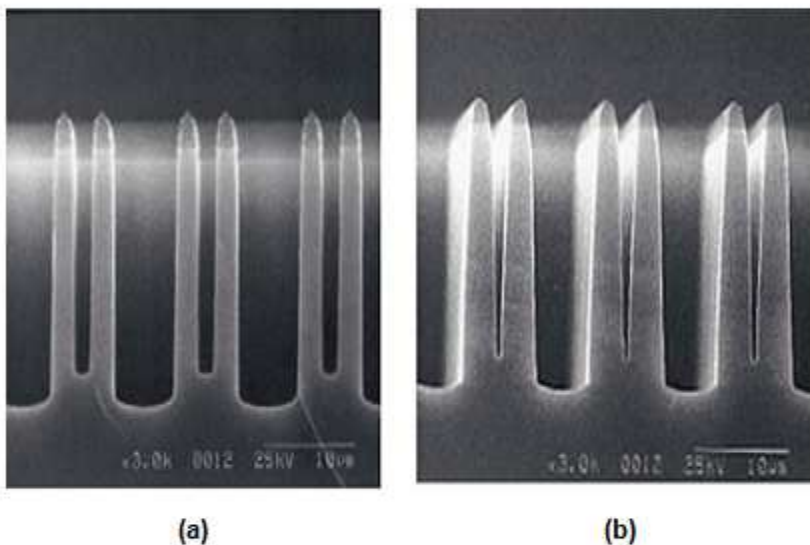


Image 1.4: As the (a) SiO_2 and (b) Si_3N_4 trenches become deeper, the differences in trench depths of the 2 μm and 7 μm wide trenches become more obvious due to RIE lag [23].

1.4 Previous works on microstructure charging

The role of the directionality difference between ions and electrons in microstructure charging was first recognized by Arnold and Sawin [14]. They were the first to simulate the charging of an individual dielectric trench assuming monodirectional ion bombardment (with an energy of 100eV) and an isotropic electron flux (with a temperature of 4eV) in two-dimensional (2D) geometry.

Kinoshita et al. [24] numerically simulated the influence of a rising bottom potential on the trajectory of approaching ions using the simulation domain depicted in figure 1.10. They concluded that the bottom potential raised up repelling enough ions so that the ion flux that was reaching the bottom was equal to the shadowed electron flux. The dependence of notch depth on open space width (see figure 1.6) was also explained by taking account the potential minimum in the polysilicon (poly-Si) region of the outermost line.

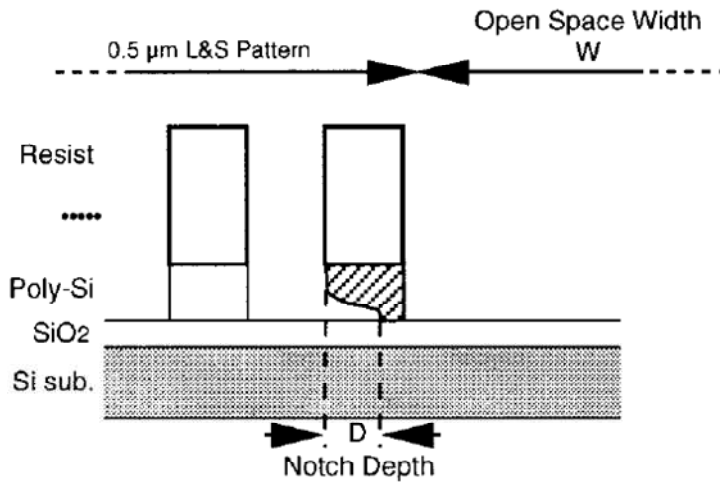


Figure 1.6: The simulation domain used by Kinoshita et al. [24].

Hwang and Giapis [12] improved the simulation of Kinoshita et al. by allowing the charge distribution in the poly-Si line to be affected by the positive potential on the oxide in the narrow space and by the negative charges on the resist. The result was that the bottom potential was increased and became very asymmetric. More precisely, Kinoshita et al. [24] assumed that the charge was equidistributed along the poly-Si sidewall surface in order for the poly-Si to be equipotential. However, Hwang and Giapis [12] understood that the aforementioned assumption was not in agreement with the electrostatic laws due to the presence of strong charging potentials at the aforementioned neighboring insulating surfaces. Indeed, they correctly postulated that the surface charge on the poly-Si lines should be unevenly distributed in order to make the surface equipotential. This conclusion led them to incorporate the redistribution of the charge in the poly-Si lines in their model. After this modification, they observed high accumulation of electrons in the outermost poly-Si/SiO₂ inner interface. The different approach of Hwang and Giapis [12] had a tremendous impact on the steady state potential distribution in the microstructure areas. In contrast to the work of Kinoshita et al. [24], the final potential distribution at the bottom of the trench was dramatically asymmetric. Eventually, Hwang and Giapis clarified why the notch appears at the foot of the inner sidewall of the outermost poly-Si line. In brief, the large and asymmetric positive potential at the trench bottom can slow down energetic ions so that they can be deflected and accelerated towards the lower part of the inner poly-Si sidewall.

Hwang and Giapis expanded their simulation to uncover the influence of different phenomena on pattern dependent etching and related profiles distortion effects [13, 18, 25-32]. An interesting work of theirs is the investigation for the effect of the aspect ratio of the microstructure on charging [29]. In that work, the photoresist thickness was varied to change the aspect ratio. Ultimately, it was verified that the notch was worsening with the increase of the aspect ratio.

Examining the electron temperature effects on microstructure charging [31], Hwang and Giapis verified that when the electron temperature increased, the deflected ion flux toward the inner side of the outermost line increased too,

while their energy remained constant. For that reason, they concluded that the greater the open space width and/or the electron temperature were, the worsen the notch would be.

A recent work on charging effect simulation belongs to Ishchuk et al. [19]. Specifically, their model was integrated in a full featured plasma processing simulation software. Due to this fact, both the charging effect and the etching process were evolving simultaneously. This appears contrary to the works of Kinoshita et al. [24] and Hwang et al. [12] where the profiles of already etched trenches were considered. Verification of their model was successfully accomplished as their results impeccably fitted with experimental ones.

All of the presented works until here refer to the charging of silicon-on-insulator (SOI) microstructures consisted of both conductive and insulating materials. However, works that investigate the consequences of charging effect exclusively in dielectric etching have also been published [15-17, 33].

In particular, Hwang and Giapis motivated by experimental results for SiO₂ etching [34], in which the aspect ratio dependent etching (ARDE)⁸ was questioned did not hold for the etching of oxides, calculated charging potentials for insulating surfaces [15]. Most importantly, they claimed that the violation of ARDE should be correlated to the failure of the dielectric surface to restrain charge dissipation. For that reason, surface currents were incorporated in their model. Specifically, they calculated the potential distribution along the trench surfaces by gradually reducing the width of the trench and concurrently holding the aspect ratio constant. The ensuing distributions were significantly different something that flawlessly indicated a violation of ARDE. Ultimately, Hwang and Giapis concluded that if surface currents did not exist, the formation of a high aspect ratio oxide hole would have been impossible.

A special class of polymers may have a finite surface conductivity under photo-irradiation or energetic ion bombardment from the plasma. Matsui et al. [16] took this fact under consideration and proposed a different mechanism of electron surface conductivity during oxide etching. Contrary to the work of Hwang and Giapis [15] in which there was no inhibitor deposition, in Matsui et al. model, a thin polymer layer prevented the trench wall from charging by a recombination process of the accumulated positive ion through a fast electron transport. The surface conduction in conjunction with the incident local fluxes of positive ions and electrons was described by a simple surface continuity equation. Conclusively, this research group numerically predicted that the sensitivity of the surface charging potential to the aspect ratio of the trench decreases when the wall has a finite conductivity during plasma irradiation.

Contrary to the previous works in which the steady state behavior of the surface charge densities and potential distributions were examined, Kenney and Hwang [35] investigated the dynamic behavior. In particular, the purpose of their research was to analyze if a steady state behavior would be reached in high aspect ratio dielectric nano-structures or the oscillation of the potential

⁸ Etching rate dependence on aspect ratio rather than the absolute feature size.

that were induced by individual charges would lead to stochastic behavior, i.e. stochastic surface charging. Ultimately, in the study of Kenney and Hwang, an oscillation in the potential in a high aspect ratio dielectric trench was observed. Namely, both the magnitude and frequency of the oscillation were increasing as the dimensions of the structure were decreasing.

Park et al. [17] studied the impact of pressure on the microstructure charging during the etching of SiO₂ trenches. They verified that the pressure increment involved a reduction in the charging effect. Specifically, due to the augmentation of collisions at a higher pressure, a wider angular ion distribution and a lower average ion energy ensued. Thus, owing to the small angle difference between ions and electrons, electron shadowing was impaired. Etching rate calculations confirmed the above tendency. Indeed, during etching of high aspect ratio structures, the low pressure led to undercutting and low etching rate. Contrarily, a moderate pressure mitigated the aforementioned charging effect consequences.

Other interesting works on the simulation of charging during plasma etching of microstructures are the those of Radjenovic et al. [36, 37] and Zhang et al. [38].

1.5 The aim and the structure of this work

The aim of this work is the development and implementation of a model for the simulation of surface charging on plasma "wetted" 2-dimensional (2d) microstructures. The cross section of a 2d structure does not vary along the third dimension; an infinitely long trench⁹ is a 2d structure. The algorithm is applied to the investigation of the charging in dielectric (infinitely long) trenches. In particular, the effect of several parameters such as the average ion energy and electron temperature on the local ion fluxes as well as the local etching yields and rates are examined. The aim is to estimate the importance of charging on the etching of insulating microstructures.

The charging simulation model consists of three sub-models. The first sub-model is the particle trajectories calculation model where the ion and electron trajectories are calculated by solving Newton equations. In the second sub-model, the surface charge density on the dielectric trench is calculated. The third sub-model is the charging potential model and includes the calculation of the space potential and electric field induced by the surface charging. The space potential and electric field is not only affected by the surface charge but it also affects it: the electric force coming from the field affects the trajectory calculation in the first sub-model. The potential in the simulation domain is updated after charge transfer from impinging particles on the dielectric surface.

Given that surface currents [15, 32] on the dielectric surface and tunnelling currents [18] through the oxide thick are both neglected for the present work, the study aims to reveal the worst case scenario of microstructure charging.

⁹ The third dimension of an infinitely long trench is practically much greater than the other two.

As far as the tools for the solution is concerned, a Matlab [39] code is developed for the first and second sub-models. The computations in the third sub-model are realized by Comsol Multiphysics 4.3b [40]. During the repetitive charging process, all models cooperate with each other through the Matlab programming environment (Comsol Livelink for Matlab [11]). Parallel computing techniques are utilized in order to reduce the simulation time in an efficient way. Computers from the recently instituted computer cluster [41] at the Department of Microelectronics of the NCSR 'Demokritos were utilized for the implementation of the simulation.

This work is the first step for the incorporation of a charging model into ϕ etch, i.e. an integrated simulation framework for feature profile evolution [42] and the application of the charging on to random surface morphologies in order to study the effect of charging on roughness formation and evolution on surfaces of insulating materials.

In the following, the structure of this work is given. Specifically, in the second chapter, the origin of microstructure charging is examined. Electron shadowing effect is introduced as the cause for pattern dependent charging and its impact is clarified. The third chapter includes the description of the charging model. The different sub-models and the coupling algorithm are presented. The fourth chapter includes two parts. In the first part, the accuracy of the charging model is examined by comparing its results with a published work. In the second part, a systematic study on the influence of charging on etching of features (trenches) is performed. The impact of charging under different conditions and cases is investigated. In particular, the effect of a) the shape of the ion energy distribution function, b) the average ion energy, c) the electron temperature, and d) aspect ratio of the feature on the local ion fluxes, etching yields and rates is examined. For the calculation of the etching yield and rate a model for ion enhanced etching is considered. In the last chapter, the obtained results are discussed. Future extensions and potential applications of the charging model are also proposed.

2 THE ORIGIN OF MICROSTRUCTURE CHARGING

2.1 Introduction

Any initially current imbalance will introduce charging on a dielectric surface segment. For instance, a larger ion flux will charge up the surface segment positively. Thus, electrons will be attracted in order to compensate the current imbalance. On the occasion that the counterbalance can not be accomplished in this way, this can happen when the initial current imbalance is overwhelming, the potential is continuously increasing until enough ions are deflected away to make current balance attainable. But how a current imbalance is provoked? Electron shadowing is the answer and it is discussed in this chapter.

The ion and electron dynamics in a radio frequency (RF) sheath is discussed and the development of a negative direct current (DC) bias at the wafer is both qualitatively and quantitatively investigated. The directionality difference between the ion and electron flux while they impinge on the processing wafer is attributed to this negative bias. Current imbalance on dielectric surfaces is associated with the aforementioned difference as emphasis is given on how such a disturbance can lead to charging build up. Electron shadowing effect is introduced as the common cause for current imbalance and its impact on pattern dependent charging is clarified.

2.2 Ion and electron dynamics in an RF sheath

2.2.1 Why RF plasma?

In many cases, the material on one or more of the electrodes in a plasma reactor is insulating. For instance, in the case of the DC plasma etching of silicon oxide (SiO_2), wafers with an upper layer of SiO_2 are first patterned lithographically and then placed on the electrode. The exposed materials on the top of the wafers, photoresist and oxide, are both insulators. As ions arrive on the surface of the wafer, these layers become charged. The positive charge accumulates on the surface and the DC field that sustains the plasma is gradually reduced until the plasma is ultimately extinguished.

To solve this problem, the plasma can be driven by an AC signal. In this case, in the first half cycle of the AC signal, the current will flow until the insulator is charged up and terminates the discharge. On the next half cycle, however, the insulator is discharged as current flows in the opposite direction. Thus, the insulator behaves like a capacitor that is charged in alternate directions by the plasma. If the AC frequency is increased to the point where the charging time is much longer than the AC half period, current will flow in the plasma for the entire AC cycle. A frequency of about 100 kHz [4] is usually sufficient to achieve this condition.

AC sources are in the RF range, commonly 13.56 MHz. This number has not a specific meaning. It just happens to be a frequency selected by the international communication authorities so as to avoid the disturbance of

potential surrounding communications [4] . At this frequency, the heavy ions cannot respond to the immediate electric field due to their inertia. On the other hand, the light electrons respond to the field. Due to the dissimilarities in mobilities of the aforementioned particles, a time-average negative bias will emerge. This bias is called RF self bias potential.

It is quite instructive to illustrate how this potential develops. A simple discharge system is depicted in figure 2.1. C is the capacitance of the insulating target. Clearly, the plasma shows a larger resistance for ion current than electron current owing to the greater mobility of electrons. But what is the impact of this fact? Well, imagine a square wave with peak amplitude V_1 imposed on the system. At the beginning of the process, the capacitor is initially uncharged ($V_c=0$) so from Kirchhoff's Voltage Law (KVL) the potential at the plasma will be V_1 . Due to the positive polarity, ions will be repulsed from the insulating target while electrons will be severely attracted. The capacitor is charged through the effective resistance of the plasma for electron current flow. The initial potential value V_2 of the discharge will fall as shown in figure 2.2. Indeed, due to the capacitance charging, it applies for the capacitor potential

$$V_c = V_1(1 - V_1 e^{-t/\tau}) \quad (2.1)$$

and for the plasma potential

$$V_2 = V_1 e^{-t/\tau} \quad (2.2)$$

where

$$\tau = R \cdot C \quad (2.3)$$

is the time constant of the system,¹⁰ R is the effective resistance of the plasma and, as it has been already mentioned, C is the capacitance of the insulator target.

Next, in the second half of the cycle, the plasma potential decreases by $-2V_1$. Due to the negative polarity, ions will be attracted to the insulating target while electrons will be severely repulsed. The capacitor is charged through the effective resistance of the plasma for ion current flow. The initial potential value V_2 of the discharge will fall as shown in figure 2.2. However, due to their inertia, ion current is significantly smaller than the above mentioned electron current, thus plasma potential decays slower (a larger time constant ensues for the system). Due to this behavior, not only an oscillation damping can be observed but also the whole insulator's potential waveform is displaced toward the negative values. However, after a few cycles, the time average ions and electrons currents will be equal and the waveform will oscillate in a

¹⁰ τ represents the time for the system to make a significant change in voltage whenever the capacitor is charging or discharging.

constant way. From this condition, a time-average negative bias on the electrode ensues. This is the RF self bias potential.

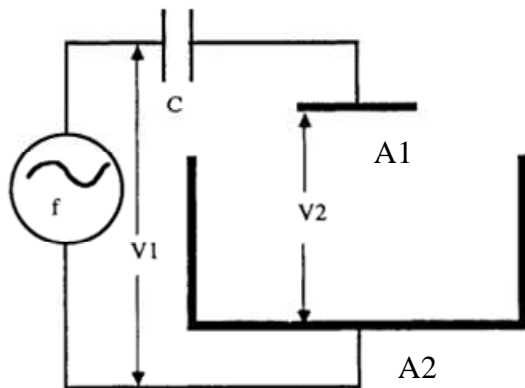


Figure 2.1: Schematic of electrode configuration for an RF glow discharge. An RF power supply is capacitively coupled to the electrodes. Taken from [43]

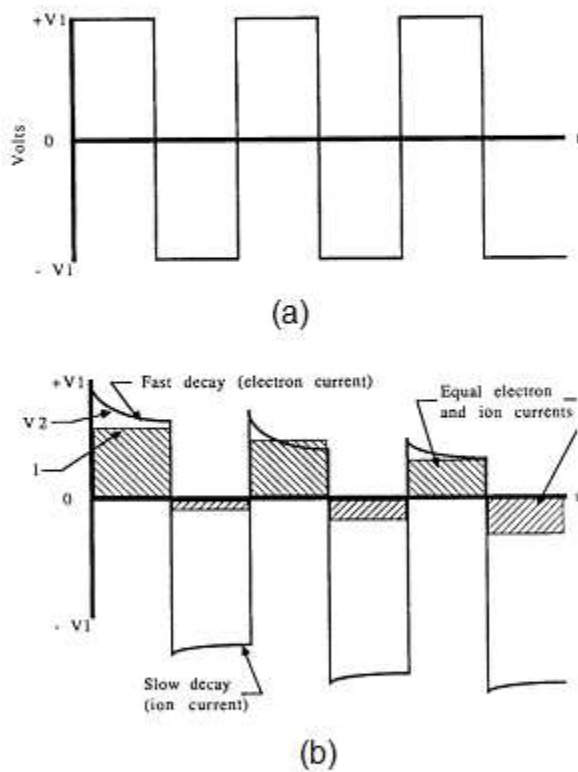


Figure 2.2: a) Electrode's voltage and current waveforms when the circuit of figure is squared wave excited. b) On each half cycle, the current decays as the capacitor charges from the plasma. Taken from [43].

A similar effect holds for a sinusoidal wave, where the electrode acquires a negative self-bias, which in this case has a value equal to nearly half of the applied rf peak to peak voltage (see section 2.2.2). This is illustrated in figure 2.3.

In this respect, an RF plasma can be similar to the DC plasma. More specifically, at low frequencies, the ion current flows towards the insulator

electrode until the insulator is charged up and so the break field¹¹ extinguishes. Indeed, from equations (2.1) and (2.2), while V_c increases, V_2 decreases; when V_2 becomes lower than the breakdown voltage the plasma is terminated.

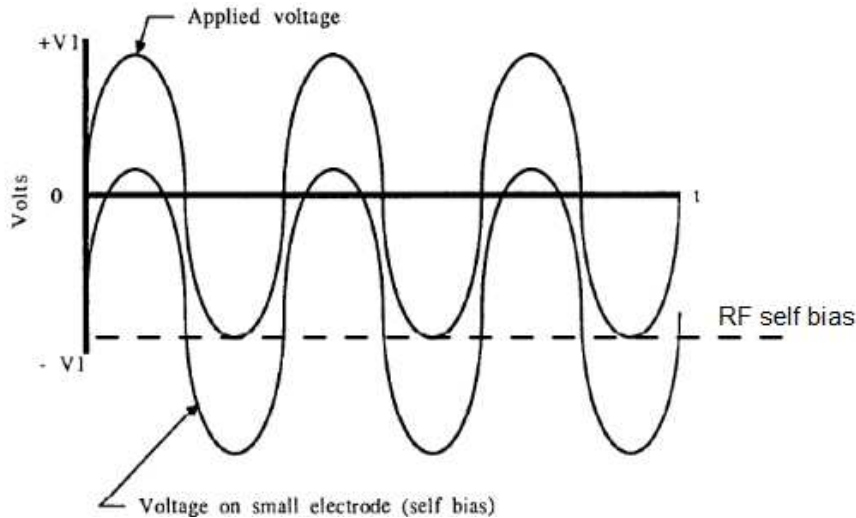


Figure 2.3: Self bias and DC offset of a sine wave driven system. The RF signal is superimposed on the RF self bias level. Taken from [43]

On the next half cycle, ion current flows at the opposite direction while electron current flows towards the insulator, thus the insulator is discharged. Conclusively, there will be a series of short-lived discharges as the signal successively takes opposite polarities. At the beginning of the AC period the discharge will start and will end at some time point inside the half period. During the second half of the period the insulator will be discharged.

To overcome this problem, the secret is to increase the AC frequency to the point where the charging time of the insulator is much longer than the AC half period. In this way, a sheath will form each time at the electrode which is negative during the particular half cycle of the AC power. The ions which are able to cross the sheath in a short time compared to the AC half period (before the polarity changes), will gain an amount of energy roughly equal to the instantaneous AC voltage. Thus, the ions striking the electrodes will have a distribution of energies (see section 3.2.2).

At high frequencies, the sheaths widths are pulsing with the applied signal so rapidly that the slow ions cannot follow the voltage change. However, electrons are severely accelerated and decelerated according to the polarity. During alternate half cycles, electrons strike the surface of each electrode, giving to both a net negative charge with respect to the plasma. In this case,

¹¹ The potential difference at which a gas is transformed from an insulator to a conductor. As the voltage is increased, the free electrons present in the gas gain energy from the electric field. When the applied voltage is increased to such a level that an appreciable number of these electrons are energetically capable of ionizing the gas, the gas makes the transition from an insulator to a conductor; that is, it breaks down. The potential difference at which this transition occurs is known as the breakdown potential.

one sheath exists in the vicinity of each electrode.¹² Due to electron depletion, large negative DC voltage drops exist between the plasma and the electrodes. The RF signal is superimposed on this DC level (RF self bias). It can be shown [44] that

$$\frac{V_{2,A1}}{V_{2,A2}} = \left(\frac{A_2}{A_1} \right)^4 \quad (2.4)$$

where A_1 , A_2 are the areas of the electrodes and $V_{2,A1}$, $V_{2,A2}$ are the voltage differences between the plasma and the electrodes. To maximize the voltage difference between the plasma and the electrode in which the wafer is placed, it is desirable to increase the area of the other electrode. This can be done by connecting it to walls of the chamber.

2.2.2 The mathematical expression of the RF self bias

Before any external AC oscillation is started, the electron and ion fluxes must be equal, i.e. the flux of ions is balanced by a Boltzmann-retarded thermal flux of electrons. Indeed, suppose we suspend a small electrically isolated substrate into the plasma. Initially, it will be struck by electrons and ions. The electron flux is larger from the ion flux (due to the larger kinetic energy of electrons) so immediately a negative charge starts to build and hence negative potential is developed with respect to the plasma. Since the substrate is charged negatively, electrons are repelled and ions are attracted. Thus the electron flux decreases, but the object is continuously being charged negatively until the electron flux is reduced by repulsion just enough to balance the ion flux. Thus, the total ion flux on both electrodes must be equal to that of the electrons at steady state.

The voltage difference between the electrode surface and the plasma boundary will be the floating potential [44], defined as¹³

$$V_f = \frac{kT_e}{e} \frac{1}{2} \ln \left(\frac{2\pi m}{M} \right), \quad (2.5)$$

where T_e is the electron temperature, k is the Boltzmann constant, e is the electronic charge, m is the electron mass and M is the ion mass.

However, in the previous section we saw that in the case of an AC signal, the large amount of electrons collected by the wafer during the frequency's positive cycle cannot be neutralized by the ion current that is unaffected in high frequencies by the AC voltage. This leads to the formation of an RF floating potential in correspondence with equation (2.5). More precisely, during the continuous RF modulation of the potential between the wafer and the plasma, the instantaneous electron flux arriving at the wafer will be

¹² Imagine fast decay for the insulator's potential due to electron current and simultaneously almost no decay due to ion current in figure 2.2.

modulated through the dependence of the Boltzmann factor on the instantaneous oscillating potential [45]

$$\Gamma_e = \frac{1}{4} n_e \bar{u}_e \exp\left(\frac{eV(t)}{kT_e}\right), \quad (2.6)$$

where n_e is the electron density, \bar{u}_e is the electron thermal velocity and

$$V(t) = V_1 \sin \omega t + V_{f_{RF}}, \quad (2.7)$$

where V_1 is the amplitude of the RF signal imposed on the wafer, ω is its frequency and $V_{f_{RF}}$ is the RF floating potential.

Obviously, the charge cannot be balanced at all times in the wafer. It can only be balanced when the entire AC cycle is integrated. Therefore

$$\left\langle \frac{1}{4} n_e \bar{u}_e \exp\left(\frac{e(V_1 \sin \omega t + V_{f_{RF}})}{kT_e}\right) \right\rangle = 0.6 n_e u_B, \quad (2.8)$$

where the angled brackets imply averaging over one period of the RF signal.¹⁴

Utilizing equation 2.8, it can be shown that [45]

$$V_{f_{RF}} = \frac{kT_e}{e} \left[\frac{1}{2} \ln\left(\frac{2\pi m}{M}\right) - \ln I_0\left(\frac{eV_1}{kT_e}\right) \right] \quad (2.9)$$

where m is the electron mass and M is the ion mass and I_0 the zero-order modified Bessel function [45]. From equation (2.9), it can be concluded that an RF voltage across a sheath shifts its DC floating potential (equation (2.5)) by

$$V_{f_{RF}} - V_f = -\frac{kT_e}{e} \ln \left[I_0\left(\frac{eV_1}{kT_e}\right) \right] \quad (2.10)$$

This value is the RF self bias. It's just the potential difference between the biased and unbiased (without RF) electrode. The relationship between the RF floating potential and the amplitude of the applied RF voltage is shown in figure 2.4 for Argon (Ar) plasma. For $V_1 < kT_e/e$ the floating potential is close to the DC value, but for $V_1 > kT_e/e$ the magnitude of the floating potential gets ever closer to the RF amplitude.

¹⁴ The origin of factor 0.6 is explained in section 2.3.

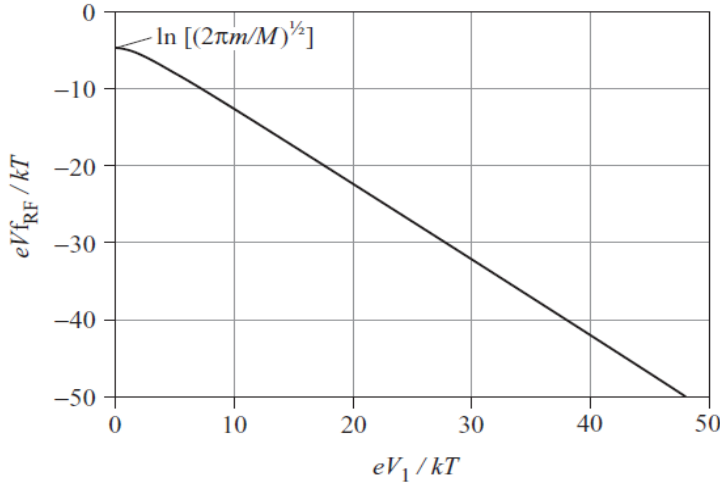


Figure 2.4: Floating potential for a sinusoidally modulated sheath in an Ar plasma; the floating potential approaches the RF amplitude V_1 at high bias while at very low bias the RF self bias becomes negligible and the floating potential approaches the DC value. Reproduced from [45].

2.3 The directionality difference between ions and electron fluxes at the wafer

Microstructure charging is induced by the directionality difference between ion and electron fluxes at the wafer. The origin of this difference is discussed below.

More precisely, electrons enter the sheath having a Maxwellian energy distribution.¹⁵ This means that they have the same velocity in any direction towards the wafer, thus their angular distribution is isotropic. Simultaneously, due to the time average negative self bias developed on the electrode (RF self bias potential, see sections 2.1.1 and 2.1.2), electrons are decelerated in the sheath and the vast majority of them are repelled back to the plasma. Actually, only a small fraction of electrons can cross the sheath. This fraction is comprised of electrons from the Maxwellian energy distribution that are energetic enough to overcome the potential $V_{f_{RF}}$ [equation (2.9)]. In other words, only electrons with sufficient perpendicular velocity can reach the wafer

$$u_{\perp}^e \geq \sqrt{\frac{2eV_{f_{RF}}}{m}}, \quad (2.11)$$

where e is the electron charge, $V_{f_{RF}}$ is the RF floating potential of the electrode and m is the electron mass.

¹⁵ Electrons emerge from plasma into the sheath region due to random thermal motion. The Maxwellian distribution conveniently relates a characteristic electron temperature to the average energy of electrons.

The direction of the aforementioned electrons can be enclosed within a narrow angle φ , denoted in figure 2.5 [18]. Due to repulsion, these electrons are decelerated as they traverse the sheath and as a consequence their angular distribution expands. However, near the boundary lower sheath and so the wafer, their average energy (temperature) is the same with that of the electrons of the plasma initially due to the fact that these electrons had initially energies greater than the average [4]. Ultimately, the electron angular distribution function can be described by $\cos^n\theta$, where $n \leq 1$ and θ is the angle of incidence of electrons at the wafer [12].

On the contrary, ions, are accelerated in the presheath region to the Bohm velocity¹⁶,

$$u_B = \sqrt{\frac{kT_e}{M}}, \quad (2.12)$$

where k is the Boltzmann constant, T_e is the electron temperature and M is the ion mass. Consequently, the vertical coordinate of ion velocity,

$$u_{\perp} = u_B, \quad (2.13)$$

i.e. that in the direction perpendicular to the wafer, is larger than the thermal velocity of ions in the lateral direction, that is, parallel to the wafer

$$u_{\parallel} = \sqrt{\frac{kT_i}{M}}, \quad (2.14)$$

where T_i is the ion temperature. As the ions cross the sheath, they are accelerated further due to attraction from the negative RF self bias and so their angular distribution evolves into highly anisotropic (see figure 2.5).

¹⁶ Between plasma and sheath exists a quasi neutral transition region of low electric field, and the effect of this region is to increase the velocity of ions entering the sheath. This electric field penetrates plasma by a short distance, the size of an electronic Debye length (screening length). A voltage drop of $kT_e/(2qe)$ occurs across this distance. Here k is the Boltzmann constant, T_e is the electron temperature and e is the electronic charge. Within this screening length, ions are accelerated by the $kT_e/2e$ potential toward the sheath. This results in an ion flux significantly larger than just the due to random thermal motion alone. This is the Bohm criterion for a stable sheath formation, which gives the saturated ion current that is independent of the sheath potential. The saturated ion current according to the Bohm criterion is $I_{ion} = 0.6nu_B$, where n is the plasma density. [4] B. Chapman, "Glow Discharge Processes," *John Wiley & Sons*, pp. 49-74, 139-172, 1980.

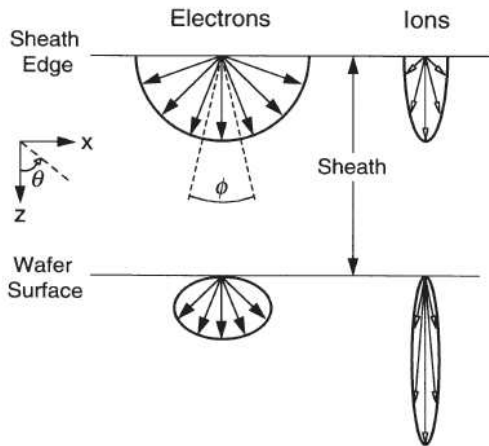


Figure 2.5: Depiction of the electron and ion angular distribution functions at the sheath edge and at the unpatterned wafer surface. The anisotropy of both distributions is evident. Nonetheless, ions are much more directional than electrons. The part of the electron angular distribution that will arrive at the wafer surface is denoted by ϕ . [18]

Examples of angular distributions for ions and electrons at an unpatterned wafer are presented in figure 2.6. In the ion angular energy distribution, the domination of the normal direction is conspicuous. Contrarily, this is not happening for the case of electrons. The flux of both ions and electrons hitting normal to an unshadowed surface segment ΔS (see figure 2.7) is maximum, although there are significantly fewer electrons than ions impinging at angles near to the value $\theta = 0^\circ$, where θ is the angle particle trajectory with the surface normal. Indeed, most electrons impinge at angles larger than a few degrees from normal. The origin of microstructure charging is the difference in the angular distributions of ions and electrons as demonstrated in the next paragraphs.

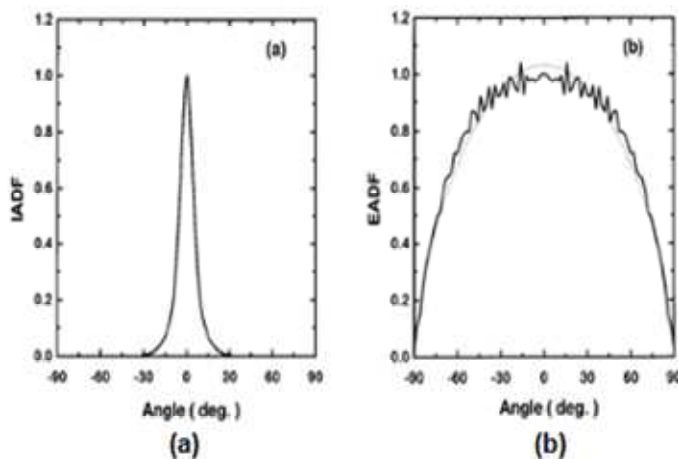


Figure 2.6: (a) Ion (Cl^+) and (b) electron distribution angular distribution at the sheath lower boundary as calculated by Hwang and Giapis [12].

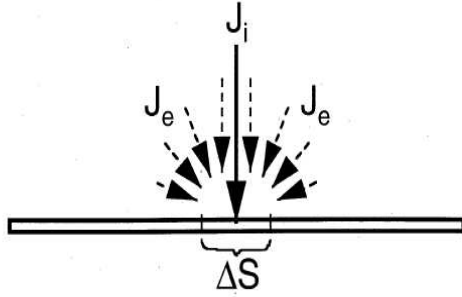


Figure 2.7: Depiction of the difference in the degree of anisotropy between ions and electrons. Almost all of the ions arrive at the segment ΔS at angles of incidence smaller than a few degrees from normal, while the majority of the electrons impinge at angles that deviate significantly from $\theta = 0^\circ$. The dashed-line arrows describe electron flux while the solid-line arrows depict ion flux. Decreasing length of the dashed lines indicates smaller electron flux. Taken from [18].

2.4 Electron shadowing effect

Assume a dielectric line placed on a wafer surface adjacent to the surface segment ΔS . Due to their low anisotropy, electrons arrive at oblique angles of incidence on ΔS . As a result, electron flux will be diminished in this region. On the other hand, ions are highly directed, thus their traces are slightly influenced. Hence, ΔS charges up positively. As far as the material of the surface wafer is concerned, it can be conductive or insulating. In the case of a conductive material, the aforementioned current imbalance will be restored by electron transport from other unshaded areas. Additionally, the top regions of the line sidewalls will charge up negatively due to the slanting electrons trajectories. Simultaneously, this negative charge will cause ions deflection towards the lower part of the sidewall charging it up lightly positively. In the case of an insulating material, accumulation of positive charge on the segment ΔS is incurred, as presented in figure 2.8. Ions are repelled due to the emerging positive electric field while more and more electrons are attracted. When steady state is reached, the electron flux is equal to the ion flux.

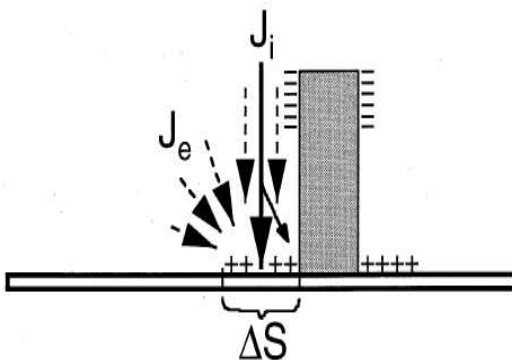


Figure 2.8: Schematic illustration of steady-state current balances at an insulating surface segment next to a single insulating feature of rectangular cross section. The dashed-line arrows describe electron flux while the solid-line arrows depict ion flux. Decreasing length of the dashed lines indicates smaller electron flux. The ion and electron fluxes are not to scale. Taken from [18].

Placing a second dielectric line, a trench is formed. In this case, electron shadowing is enhanced. Actually, the closer the lines are, i.e. the larger the aspect ratio is, the more severe the shadowing is. As in the previous case, the ion flux is not affected. Consequently, the current imbalance becomes more intense. If the wafer surface is conductive, current balance is restored by electrons transport from other unshaded regions. However, in the case of an insulating surface its potential must increase much more than that of the single-line case; more ions should be deflected to achieve equal fluxes of ions and electrons.

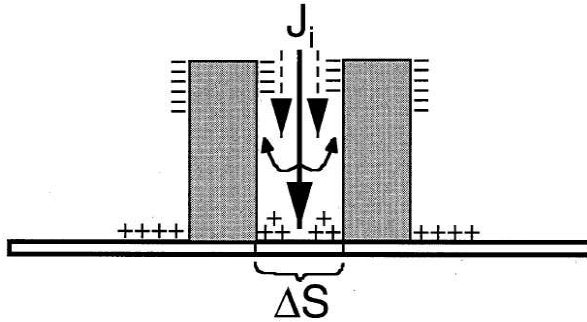


Figure 2.9: Schematic illustration of steady-state current balances at an insulating surface segment confined by two insulating features, forming a trench. The dashed-line arrows describe electron flux while the solid-line arrows depict ion flux. Decreasing length of the dashed lines indicates smaller electron flux. Taken from [18].

3 THE DESCRIPTION OF THE MODEL

3.1 Introduction

The aim of the microstructure charging model is the calculation of the charging potential as well as the local ion and electron fluxes inside dielectric microstructures, namely trenches, wetted by a plasma environment. The charging model consists of three sub-models, i.e. a) the particle trajectory, b) the surface charge density, and c) the space potential calculation models. A schematic of the linking among sub-models is shown in figure 3.1. A sequential use of the three sub-models for several times until the steady state condition is fulfilled is performed. A full sequential use of the models consists a charging step. A number of equal number of ions and electrons are released at each charging step. After that, their trajectories are traced, then the surface charge density, and finally the space potential and electric field are calculated. The space electric field is taken into account in the next charging step for the calculation of particle trajectories. The steady state condition is fulfilled when the potential distribution along the dielectric microstructure surface no longer changes.

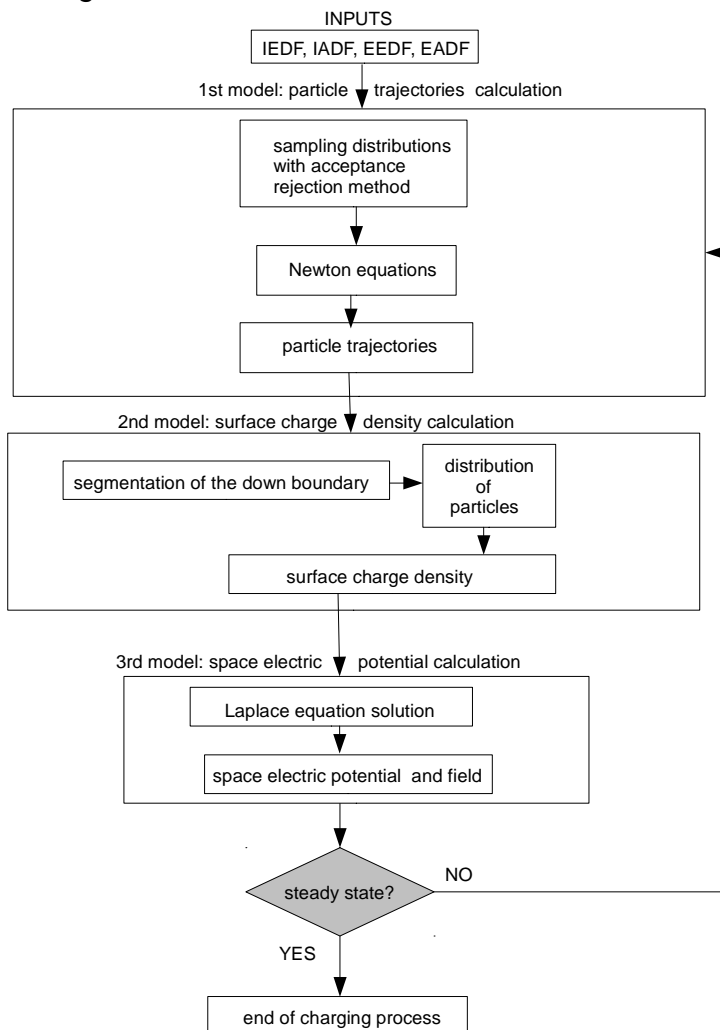


Figure 3.1: Schematic of the simulator algorithm.

In the first model, the trajectories of the particles, i.e. ions and electrons, inside the microstructure are calculated. Particles are released from the upper boundary or "inlet" of the simulation domain. The simulation domain is a rectangular area, such as the one shown in figure 3.2. A particle trajectory evolution depends on both its initial velocity and the electrostatic influence of the space electric field. The trajectories are calculated by the numerical integration of Newton equations of motion for each particle; a suitable Runge Kutta method [46] is used. Realistic energy and angular distributions at the wafer are utilized for the calculation of particles initial velocities. For this purpose, the aforementioned probability distributions are sampled with the acceptance-rejection method [47].

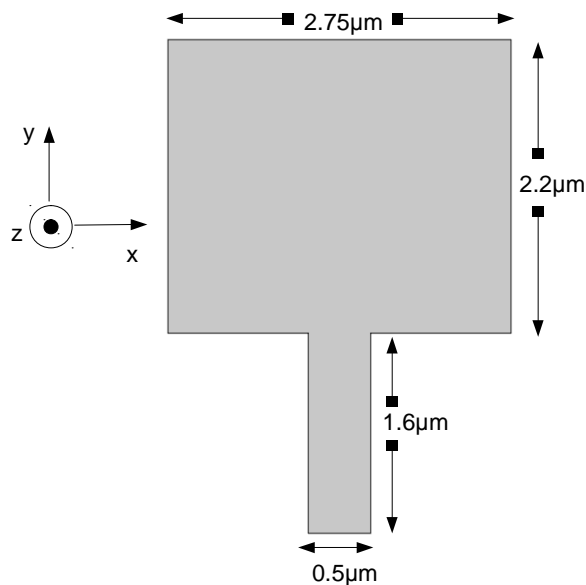


Figure 3.2: The simulation domain.

The space electric field that affects the particle trajectories, is coming from the surface charge that gradually accumulates on the microstructure or trench boundary and is calculated by the third sub-model. The trench is the bottom boundary of the simulation domain. When a particle reaches the left or right boundary of the simulation area, the particle trajectories continuity condition is activated [17, 19]. More precisely, the trajectories of the particles, which abandon the simulation domain and traverse the left and right boundaries, are mirrored with respect to the y axis. This means that the tracing of the simulated particle continues, but the sign of the x axis velocity component is reversed.

A particle trajectory is terminated on the trench boundary. The termination condition is implemented by utilizing the signed distance function [48] of the trench boundary; the signed distance is calculated by solving the Eikonal equation with the fast marching method [49]. A trajectory termination can also occur on the upper boundary (inlet); the electrostatic repulsion may cause the reverse of the sign of the particle velocity on the y axis. To accelerate the simulation, the superparticle concept is borrowed from the particle in cell (PIC) method [50]. Specifically, every particle represents a cluster of particles.

In the second model, the local surface charge density on the trench boundary is calculated. When an ion or an electron impinges on the dielectric surface, its charge is transferred on it. A discretization of the trench boundary to equal segments and the distribution of the particles (ions and electrons) on these segments are required for the calculations of the local surface charge density. After every charging step the local charge density is the total number of particles that have currently impinged of each segment divided with the length of the segment.

The third model includes the potential and electric field computation by solving the Laplace equation in the simulation domain [15]. The finite element method is employed with the proper boundary conditions. The surface charge density on the trench boundary is one of the aforementioned conditions.

Steady state is reached when the potential on the trench boundary no longer changes [15]. In this occasion, the potential has reached the saturation regime. This means that the ion and electron flux is equal at every point of the dielectric microstructure.

Regarding the dimension of the model, In this point it should be mentioned that the trench is assumed to have the same shape along the z axis, thus the charging should not vary along that direction [14, 19, 33]. This means that the electric potential and field parallel to that axis must be negligible compared to the field in the transverse coordinates.¹⁷ Consequently, a two dimensional (2d) approach can be utilized for the calculation of the electric field and this can be implemented by restricting our attention to the cross section of the trench. Additionally, due to the absence of an electric field component at that direction, the z velocity component of the particles is also neglected as the particles thermal energy is much smaller than their directional kinetic energy in the 2d region [51]. Finally, linear instead of surface charge densities on the microstructure are calculated by the second sub-model.

The 2d approximation is much faster than the full 3d approach. Indeed, introducing a new dimension to a 2d calculation requires more computational power for the solution of the Laplace equation and much more particles to achieve steady state.

As far as the tools for the solution is concerned, a Matlab [39] code is developed for the first and second sub-models. The computations in the third sub-model are realized by Comsol Multiphysics 4.3b [40]. During the repetitive charging process, all models cooperate with each other through the Matlab programming environment (Comsol Livelink for Matlab [52]).

The following paragraphs include a detailed description of the three sub-models.

¹⁷ The gradient of the electric potential is negligible to that direction.

3.2 Particle trajectories calculation model

3.2.1 The acceptance-rejection method

3.2.1.1 Introduction

The aim of this section is to present the way that the initial particle velocities are generated during the simulation process. More precisely, to implement such a generation, a proper technique must be incorporated in the model in order to sample random variables from known probability distributions. This technique or sampling procedure is an algorithm that can produce a sequence of values which can be considered to have been taken from a probability distribution. In our case, the values of the ion energy are sampled from a bimodal distribution while the values of the angle of their incidence are produced from a normal distribution. In the same manner, the values of electron energy are sampled from a maxwelian distribution, while the values of the angle of their incidence are generated from an angular distribution that is described by the equation [12]

$$f(\theta) = \cos^{0.6} \theta. \quad (3.1)$$

When the probability distribution to be sampled from is continuous but not standard then the acceptance-rejection method [47] can be utilized to perform sampling. The concept behind this type of sampling is to initially simulate values from a standard probability distribution, i.e. a distribution for which it is known how to generate values. Then by accepting some values and rejecting others, a sample from the desired distribution is acquired.

3.2.1.2 The algorithm of the acceptance-rejection method

Suppose we want to simulate a continuous random variable¹⁸ X with probability density function (pdf) $f(x)$ ¹⁹, which is nonzero on $[a,b]$ with $a, b \in \mathbb{R}$ and zero everywhere else, but that it is difficult to generate directly. Also suppose that we can easily generate a random variable having pdf

$$g(x) = \frac{G(x)}{\int_a^b G(x)dx} \quad (3.2)$$

¹⁸ In probability and statistics, a random variable or stochastic variable is a variable whose value is subject to variations due to chance (i.e. randomness, in a mathematical sense). As opposed to other mathematical variables, a random variable conceptually does not have a single, fixed value (even if unknown); rather, it can take on a set of possible different values, each with an associated probability.

¹⁹ A random variable is called continuous if there exists a function $\mathbb{R} \rightarrow [0, \infty)$ such that $P\{X \in B\} = \int_B f(x)dx$ for every set $B \subseteq \mathbb{R}$. We call f the probability density function of X .

and let $G: \mathbb{R} \rightarrow \mathbb{R}$ be such that $f(x) \leq G(x)$, $x \in [a,b]$. The procedure can be described by the following 3 steps.

i) Generate a random variable Y from $g(x)$. In the example that is depicted in the picture below, these Y random numbers are generated from a uniform distribution²⁰ in the interval $[a,b]$. It should be noted that random numbers that are uniformly distributed over an interval a to b may be generated in matlab by

$$Y = a + (b - a) \cdot \text{rand}, \quad (3.3)$$

where `rand` is a matlab function for producing uniform random variables distributed on the interval $(0,1)$.

ii) Generate U , uniform on $[0,1]$, independent of Y .

iii) If

$$U \leq \frac{f(Y)}{G(Y)}, \quad (3.4)$$

then set

$$X=Y \text{ (accept)}. \quad (3.5)$$

Otherwise, return to Step (i) (reject).

²⁰ The probability density function of the continuous uniform distribution is

$$f(x) = \begin{cases} \frac{1}{b-a} & \text{for } a \leq x \leq b \\ 0 & \text{for } x < a \text{ or } x > b \end{cases}$$

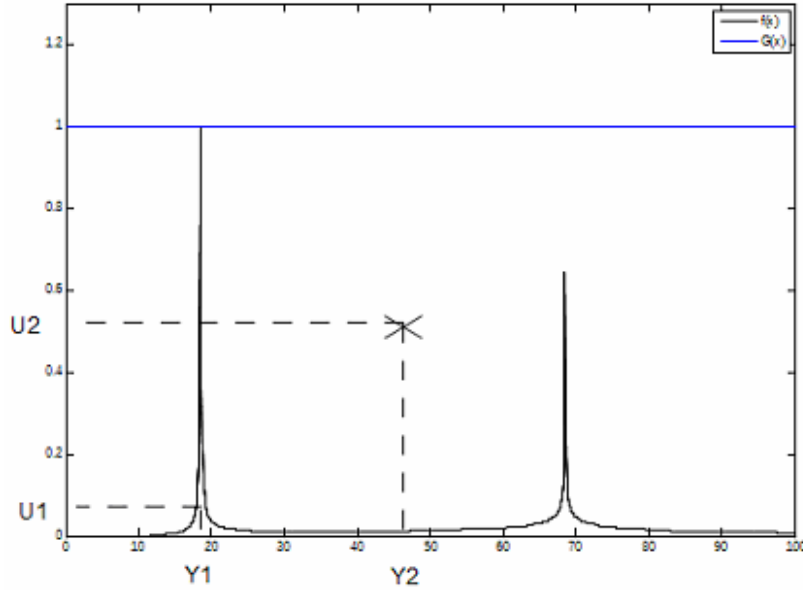


Figure 3.3: application of acceptance-rejection method on an arbitrary pdf. The rejection of a sample is denoted with the symbol x. The Y random numbers are generated from a uniform distribution on the interval [0,100].

A detailed mathematical proof of the acceptance-rejection method can be found in appendix I.

3.2.2 Ion energy and angular distribution function

3.2.2.1 introduction. Why a bimodal ion energy distribution function (IEDF)?

The significance of plasma frequencies in time varying sheaths is clearly illustrated from the fact that the crucial parameter that determines the shape of IEDFs in the surface of a wafer is the ratio[53]

$$\frac{\tau_{ion}}{\tau_{RF}} = \frac{\omega_{RF}}{\omega_{pi}}, \quad (3.6)$$

where

τ_{RF} is the radio frequency (RF) period of the bias imposed on the electrode and

$$\tau_{ion} = \frac{\lambda_{De}}{u_B} = \frac{\lambda_{De}}{\sqrt{kTe/M_{ion}}} = \omega_{pi}^{-1} \quad (3.7)$$

is the time it takes an ion to cross the first Debye length of the sheath λ_{De} ²¹ [4], having entered at the Bohm speed. Due to applied electric field, ions

²¹ The Debye length λ_{De} tells us how rapidly a potential perturbation is attenuated in the plasma. Over a distance λ_{De} , the perturbation is reduced to 1/e of its initial value. Specifically,

undergo simple harmonic motion of angular frequency ω_{pi} given by the equation [45]

$$\omega_{pi} = \sqrt{\frac{ne^2}{M_{ion}\epsilon_0}} \quad (3.8)$$

where n is the plasma density, e the electrical charge, M_{ion} the mass of the ion and ϵ_0 is the electric permittivity of free space.

In the low frequency regime ($T_{ion}/T_{RF} \ll 1$) ions are able to respond faster than an applied alternating voltage at the electrode surface. In other words, the time for ions to cross the sheath is much shorter than the oscillation period. Very low-frequency oscillations in the sheath potential can therefore be treated as a series of quasi-static states – that is, a direct current (DC) sheath model might be applied at any instant. But what does this really mean?

Well, as ions respond to the instantaneous sheath voltage, their energy depends strongly on the phase of the cycle in which they enter the sheath. Simultaneously, the large period of the sinusoidal modulation of the potential across the sheath entails that the voltage across the sheath changes most slowly through the phases of maximum and minimum.²² Thus, there will be markedly more ions having energies corresponding to the maximum and minimum potentials compared with the intermediate range. Consequently, the IEDF is broad and bimodal as it can be seen in figure 3.4. In the low frequency regime it can be expressed by the following equation [44]:

$$f(E) = \frac{1}{\pi} \frac{2\epsilon e^E}{(2\epsilon e^E - 1) \cdot \left\{ \bar{\eta}_s^2 - [\ln(2\epsilon e^E - 1)]^2 \right\}^{\frac{1}{2}}}, \quad (3.9)$$

where

$$E = \frac{E_i}{kT_e} \quad (3.10)$$

is the ion energy normalized to kT_e (k is the Boltzmann constant and T_e is the electron temperature), $\bar{\eta}_s$ is the peak RF drive voltage normalized to kT_e , and ϵ is essentially the square root of the mass ratio

the variation of the potential around a perturbation is given by $\Delta V(x) = \Delta V_0 \exp(-\frac{|x|}{\lambda_{De}})$, where

$\lambda_{De} = \sqrt{\frac{\epsilon_0 k T_e}{ne^2}}$. n is the plasma density, ϵ_0 is the permittivity of free space, k is the Boltzmann constant and T_e is the electron temperature.

²² This can be comprehended if someone imagine a sinusoidal curve and focus on its gradient which is zero at maxima and minima.

$$\varepsilon = \left(\frac{\pi m_e}{2M_{\text{ion}}} \right)^{\frac{1}{2}}, \quad (3.11)$$

where m_e is the mass electron and M_{ion} is the ion mass.

On the other hand, if the period of the modulation is nearly equal to the ion transit time, i.e. $T_{\text{ion}}/T_{\text{RF}} \sim 1$, some of the ions will fall into the sheath when it has a relatively small but fast growing potential across it. Other ions, having entered the sheath when the potential difference was rising more slowly close to its highest, may then be overtaken by the plasma boundary during the phase when the sheath width decreases. These latter ions then re-enter the sheath when the potential difference is lower (see figure 3.5b).

Finally, if the period of the modulation is much smaller than the ion transit time, i.e. $T_{\text{ion}}/T_{\text{RF}} \gg 1$, the ion trajectories become increasingly less responsive

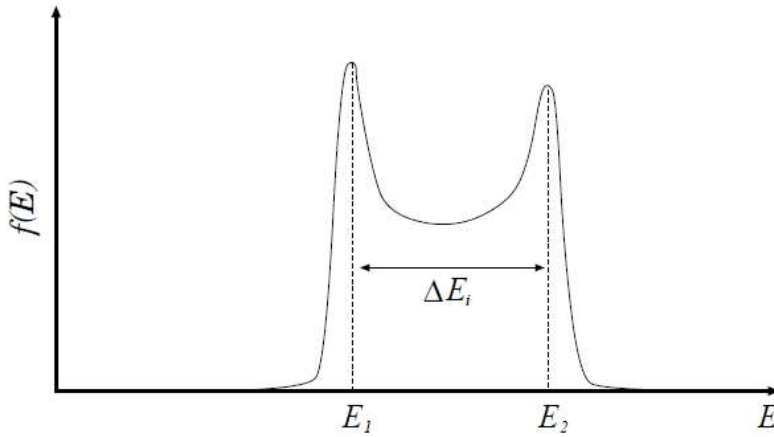


Figure 3.4: A bimodal IEDF. The two peaks in the distribution correspond to the minimum and maximum sheath drops i.e. where the voltage is most slowly varying. Taken from [53].

to the sheath motion. Once an ion comes within the range of the moving sheath its speed begins to increase, driven effectively by the time-averaged electric field (see section 2.2) in the region swept by the plasma/sheath boundary.

It should be mentioned that increasing the modulation frequency narrows the IEDF, effectively drawing the high and low-energy peaks closer together. At sufficiently high frequency ($\omega_{\text{RF}} \gg \omega_{\text{pi}}$), the peaks effectively merge to give a mono-modal IEDF [53].

Figure 3.5 illustrates the impact of the sinusoidal modulation period of potential across the sheath on the ion trajectories. The rapid steepening of the curves indicates acceleration.

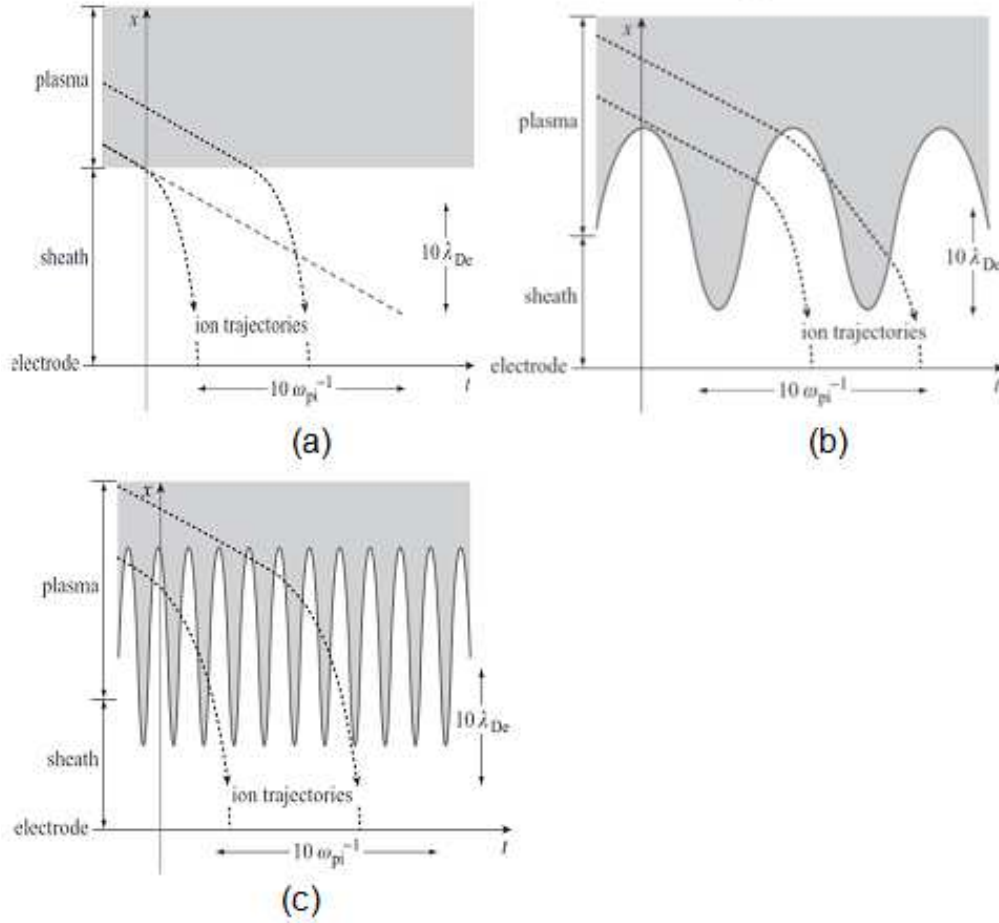


Figure 3.5: (a) The trajectories of two ions in a DC sheath, the second one is shifted in time crossing into the sheath at some later time. The rapid steepening of the curves indicates acceleration. (b) and (c) Schematic ion trajectories in temporally modulated sheaths, $\omega \sim \omega_{pi}$ and $\omega \gg \omega_{pi}$ respectively. In both cases, the ions are being repeatedly overtaken by the oscillating sheath. In the latter case the ion motion in this regime is effectively governed by the average fields (see section 2.2) so that the trajectories closely resemble those of a steady sheath. Reproduced from [45].

3.2.2.2 Ion velocities at the inlet of the domain

As it was previously mentioned the ions plasma frequency is given by the equation (3.8). Assuming that the majority of the ions in the plasma are Cl^+ and employing a plasma with a density of $1 \times 10^{11} cm^{-3}$, equation 3.8 ensues:

$$\omega_{pi} = 70 \text{ MHz} . \quad (3.12)$$

If the sheath RF bias frequency is assumed to be equal to $\omega = 1 \text{ Mhz}$, considering equation (3.6), it can be derived that

$$\frac{T_{ion}}{T_{rf}} = \frac{\omega_{rf}}{\omega_{ion}} = \frac{1 \text{ MHz}}{70 \text{ MHz}} = 0.014 \ll 1 \quad (3.13)$$

and as a result the equation of low frequency regime applies (see section 3.2.2.1). Thus, the IEDF at the wafer surface is given by the equation (3.9).

The electron and ion temperatures are taken to be 4 eV and 0.5 eV, respectively. The wafer electrode is biased at $\omega_{RF} = 1$ MHz with an RF voltage of 50 V. After the required substitutions, it follows from equation (3.9)

$$f(E_i) = \frac{1}{\pi} \frac{0.00986 \cdot e^{\frac{E_i}{4eV}}}{\left(0.00986 \cdot e^{\frac{E_i}{4eV}} - 1\right) \times \left\{156.25 - [\ln(0.00986 \cdot e^{\frac{E_i}{4eV}} - 1)]^2\right\}^{\frac{1}{2}}}. \quad (3.14)$$

The equation (3.14) is first multiplied with the proper factor in order to be normalized. The sampling of random variables of energy from the above mentioned distribution is implemented by the rejection-acceptance method [47]. The results of this method is presented in figure 3.6, where the probability density histogram of 1000 generated random energies is produced. Simultaneously, the curve which corresponds to the theoretical probability density function of ion energy is superimposed upon the histogram.

As far as the angular distribution of ions is concerned, the ions enter the upper boundary with an anisotropic flux distribution and they are accelerated as they traverse the sheath. Their angular distribution can be described by a normal distribution with mean $\mu=0$ and standard deviation $\sigma=1.667^\circ$. Namely, it is given by the equation [47]:

$$f(\theta) = \frac{1}{\sigma \cdot (2\pi)^{\frac{1}{2}}} \cdot e^{-\frac{\theta^2}{2\sigma^2}} \quad (3.15)$$

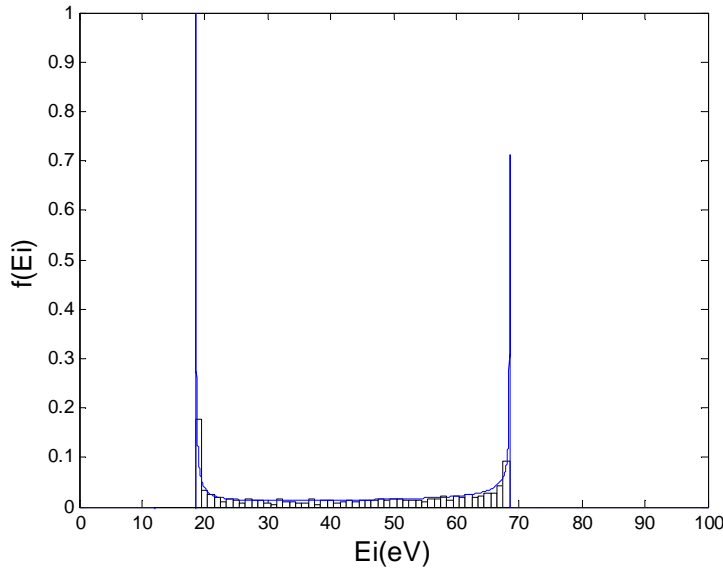


Figure 3.6: Depiction of the curve that corresponds to the theoretical pdf of ion energy, superimposed on the probability density histogram of the generated random numbers.

The sampling of random angles from the above mentioned distribution (equation 3.15) is implemented by the rejection-acceptance method. The results of this method are presented in figure 3.7, where the probability

density histogram of 1000 generated random ion angles is produced. Simultaneously, the curve that corresponds to the theoretical probability density function of ions angle is superimposed upon the histogram.

Assuming that the energy and the angle that an electron has near the wafer are independent [47], the probability density function of both energy and angle of electrons (IEADF) can be derived by the equation:

$$f(E_i, \theta) = f(E_i) \cdot f(\theta) \quad (3.16)$$

For the production of random variables of the IEADF the rejection-acceptance method is used. The figure of IEADF and the corresponding probability density histogram implemented by 1000 samples are presented in figures 3.8 and 3.9 respectively.

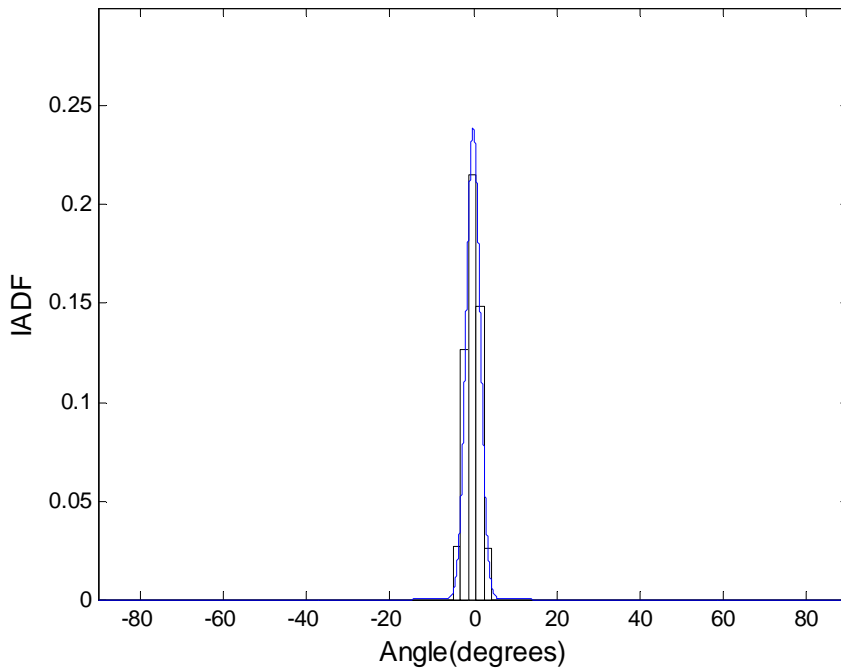


Figure 3.7: The curve that corresponds to the theoretical pdf of ion angular distribution, superimposed on the probability density histogram of the generated random numbers.

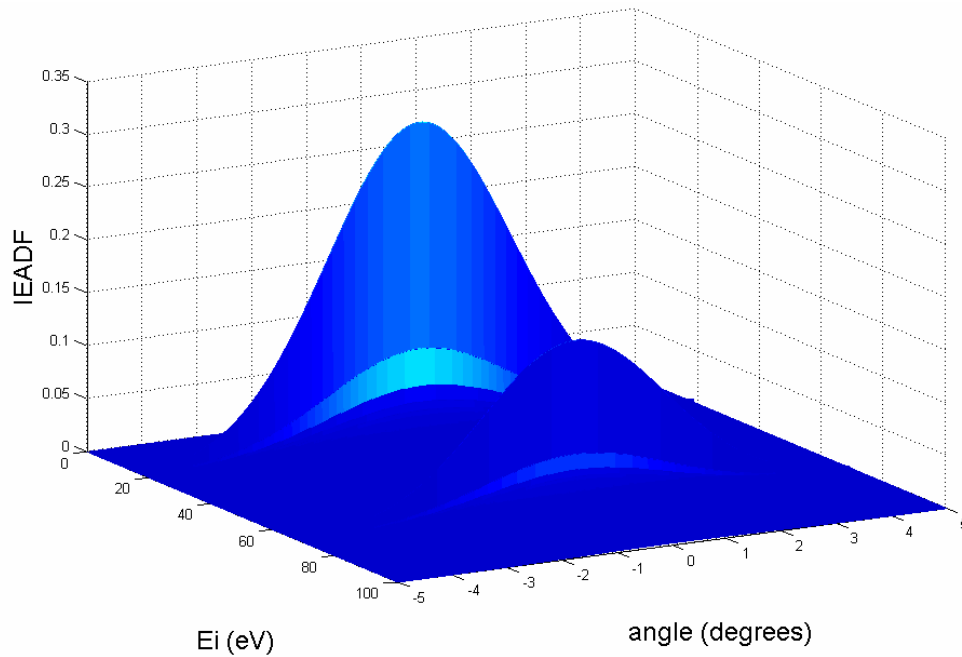


Figure 3.8: IEADF, coming from equations 3.14, 3.15, and 3.16.

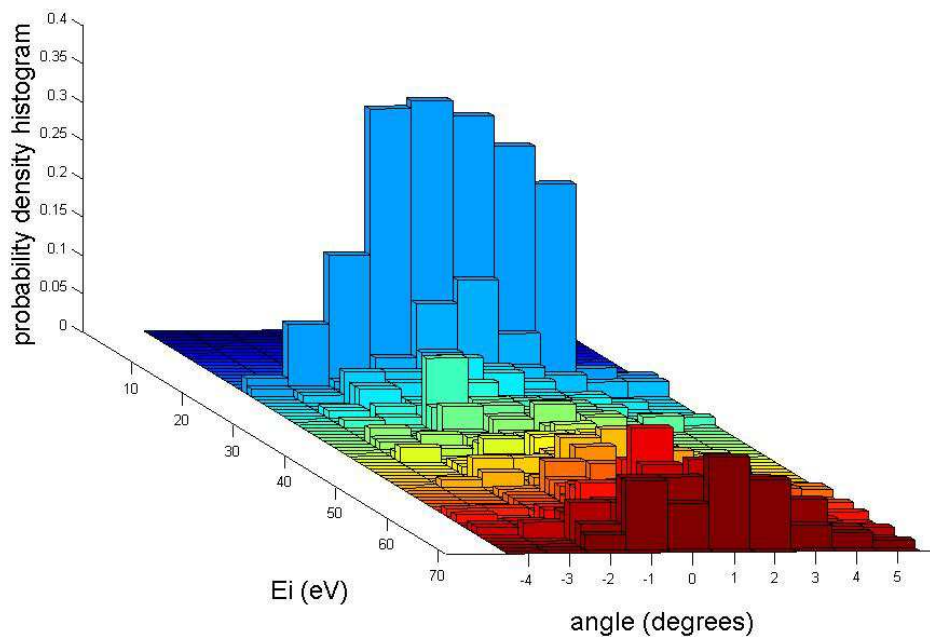


Figure 3.9: The probability density histogram corresponding to the IEADF of figure 3.8. The sampling is implemented by the acceptance-rejection method. 1000 samples were used.

The ions are distributed near the surface of the wafer accordingly to the IEADF that is described by equation 3.16. Thus, an ion that enters the inlet of the simulation domain has a specific value of energy and angle that is determined by this IEADF. In addition to that, provided that the potentials associated with the surface charge density influence the region just above the microstructure [12], i.e. the ions have only kinetic energy when they enter the

domain, the velocity coordinates of an ion that enters the domain can be calculated by the following equations

$$(u_x^2 + u_y^2) = \left(\frac{2E_{ion}}{m_{ion}}\right) \quad (3.17)$$

and

$$\tan\theta = \frac{u_x}{u_y}. \quad (3.18)$$

After a little algebra²³, it can be concluded

$$u_x = \left(\frac{2E_{ion}}{m_{ion}}\right)^{\frac{1}{2}} \cdot \left\{ \left[\frac{(\tan\theta)^2}{(1+(\tan\theta)^2)} \right] \right\}^{\frac{1}{2}} \quad (3.19)$$

and

$$u_y = \left(\frac{2E_{ion}}{m_{ion}}\right)^{\frac{1}{2}} \cdot \left[\frac{1}{(1+(\tan\theta)^2)} \right]^{\frac{1}{2}} \quad (3.20)$$

To summarize, the acceptance-rejection method is used in order to sample a pair of energy and angle value per ion from the appropriate IEADF. Then, the velocity coordinates are computed by the equations 3.19 and 3.20. This procedure is implemented by an appropriate matlab function.

3.2.2.3 Electron velocities at the inlet of the domain

Electrons enter the inlet of the simulation domain with a maxwelian energy distribution which can be described by the equation [44]

²³Specifically, it applies

$$(u_y^2 + u_x^2 \cdot (\tan\theta)^2) = \left(\frac{2E_{ion}}{m_{ion}}\right) \Rightarrow u_y^2 \cdot (1 + (\tan\theta)^2) = \left(\frac{2E_{ion}}{m_{ion}}\right) \Rightarrow u_y^2 = \left(\frac{2E_{ion}}{m_{ion}}\right) \cdot \frac{1}{(1+(\tan\theta)^2)} \Rightarrow$$

$$\Rightarrow u_y = \left(\frac{2E_{ion}}{m_{ion}}\right)^{\frac{1}{2}} \cdot \left[\frac{1}{(1+(\tan\theta)^2)} \right]^{\frac{1}{2}}. \text{ Thus, it occurs}$$

$$\left(\frac{2E_{ion}}{m_{ion}}\right) \cdot \left[\frac{1}{(1+(\tan\theta)^2)} \right] + u_x^2 = \left(\frac{2E_{ion}}{m_{ion}}\right) \Rightarrow u_x^2 = \left(\frac{2E_{ion}}{m_{ion}}\right) - \left(\frac{2E_{ion}}{m_{ion}}\right) \cdot \left[\frac{1}{(1+(\tan\theta)^2)} \right] \Rightarrow$$

$$\Rightarrow u_x^2 = \left(\frac{2E_{ion}}{m_{ion}}\right) \cdot \left\{ 1 - \left[\frac{1}{(1+(\tan\theta)^2)} \right] \right\} \Rightarrow u_x = \left(\frac{2E_{ion}}{m_{ion}}\right)^{\frac{1}{2}} \cdot \left\{ \left[\frac{(\tan\theta)^2}{(1+(\tan\theta)^2)} \right] \right\}^{\frac{1}{2}}$$

$$f(\varepsilon) = 2.07 \langle \varepsilon \rangle^{-\frac{3}{2}} \frac{1}{\varepsilon^2} e^{-1.5 \frac{\varepsilon}{\langle \varepsilon \rangle}}, \quad (3.21)$$

where

$$\langle \varepsilon \rangle = \frac{3}{2} k_B T_e \quad (3.22)$$

is the average kinetic energy of an electron [45]. If the electrons are assumed to have a temperature of $k_B T_e = 4\text{eV}$, thus $\langle \varepsilon \rangle = 6\text{eV}$. The equation (3.21) is first multiplied with the proper factor in order to be normalized. The sampling of random variables of energy from the above mentioned distribution is implemented by the rejection-acceptance method [47]. The results of this method is presented in figure 3.10, where the probability density histogram of 1000 generated random energies is produced. Simultaneously, the curve which corresponds to the theoretical probability density function of electron energy is superimposed upon the histogram.

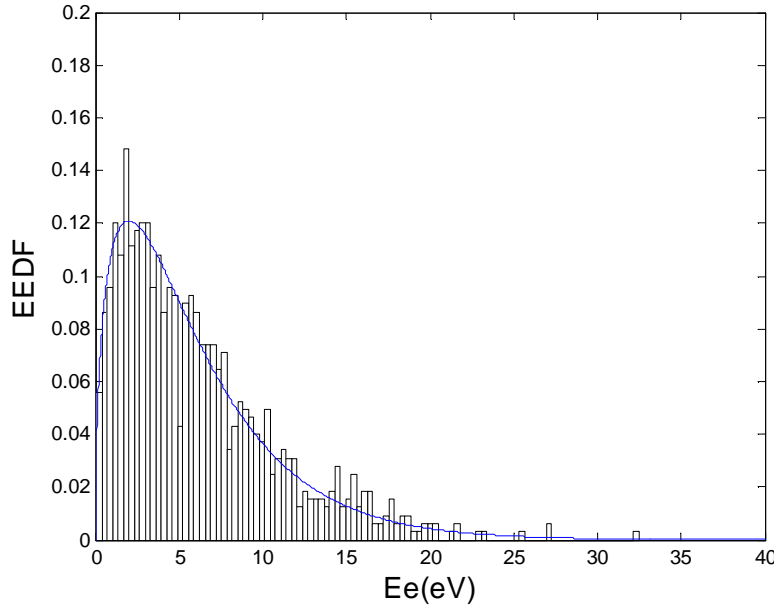


Figure 3.10: Depiction of the curve that corresponds to the theoretical pdf of electron energy, superimposed on the probability density histogram of the generated random numbers.

As far as the angular distribution of electrons is concerned, the electrons enter the upper boundary with an isotropic flux distribution and they are decelerated as they traverse the sheath. Consequently, their angular distribution broadens and near the wafer, it can be described by the equation [12]:

$$f(\theta) = \cos^n \theta, \quad (3.23)$$

where $n=0.6$. The equation (3.23) must be multiplied with the proper factor in order to be normalized in the region of angles from $\theta = -90^\circ$ to $\theta = 90^\circ$. The sampling of random angles from the above mentioned distribution is implemented by the rejection-acceptance method. The results of this method is presented in figure 3.11, where the probability density histogram of 1000

generated random electron angles is produced. Simultaneously, the curve that corresponds to the theoretical probability density function of electrons angle is superimposed upon the histogram.

Assuming that the energy and the angle that an electron has near the wafer are independent events, the probability density function of both energy and angle of electrons (EEADF) can be derived by the equation:

$$f(\epsilon, \theta) = f(\epsilon) * f(\theta) . \quad (3.24)$$

For the production of random variables of the EEADF the rejection-acceptance method is used. The EEADF and the probability density histogram are presented in figures 3.12 and 3.13 respectively.

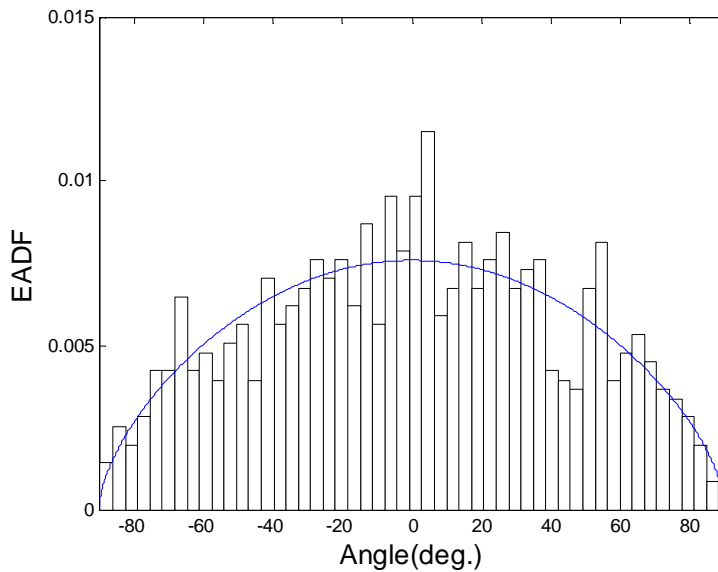


Figure 3.11: The curve that corresponds to the theoretical pdf of electron angular distribution, superimposed on the probability density histogram of the generated random numbers.

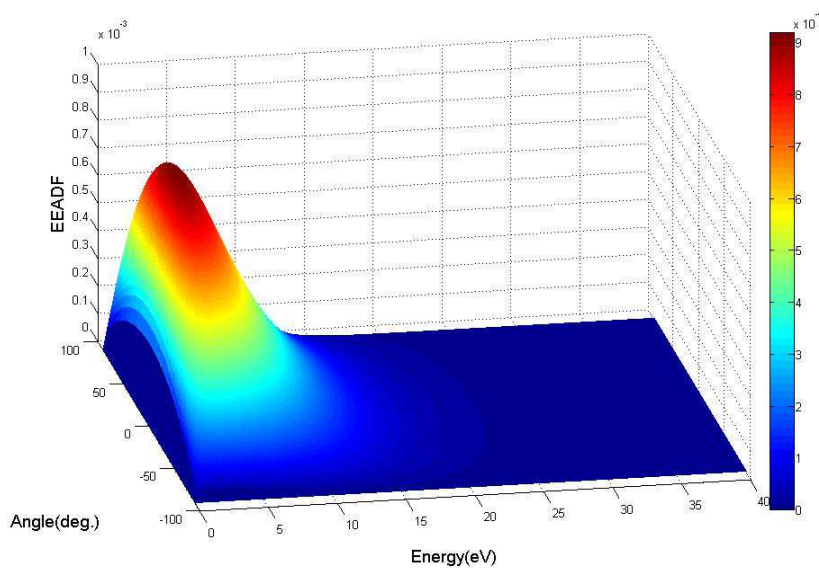


Figure 3.12: The EEADF, coming from the equation 3.21, 3.22 and 3.24.

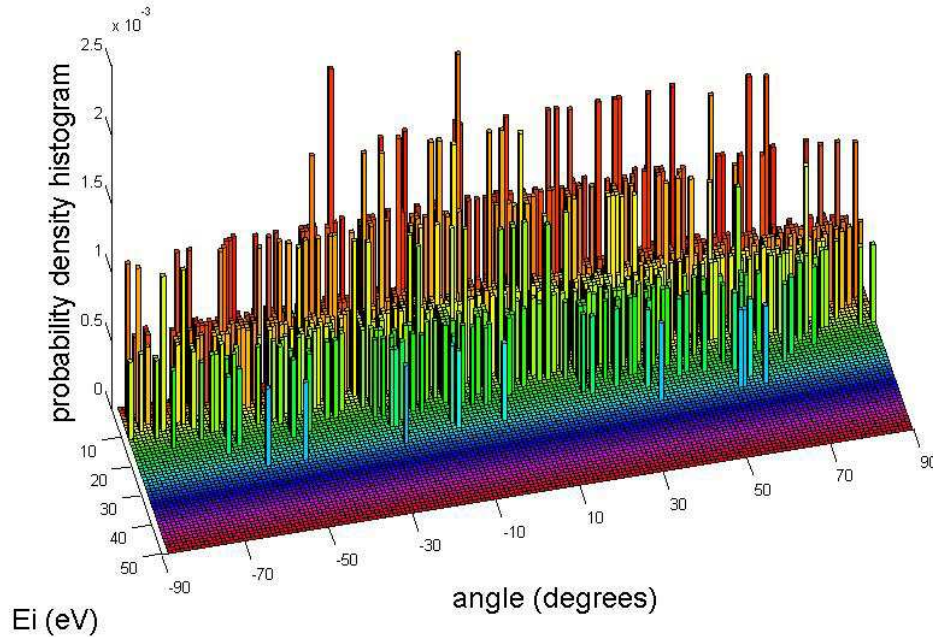


Figure 3.13: Depiction of the probability density histogram corresponding to the above mentioned EEADF. The sampling is implemented by the acceptance-rejection method. 1000 samples were used.

For the estimation of the electron velocities, the method that was used for the ions and is described above is followed. Consequently, the following equations ensue

$$u_{ex} = \left(\frac{2E_{\text{electron}}}{m_{\text{electron}}} \right)^{\frac{1}{2}} \cdot \left\{ \left[\frac{(\tan\theta)^2}{(1 + (\tan\theta)^2)} \right] \right\}^{\frac{1}{2}} \quad (3.25)$$

and

$$u_{ey} = \left(\frac{2E_{\text{electron}}}{m_{\text{electron}}} \right)^{\frac{1}{2}} \cdot \left[\frac{1}{(1 + (\tan\theta)^2)} \right]^{\frac{1}{2}} \quad (3.26)$$

Conclusively, the acceptance-rejection method is used in order to sample a pair of energy and angle value per electron from the appropriate EEADF. Then, the velocity coordinates are computed by the equations 3.25 and 3.26. This procedure is implemented by a matlab function.

3.2.3 Ion and electron trajectories simulation

In our simulation, the trajectory of a particle is calculated by solving a system of ordinary differential equations. This system is derived by the second Newton law

$$\vec{F} = m \cdot \vec{a} \quad (3.27)$$

where \vec{F} is the electrostatic force acting on the particle, \vec{a} is particle acceleration and m its mass. Specifically, from equation (3.27) it yields

$$\left[\begin{array}{l} \frac{dx}{dt} = u_x \\ \frac{dy}{dt} = u_y \\ \frac{du_x}{dt} = \frac{q}{m} E_x(x, y) \\ \frac{du_y}{dt} = \frac{q}{m} E_y(x, y) \end{array} \right] \quad (3.28)$$

where x is the particle position coordinate in the x axis, y is the particle position coordinate in the y axis, u_x is the particle velocity component in the x axis, u_y is the particle velocity component in the y axis, q is the charge of the particle, m is the mass of the particle, and ultimately E_x and E_y are the electric field components in the two dimensional space of the simulation domain. This field is a spatially varying electric field calculated by the third sub-model.

Obviously, the aforementioned system can not be solved with an analytical method. Consequently, for the simulation of the particles trajectories, a matlab solver, namely the ode15 solver, is used.

Wherever in the simulation we need the values of E_x and E_y , we call a matlab function, namely `TriScatteredInterp`, for the interpolation.

Necessary for the calculation of particle trajectories are conditions that should be imposed on the boundaries of the simulation domain. The trajectory calculation is terminated when the particle impinges on the trench boundary, that is the dielectric pattern. In the case of strong repulsion, the same condition applies for the upper boundary, i.e. the inlet of the domain. A specific option of the used solver provides a means to implement such conditions. It works by solving differential equations until one of the dependent variables or a function of them reaches a particular value. For instance, when a repelled particle is return to the inlet, its position y component has a specific value, i.e. the determined y value of the inlet, for which the process is terminated. In the case of the trench boundary, the signed distance function²⁴ [48] from it is utilized (figure 3.14). The signed distance function of the boundary is obtained by solving the Eikonal equation

²⁴ A signed distance function is an implicit function ϕ with $|\phi(\vec{x})| = d(\vec{x})$ for all \vec{x} , where $d(\vec{x}) = \min(\vec{x} - \vec{x}_i)$ for all $\vec{x}_i \in \partial\Omega$. $\partial\Omega$ represents the set of boundary points. The term 'implicit' can be justified from the fact that ϕ basically represents the isocontours of a higher dimension function.

$$F(x) \cdot |\nabla T(x)| = 1 \quad (3.29)$$

with the fast marching method [49]. Typically, such a problem describes the evolution of a boundary as a function of time T with speed $F(x) > 0$, i.e. the boundary grows outward, in the normal direction at a point x on the curve. Thus, the signed function values, depict the evolving positions of the boundary as time elapses, assuming it moves isotropically with velocity $F=1$.

When the signed distance at the position of a particle becomes less or equal to zero, the trajectory is terminated. The scattered values of the signed distance function are interpolated in a similar way that was described previously (by the `TriScatteredInterp` function of Matlab).

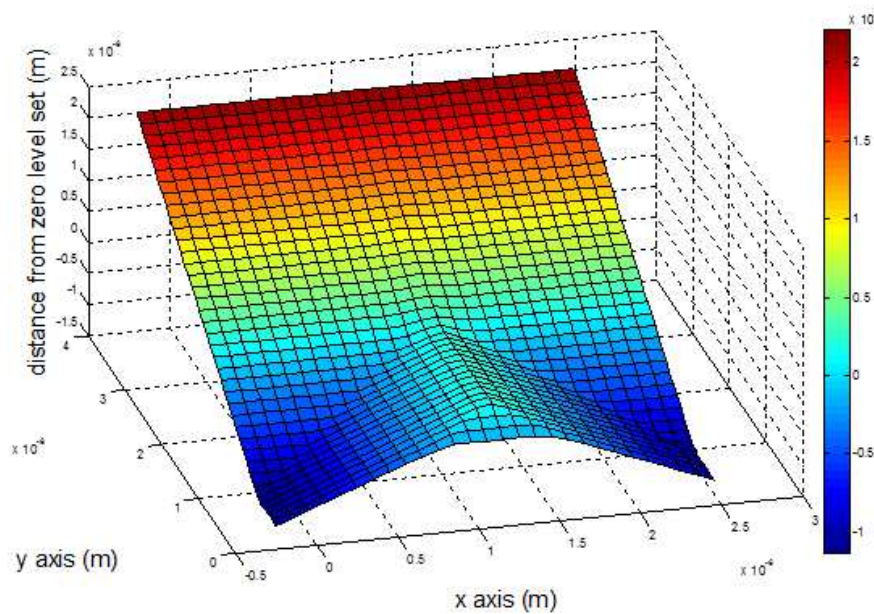


Figure 3.14: Signed distance from a trench boundary

Additionally, when a particle reaches the left or right wall of the simulation area, the particle continuity condition [17, 19] is activated. More precisely, the trajectories of the particles, which abandon the simulation area and traverse the wall boundaries, are mirrored with respect the y axis. This means that the tracing of the simulated particle continues; its position is shifted to the other wall boundary, from left to right or from right to left.

As far as the initial conditions are concerned, an initial position and velocity is attributed to each particle. Specifically, a uniform distribution is used for the selection of the initial position at the inlet of the domain. Moreover, realistic ion and electron energy and angular distributions at the wafer are utilized for the calculation of particles initial velocities, as described in section 3.2.2.

To end this section, a demonstration of 100 ions and electrons calculated trajectories after steady state has been reached follows in figures 3.15 and 3.16 respectively. The steady state electrostatic potential that alters the

particle trajectories is also depicted in figure 3.17. Note the severe repulsion that ions undergo inside the trench. Interesting also appears to be the repulsion that electrons undergo near the upper part of the sidewalls. A vast amount of electrons comes from the side boundaries due to particle continuity condition.

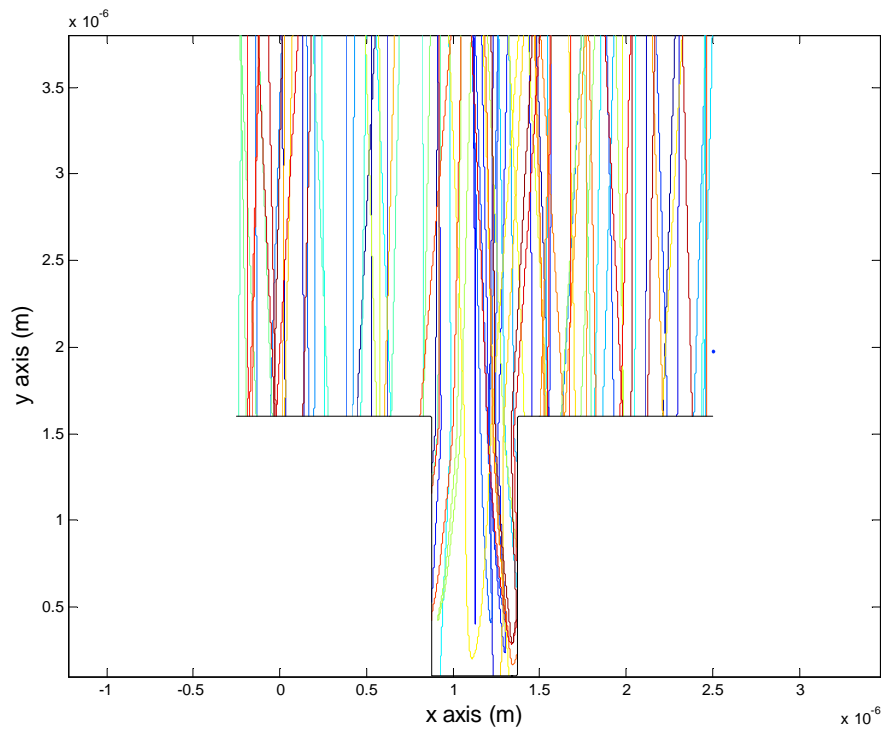


Figure 3.15: Calculated trajectories of ions starting at the inlet, after steady state has been reached.

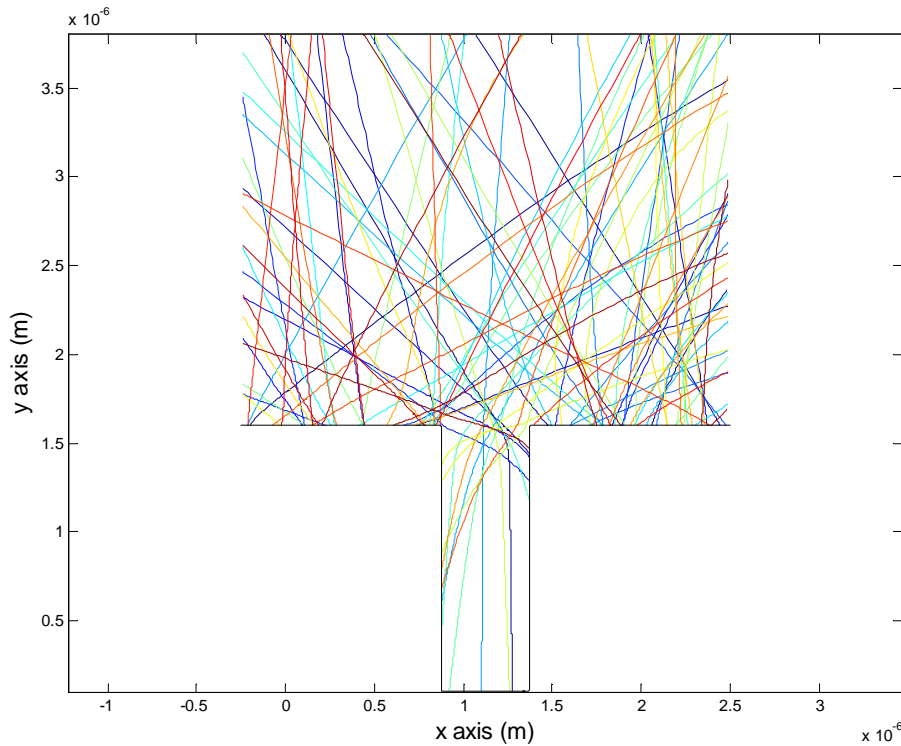


Figure 3.16: Calculated trajectories of electrons starting at the inlet, after steady state has been reached. Some electrons come from the side boundaries due to particle continuity.

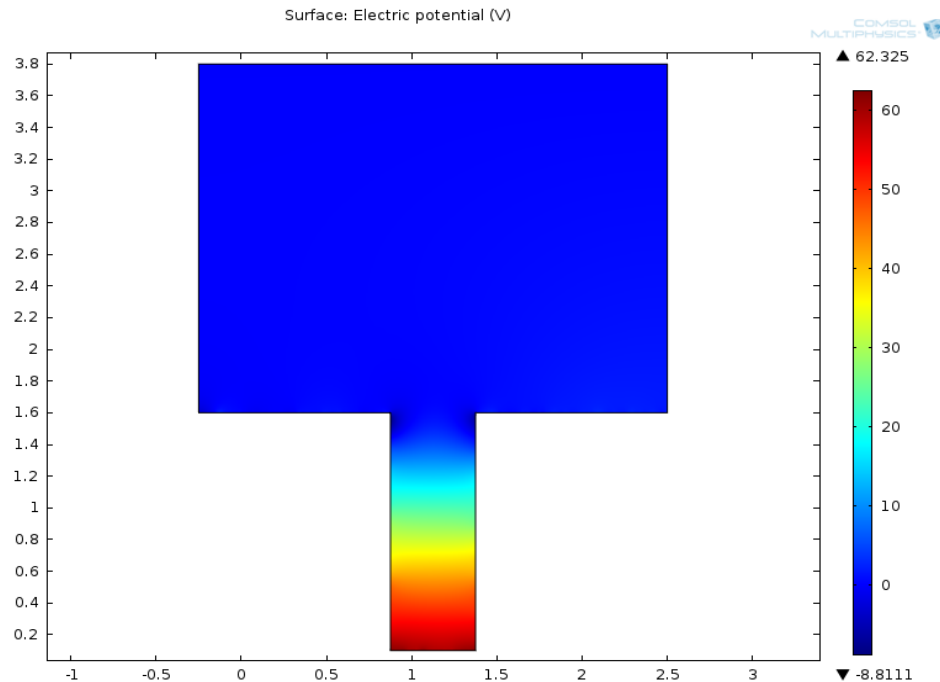


Figure 3.17: Potential distribution map at steady state charging. Notice how the most positive and negative regions influence ions and electrons respectively in regard to figures 3.15 and 3.16.

3.2.4 The utility of superparticles

In order to accelerate our simulation, superparticles are used. A superparticle is a computational particle that represents many real particles, for example 10^6 - 10^9 real particles [54]. The concept of superparticle is borrowed from the particle in cell (PIC) method [50]. It should be mentioned that a superparticle will follow the same trajectory as a real particle would because the Lorentz force depends only on the charge to mass ratio.²⁵ 250 ion and electron superparticles are generated every charging step, and each superparticle represents $3 \cdot 10^6$ particles.

The reason for using many superparticles (500 superparticles every step) is to reduce stochastic noise [17]. More precisely, when the magnitude of superparticles is increased and concurrently the number of superparticles (that are released per cycle) is decreased, steady state potential value oscillates severely. This leads to the appearance of large fluctuations in the average steady state potential. This is because, when a smaller number of superparticles is utilized per cycle, the amount of superions that reach the trench bottom per cycle is remarkably reduced. Besides, a superparticle carries a larger amount of particles. Consequently, more abrupt fields arise along the surface per cycle. Indeed, negative and positive potential regions on the microstructure are more restricted, abrupt and stronger, thus a not so smooth potential distribution emerges. Simultaneously, a superparticle trajectory is affected in the same way with a simple particle. The above assertions indicate that there will be less energetic ions to overcome the potential inside the trench per cycle. Indeed, from a statistical point of view, there will be steps where no superions arrive at the bottom. Nonetheless, one or more electrons may arrive at the trench bottom in that case. Thus, the steady state potential will significantly be reduced and an intense negative displacement of the potential will emerge. However, in the next steps the potential will rise again, as current balance is immediately restored, until the phenomenon will be repeated. Thus, the negative displacement occurs in a periodical way, i.e. potential oscillates. Consequently, the number of superparticles that are utilized per cycle must be small enough in order to accelerate the simulation process and concurrently large enough in order to avoid large potential negative displacements which lead in intense oscillation and, in turn, severe fluctuations superimposed on the average steady state potential (see appendix II).

²⁵ From Newton's second law and assuming that plasma is not subjected to any magnetic

$$\text{field: } \vec{a} = \frac{q \cdot (\text{magnitude of superparticle})}{m \cdot (\text{magnitude of superparticle})} \cdot \vec{E} = \frac{q}{m} \cdot \vec{E} .$$

3.3 Surface charge density calculation model

3.3.1 Particle distribution on the down boundary

3.3.1.1 Introduction

The calculation of the surface charge density on the trench boundary requires the segmentation of the trench boundary and the counting of the charged particles (ions and electrons) arriving at each one segment. However, there are some technical difficulties on the identification of the segment that a particle arrives at (belongs to).

Due to precision issues, it is impossible for a particle trajectory to stop exactly on the trench boundary. This is associated with the integration steps that the matlab solver follows in order to compute a particle trajectory. By reducing the solver maximum step, the situation is improved but at the same time the simulation time is severely increased. Thus, this is not the solution. Inevitably, the final integration step may end slightly below the trench boundary.

In order to overcome these difficulties, the trench boundary is given an artificial thickness and the identification problem is reduced to finding whether a point, i.e. particle position, lies inside a parallelogram or not.

This method can be applied to any type of segment, vertical, horizontal or oblique. However, for the presentation of the method, a horizontal segment is used.

In this section, the realization of the segmentation of the domain's down boundary is presented. Subsequently, the method of counting the particles in each segment is demonstrated.

3.3.1.2 The segmentation of the boundary

First, the length of the trench boundary is found. For this purpose, its coordinates are extracted from the mesh used for the solution of the third sub-model (Laplace equation). Then straight lines are joined between consecutive boundary points which are determined by the aforementioned coordinates. The length²⁶ of each straight line is added to the previous calculated one in a successive way. In this way, the total length of the boundary is computed.

Subsequently, equidistant points along the boundary are generated. In this manner, the boundary is comprised of equivalent segments. The length of each segment is given by the expression

$$s(i+1) - s(i) = \frac{b-a}{n-1} \quad (3.30)$$

²⁶ The length of each segment, defined by points $(x(i), y(i))$ and $(x(i+1), y(i+1))$ is equal to $\sqrt{(x(i+1)-x(i))^2 + (y(i+1)-y(i))^2}$ where $x(i)$, $y(i)$ are the boundary coordinates.

where $s(i)$, $s(i+1)$ are the arclengths of two successive points on the boundary, $b-a$ the length of the boundary and n the total number of points. It was found that a number of 1000 points is adequate for the accuracy of the electrostatic potential.

But how can the coordinates of the above mentioned equidistant points be estimated? This is a simple linear interpolation problem. The matlab function that does this interpolation is $V = \text{interp1}(u, v, U)$. In our case, u is a vector that contains the aforementioned values of the increasing arc length, v is the vector which contains either the y coordinates of the boundary or the x coordinates of the boundary and U is the vector which includes the equidistant points s . V is the ensuing vector of the process that holds either the x (V_x) or the y coordinates (V_y) of the equidistant points according to the values of v . Consequently, the vectors V_x and V_y holds the limits of the equidistant segments above the boundary.

In the figure 3.18, both the extracted coordinates and the calculated limits of the segments of the boundary are presented.

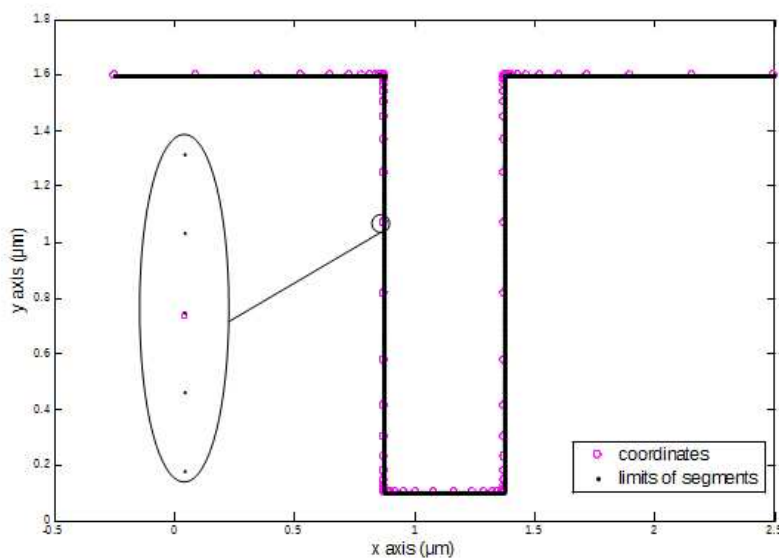


Figure 3.18: Generating equal and equidistant segments across the arc length of the boundary. These segments will be utilized for the distribution of the particles on the boundary. It should be mentioned that in the above picture, for the coordinates extraction a coarse mesh was used so that the distinguish between coordinates and limits of the segments be illustrative. During the simulation process, a extremely dense mesh is used.

3.3.1.3 The particle distribution algorithm.

3.3.1.3 The particle distribution algorithm.

The distribution of the particles on the equidistant segments of the trench boundary requires the thickening of the trench boundary. Essentially, each line segment, is substituted by a rectangle. The counting of particles on segments is substituted by the counting of particles lying inside rectangles. For a detailed presentation of the algorithm, see appendix III.

3.3.2 Surface charge density calculation

3.3.2.1 Using linear instead of surface charge density

The trench is assumed to have the same shape along the z axis, thus the charging should not vary along that direction [14, 19, 33]. This means that the electric field parallel to that axis must be negligible compared to the field in the transverse coordinates.²⁷ Consequently, a two dimensional approach can be utilized for the calculation of the electric field and this can be implemented by restricting our attention to the cross section of the trench. Additionally, due to the absence of an electric field component at that direction, the z velocity component is also neglected as the particles thermal energy is much smaller than their directional kinetic energy in the 2d region [51].

Owing to the aforementioned 2d approximation, a line charge density can be estimated instead of a surface charge density. Both types of densities are equivalent. Indeed, assume that the charge accumulated at the bottom of a random 2d trench is that shown in figure 3.19. Then the linear charge density (2d approach) at the bottom is 0.6366 C/m.

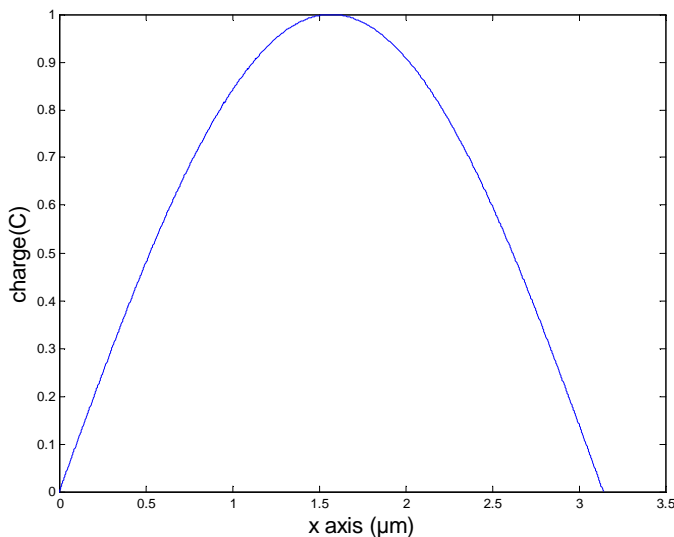


Figure 3.19: Charge distribution at the bottom of a random 2d trench.

Taking into consideration the out of plane thickness of the above 2d trench, the surface charge density at its bottom is shown in figure 3.20. The value is (3d approach) 0.6366 C/m^2 .

The 2d approximation is much faster than the full 3d approach. Indeed, introducing a new dimension to a 2d calculation requires more computational power and more particles to obtain an accurate solution.

²⁷ The gradient of the electric potential is negligible to that direction.

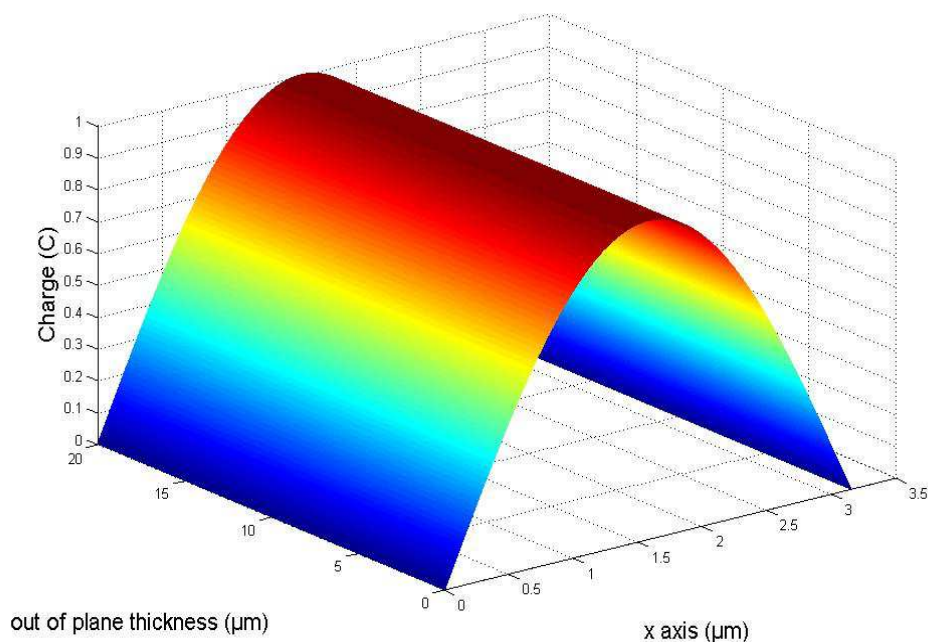


Figure 3.20: Ensuing charge distribution at the bottom of the aforementioned 2d trench when extending to 3 dimensions. The length of the out of plane thickness is indicative. The result is the same for any value. The shape of the charge function is random.

3.3.2.2 The method of calculation

After every charging step, the number of superparticles that have currently impinged on each segment, multiplied by the superparticle magnitude, is divided with the length of the segment. The superparticles counting is realized with the parallelogram method described in appendix III. In this manner, local linear charge densities above the microstructure are estimated. By using superparticles, the resulting electrostatic force field, which its estimation is based on the aforementioned local linear charge densities, becomes significant enough to alter ion and electrons trajectories after a few steps and steady state is reached in remarkably less simulation time than the case of releasing just simple particles per step. The charging process is tremendously hastened.

3.4 Charging potential calculation model

3.4.1 Imposing the proper boundary conditions

As it has been already mentioned, the third sub-model takes the surface charge density from the second sub-model and calculates the potential distribution in the domain by solving the Laplace equation²⁸

²⁸ Laplace equation is one of the most important partial differential equations in physics named after French mathematician Pierre-Simon Laplace (1740–1827). Here Laplace equation describes the electrostatic potential in a charge free region, i.e. the simulation domain. Since the electric field is given by the gradient of a potential $E = -\nabla V$ and the divergent of E is equal to zero in a free space (Gauss's Law), it ensues $\nabla E = -\nabla \cdot \nabla V = -\nabla^2 V = 0$, thus $\nabla^2 V = 0$.

$$\nabla^2 V = 0 \quad (3.41)$$

subjected to the following boundary conditions²⁹ [12, 19]:

$$V=0 \quad (3.42)$$

along the sheath lower boundary, i.e. at a plane located 3.7 μm above the dielectric surface,

$$\vec{n} \cdot \vec{D} = 0 \quad (3.43)$$

at vertical boundaries located to the left and right of the exposed surface and

$$\vec{n} \cdot \vec{D} = \sigma \quad (3.44)$$

at the exposed surface. \vec{D} is the electric displacement,³⁰ \vec{n} is the unit vector perpendicular to the boundary and in the latter condition, σ is the surface charge density that emerges from the particles distribution along the dielectric pattern. The estimation of σ is described in the section 3.2.4.

It must be mentioned that the charging potential affects the particles only near the microstructure [12, 19]. This is the reason why the potential decays to zero at short distance above the dielectric pattern, i.e. condition (3.42). Owing to this, the whole simulation process is simplified as it can be separated in two independent parts, the calculation of particle energy and angular flux distributions and the modeling of microstructure charging.

²⁹ In mathematics, in the field of differential equations, a boundary value problem is a differential equation together with a set of additional restraints, called the boundary conditions. A solution to a boundary value problem is a solution to the differential equation which also satisfies the boundary conditions. If the boundary condition gives a value to the normal derivative of the problem then it is a Neumann boundary condition. If the boundary condition gives a value to the problem then it is a Dirichlet boundary condition.

³⁰ To describe electromagnetic fields in matter, it is convenient to introduce the electric displacement field \vec{D} . More precisely, in dielectrics, one usually makes the approximation that the electric field induces tiny dipoles, which are described by the electric polarization \vec{P} . The effect of polarization is to produce accumulations of bound charge, within the dielectric and on the surface. Obviously, the bound charge induces additional electric fields. A little bit of calculation shows that these supplementary charges can be conveniently hidden by introducing the electrical displacement field \vec{D} , which then fulfils the equation $\nabla \vec{D} = \sigma_f$ or in integral form $\oint_S \vec{D} \cdot d\vec{a} = Q_{f,enc}$. This is nothing more but a particularly useful way to express

Gauss's law in the context of dielectrics, because it makes reference only to free charges and free charges is what is known initially in an electrostatics problem.

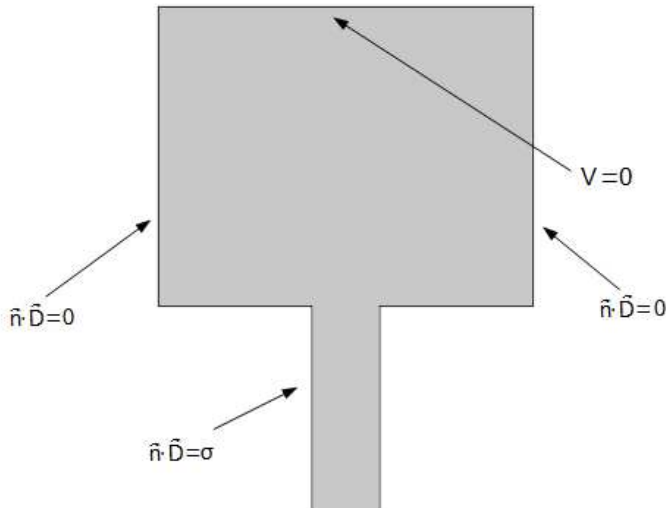


Figure 3.21: Boundary conditions imposed on the entire simulation domain.

But what is the meaning of the three Neumann conditions? Well, to answer this question we must first imagine a free charge density σ distributed on an arbitrary interface between two dielectric media. Suppose we draw a wafer-thin Gaussian pillbox extending just barely over the edge in each direction. Gauss's law³¹ in terms of electric displacement states that

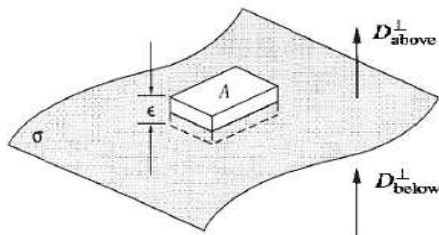


Figure 3.22: the electric displacement field always undergoes a discontinuity when you cross a surface charge σ . [55]

$$\oint_S \vec{D} \cdot d\vec{a} = Q_{\text{enc}} = \sigma \cdot A, \quad (3.45)$$

where A is the area of the pillbox lid. Now, the sides of the pillbox contribute nothing to the electric flux in the limit as the thickness ϵ goes to zero. So we are left with

$$D_{\text{above}}^{\perp} - D_{\text{below}}^{\perp} = \sigma \quad (3.46)$$

³¹ This suggests that the flux through any closed surface is a measure of the total charge inside. For the field lines that originate on a positive charge must either pass out through the surface or else terminate on a negative charge inside. On the other hand, a charge outside the surface will contribute nothing to the total flux, since its field lines pass in one side and out the other. This is the essence of Gauss's law.

where D_{above}^{\perp} denotes the component of \vec{D} that is perpendicular to the surface immediately above, and D_{below}^{\perp} is the same, only just below the surface.

Consequently, the boundary condition on \vec{D} can be written:

$$\hat{n} \cdot (\vec{D}_1 - \vec{D}_2) = \sigma, \quad (3.47)$$

where \hat{n} is a unit vector perpendicular to the surface, pointing from "below" to "above", where "below" implies medium 2 and "above" implies medium 1. The indexes in electrical displacement vectors indicate the medium. In our case, the first medium, i.e. the simulation domain, is the vacuum. As far as the second medium is concerned, we neglect the thickness of the dielectric, thus $\vec{D}_2 = 0$. So condition (3.47) becomes

$$\vec{D}_1 \cdot \hat{n} = \sigma. \quad (3.48)$$

When $\sigma=0$, the above condition implies that the potential is symmetric with respect to the boundary that is imposed on. Thus, in order to mirror the simulation domain [12, 19], the condition (3.43) is imposed on both left and right boundary. In other words, imposing this condition the effect of charging potentials outside the simulation domain on the process is also considered

To end this section, an example of the evolving electrostatic potential for the first four steps is demonstrated. Note the gradual positive charging build up at at the dielectric trench bottom.

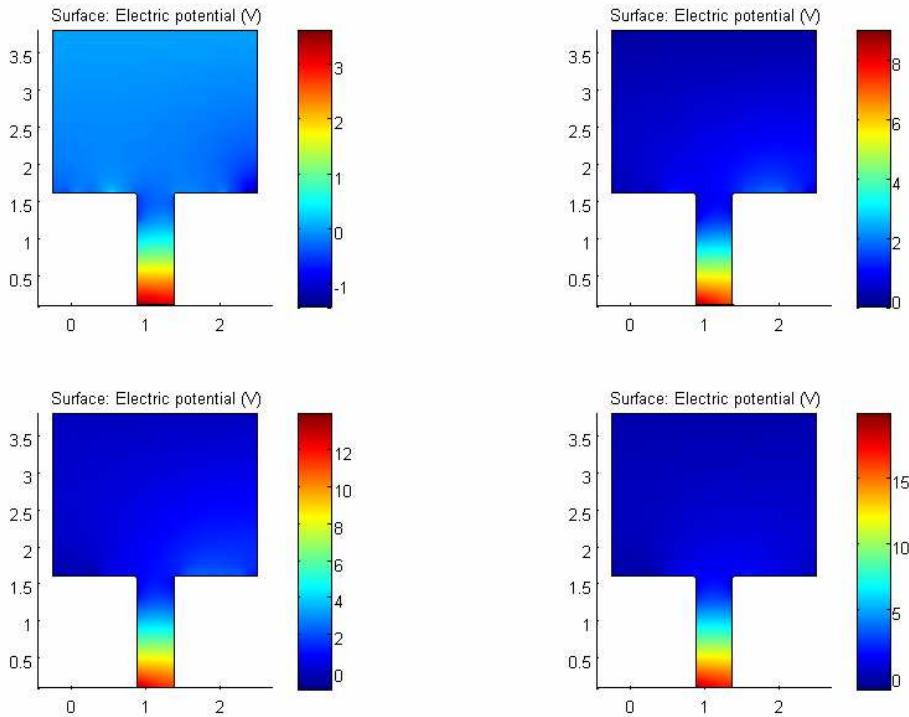


Figure 3.23: example of the electrostatic potential evolution during sequential charging steps. Results are obtained from comsol multiphysics software 4.3b.

3.4.2 The mesh of the simulation domain

Comsol approximates the solution of the Laplace equation with the utilization of the finite element method (FEM) [56] (see appendix IV). In our simulation we follow the triangulation process for the mesh construction. The type of basis functions is linear functions. It should be noted that it is not always efficient to make the triangles be all of essentially at the same size. Indeed, at places where the derivate of the potential is high, smaller triangles are used. On the other hand, in areas of small variation of the solution, larger ones are utilized. The ensuing mesh is presented in figure 3.24. It is consisted of 13600 triangular elements. At this mesh density, the solution is saturated.

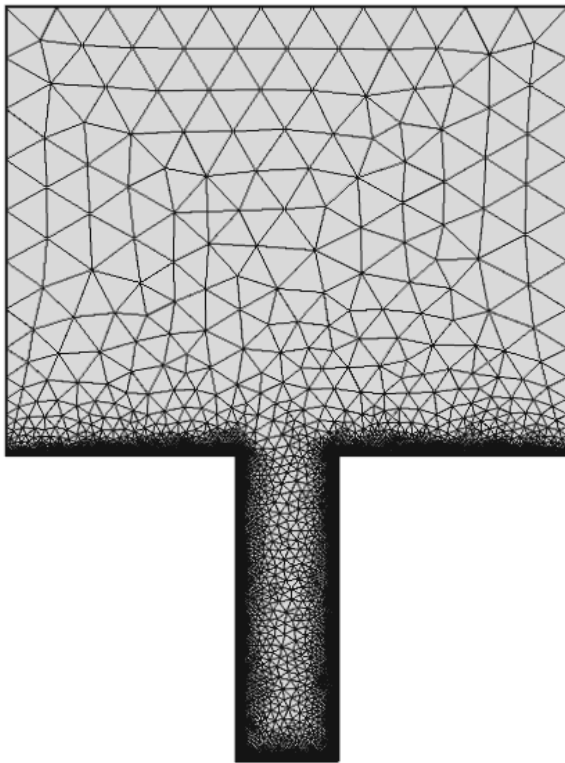


Figure 3.24: A triangulation of the simulation domain consisting of 13600 triangular elements. This triangulation was created using Comsol Multiphysics 4.3b.

The evaluation of the solution of the Laplace equation is implemented by electrostatics module of Comsol Multiphysics 4.3b [40]. But is this result accurate? For the purpose of answering the previously stated question, an analytical calculation of Laplace equation subjected to mixed boundary conditions, i.e. both Neumann and Dirichlet, is presented in appendix V. The geometry is much simpler than the above case, namely it is just a rectangular with width 4 cm and height 1 cm. Finally, the result is compared with the value that is derived by electrostatics module of Comsol 4.3b. A very good agreement between the analytical and numerical result ensues.

3.5 Computational cost and parallel implementation

Parallel computing techniques are utilized in order to reduce the simulation time in an efficient way. More precisely, our model involves multiple segments of code, some of which are repetitive and independent. The part of the particle trajectory simulation belongs to this category. We could use a simple for-loop to solve for the trajectory of each particle. However, matlab functionality to execute code on parallel can significantly improve performance. The only restriction on parallel loops is that no iterations are allowed to depend on any other iterations, a condition that is satisfied for particles trajectories simulation: a particle trajectory does not depend on any other particle trajectory in the same charging step. Execution in matlab begins with a single processor, the client. When a parfor loop is encountered, parfor is a way to run FOR loops in parallel, the client is helped by a "pool" of workers. Each worker is assigned some iterations of the loop.

Once the loop is completed, the client resumes control of the execution. Matlab ensures that the results are the same whether the program is executed sequentially, or with the help of workers. The results from workers are gathered using a specific command. Local configuration is chosen, that is, the cores assigned to be workers will be on the local machine. It can be up to 8 on a local machine. In this way, matlab can take advantage of a multicore desktop machine.

As it has been mentioned, a full sequential use of the sub-models (1, 2, and 3) consists a charging step. Note, in figure 3.25, how drastically the time execution for sub-model 1 (and consequently for the charging step) is decreased with the utilization of parallel loops. The run was conducted on a computer of the computer cluster [41] of the Department of Microelectronics of NCSR Demokritos.

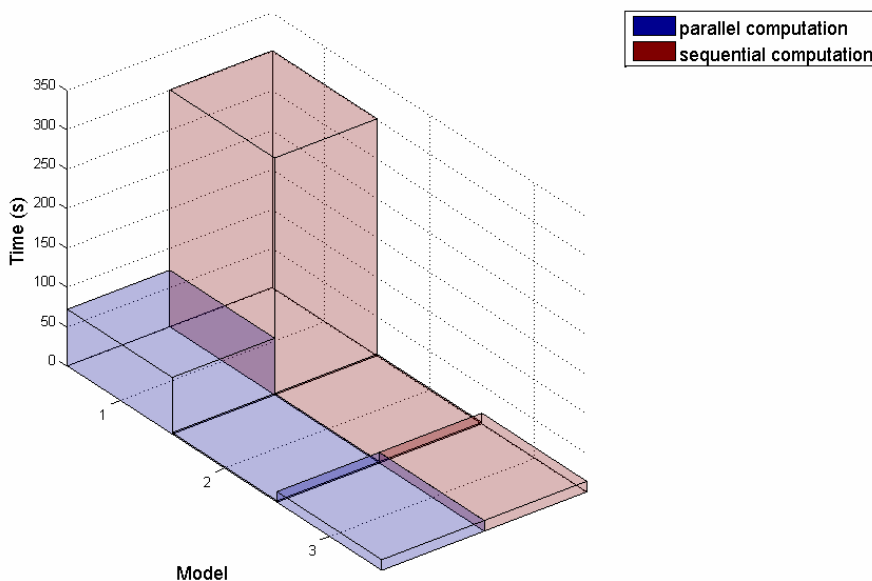


Figure 3.25: Parallel and sequential computation time comparison.

4 VERIFICATION AND RESULTS

4.1 Introduction

A systematic study on the influence of charging on etching of features (trenches) is performed. The impact of charging under different conditions and cases is investigated. In particular, the effect of a) the shape of the ion energy distribution function (IEDF), b) the average ion energy, c) the electron temperature, and d) aspect ratio (AR) of the feature on the local ion fluxes, etching yields, and rates is examined. For the calculation of the etching yield and rate a model for ion enhanced etching is considered. A verification and a self-consistency check of the model is preceded the study. The scaling of charging effects to the AR (rather than the absolute dimension) of the feature is checked and the model results are compared with a published work of Hwang and Giapis [15]. Ultimately, the effect of the distance of the inlet of particles from the trench is investigated.

4.2 Conditions, inputs and post data process of the simulation

An argon (Ar) plasma is employed. The geometry considered (figure 4.1) consists of a dielectric trench of width equal to $0.5\ \mu\text{m}$ and depth equal to $1.5\ \mu\text{m}$. The electron and ion temperature are taken to be 4 and 0.5 eV respectively. The distance between the inlet and the dielectric trench is $2.2\ \mu\text{m}$. The IEDF at the wafer is assumed to be bimodal. The ion angular distribution function is described by a normal distribution with mean $\mu=0$ and standard deviation $\sigma=1.667^\circ$ (equation 3.15, figure 3.6). The electron energy distribution function (EADF) is given by a maxwelian energy distribution (equation 3.21, figure 3.9). The electron angular distribution function is expressed by the equation 3.23 (figure 3.10).

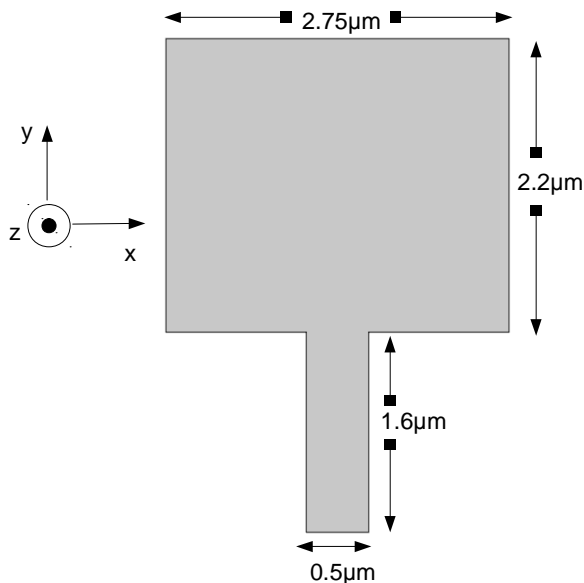


Figure 4.1: The geometry that determines the simulation domain of the model.

Our simulation model is executed in an iterative way until steady state potential is reached. For that purpose, hundreds of computational charging steps are needed. In each step, 250 superparticles of ions and 250 superparticles of electrons are released from the inlet. Each superparticle is consisted of $3 \cdot 10^6$ particles. Steady state is reached when the trench surface potential is stabilized. After the steady state point, 100 more charging steps are used. In this manner, the stochastic noise on the mean behavior of the charging potential surface distribution is reduced.

In our model, information related with the movement of the particles like the number of absorbed particles, energy, and incident angle at the surface structure can be acquired. By utilizing this data, the etching rate at each position on the structure can be calculated. In this way, the trend of the etching at the given microstructure can be predicted. We consider ion-enhanced plasma etching, presuming that the whole surface of the trench is fully covered by active radicals, thus the etching rate is only depended on the flux and energy of the incident ions. More precisely, the etching rate at the segment i of the dielectric boundary is calculated by the expression

$$ER_i = EY_i \cdot F_i, \quad (4.1)$$

where

$$EY_i = \frac{1}{N_i} \sum_{j=1}^{N_i} \left[\left(\sqrt{E_j} - \sqrt{E_{th}} \right) \cdot \cos \theta_{ij} \right] \quad (4.2)$$

is the etching yield (SiO_2 atoms/ion) at segment i of the trench boundary, N_i is the number of ions absorbed at the i segment, E_j is the energy of the impinging ion³², E_{th} is the threshold energy which is set to 4eV for SiO_2 etching [49] and θ_j is the ion's incident angle³³ on the segment. F_j is the ion flux at the corresponding segment.

In reality, steady state is reached in much less time than an actual etching profile evolution so etching is not considered during the charging transient [12, 19]. For this reason, the steady state ion flux is used in order for both the etching yield and the etching rate to be estimated.

4.3 Verification of the model

4.3.1 Comparison with Hwang and Giapis work.

In order to verify the model, a seminal work by Hwang and Giapis [15] was used as a benchmark. With the purpose to examine the accuracy of our simulation, both ion energy and angular distributions (IADF) as well as electron energy (EEDF) and angular distributions (EADF) were exactly the same with that utilized in the aforementioned work. More precisely, as far as

³² The energy of an impinging ion is calculated from its velocity components.

³³ Angle between velocity vector and normal vector at the segment. Both vectors point to the material.

the ions are concerned, data [12, 15] was obtained by a proper software though a digitization process and then it were imported to the model (for IEDF see figure 4.2, for IADF see figure 2.6a). As far as the electrons are concerned, their corresponding distributions were produced through functions that are provided from the literature [12] (see figure 3.9 and 3.10).

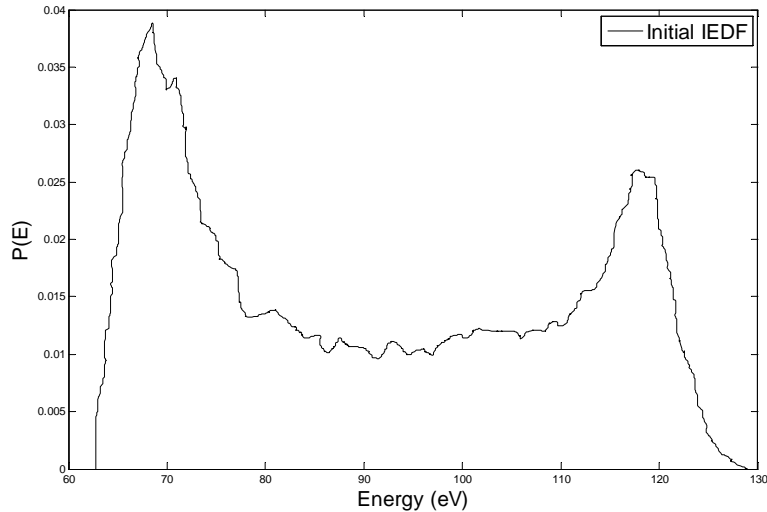


Figure 4.2: The initial IEDF that Hwang and Giapis used in their charging simulation process [15].

A comparison between the results of our simulation and that of Hwang and Giapis follows. As far as the charging potential distribution along the trench surface is concerned, the comparison is demonstrated in figure 4.3.

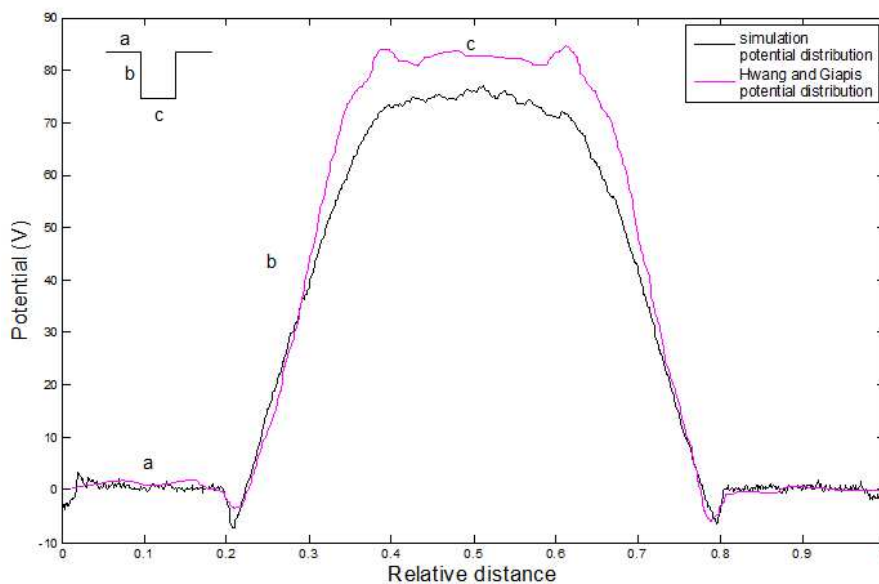


Figure 4.3: Charging potential distributions along the trench surface at AR (1.5:0.5). The length scales have been normalized by the length of the top segment in order to facilitate comparisons. Inset at the left top: The top, sidewall, and bottom segments of the trench arlength are denoted by a, b, and c.

There is a difference about 10 V as far as the trench bottom potential is concerned. The origin of this difference is the fact that the IADF in Hwang and Giapis simulation is energy dependent. The ions with normal to surface direction have greater energy compared to those with off-normal direction [12]. On the contrary, in our simulation, the release angle of an ion and its energy are independent (see section 3.2.2.2). In the former case, the closer to normal the direction of an ion is, the more energetic will be. Consequently, the number of ions with high energy arriving at the trench bottom is greater compared to the latter case (our simulation). In order to maintain current balance, a greater steady state potential at the bottom of the trench is required for the former case. Due to this greater steady state potential, the energy distribution of ions at the trench bottom is narrower. This is illustrated in figure 4.4.

With the purpose to confirm the above mentioned assumption, a narrower IADF was utilized in our simulation. In this manner, we increased the number of highly energetic ions arriving at the trench bottom. The new comparison is displayed in figures 4.5 and 4.6. Indeed, a higher steady state potential was acquired (see figure 4.5). At this time, there is a quite successful coincidence between our results and those of the Hwang and Giapis. The slightly smaller potential at the lower part of the sidewalls may be justified by the utilization of a narrower IADF. A better agreement between the bottom IEDFs is also achieved (see figure 4.6).

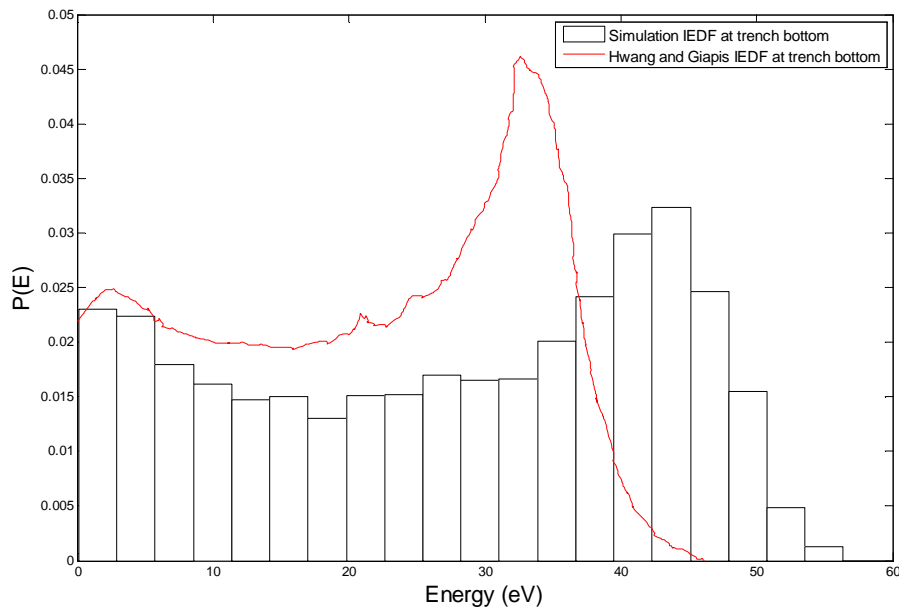


Figure 4.4: The energy distribution of ions arriving at the trench bottom. In our simulation, due to the lower steady state potential, the maximum is displaced to a higher energy.

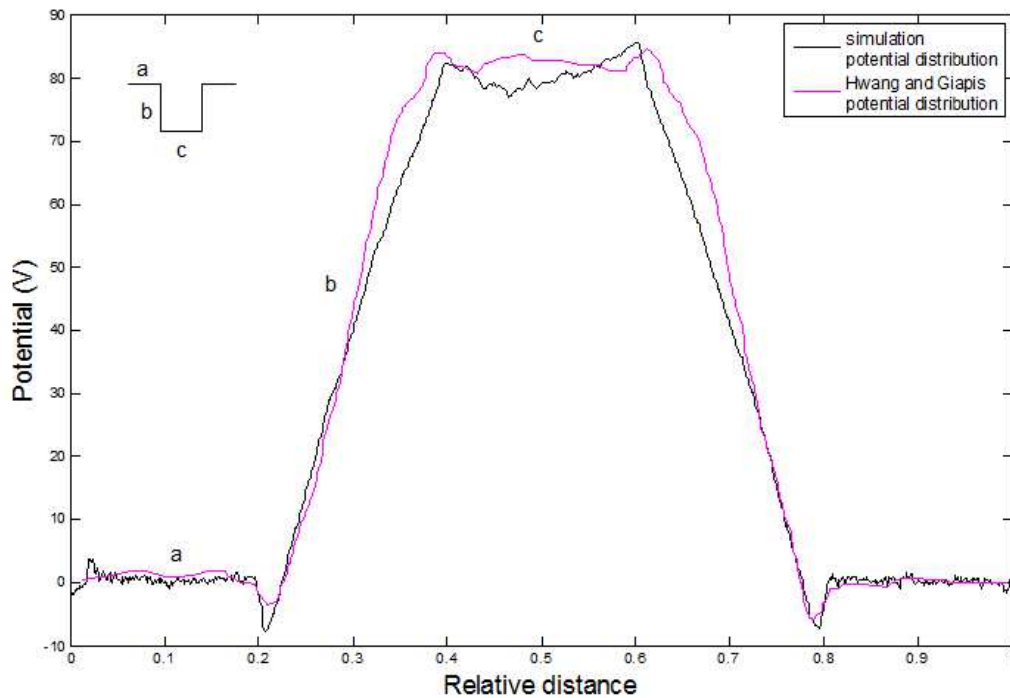


Figure 4.5: Charging potential distributions along the trench surface at AR (1.5:0.5). A narrow IADF has been used. The length scales have been normalized by the length of the top segment in order to facilitate comparisons. Inset at the left top: The top, sidewall, and bottom segments of the trench arclength are denoted by a, b, and c.

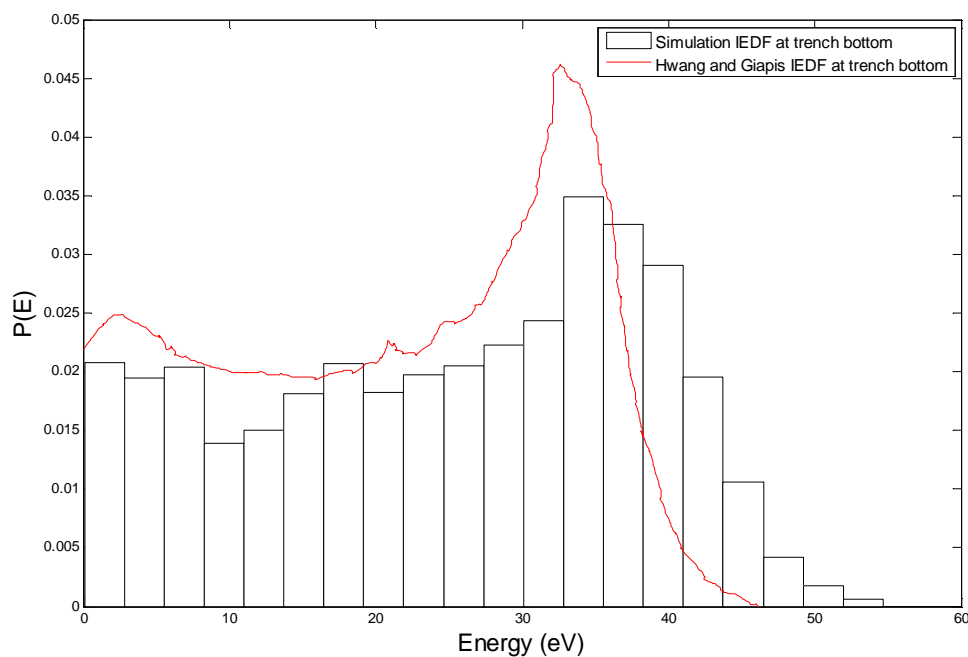


Figure 4.6: The energy distribution of ions arriving at the trench bottom. The utilization of a narrow IADF, leads to a better agreement.

4.3.2 Self-consistency check

4.3.2.1 Aspect ratio dependent charging

From dimensional analysis, the charging effect (as well as shadowing effect) is consistent with the scaling of etching rate with AR (AR dependent etching or ARDE rule) [22]. In order to check that the model is properly implemented we repeat the calculations for 2 trenches having the same AR but different widths. More precisely, we compare steady state results for a trench of depth $1.5\ \mu\text{m}$ and width $0.5\ \mu\text{m}$ with the case of a trench of depth $0.9\ \mu\text{m}$ and width $0.3\ \mu\text{m}$. The AR is constant and equal to 3 for both structures. In this way, the self-consistency of the model is examined. Specifically, from the below figures (4.7 and 4.8) it can be readily implied that the etching rate scales with AR.

As far as dielectric materials are concerned, a violation of the ARDE rule has been observed (AR independent etching-ARIE) [57]. Theoretical works have proposed different mechanisms that may lead to such an etching behaviour [15, 16]. Specifically, Hwang and Giapis [15] clarified that the ARDE rule breaks down for widths below $0.5\ \mu\text{m}$. In that work, when the evolving electric field surpassed a discharge threshold value E_s , currents were allowed to flow along the surface, thus reducing surface charging. However, with the increasing of the trench depth, surface currents, were not so effective in reducing the bottom potential. Indeed, for $W=1\ \mu\text{m}$ and $W=0.5\ \mu\text{m}$ it was proved that the ARDE still holds.

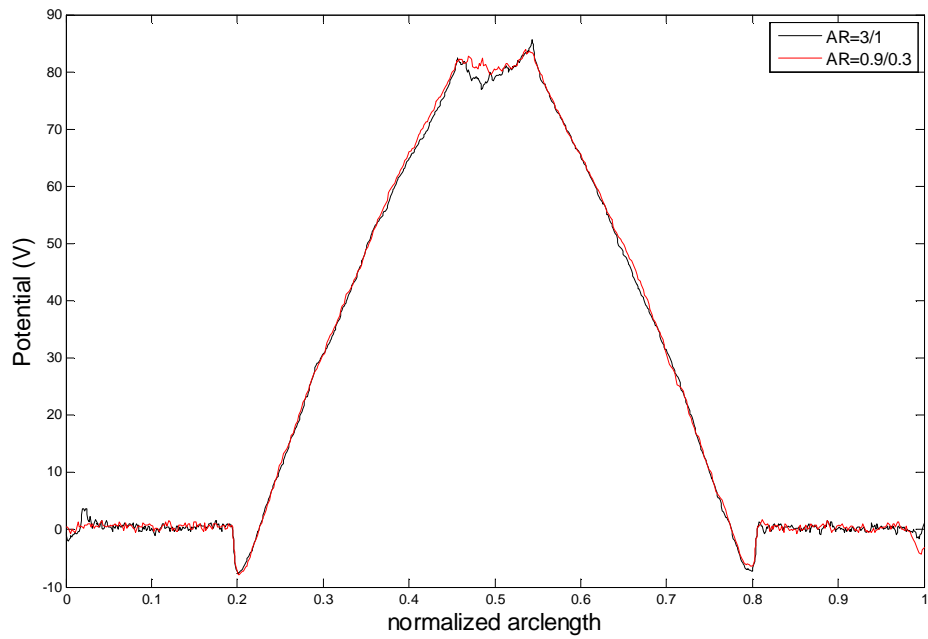


Figure 4.7: Charging potential distributions along the trench surface as a function of the trench width at constant AR that is equal to 3. Surface currents [15, 32] or sidewalls conductivity [16] are neglected. Obviously, ARDE holds.

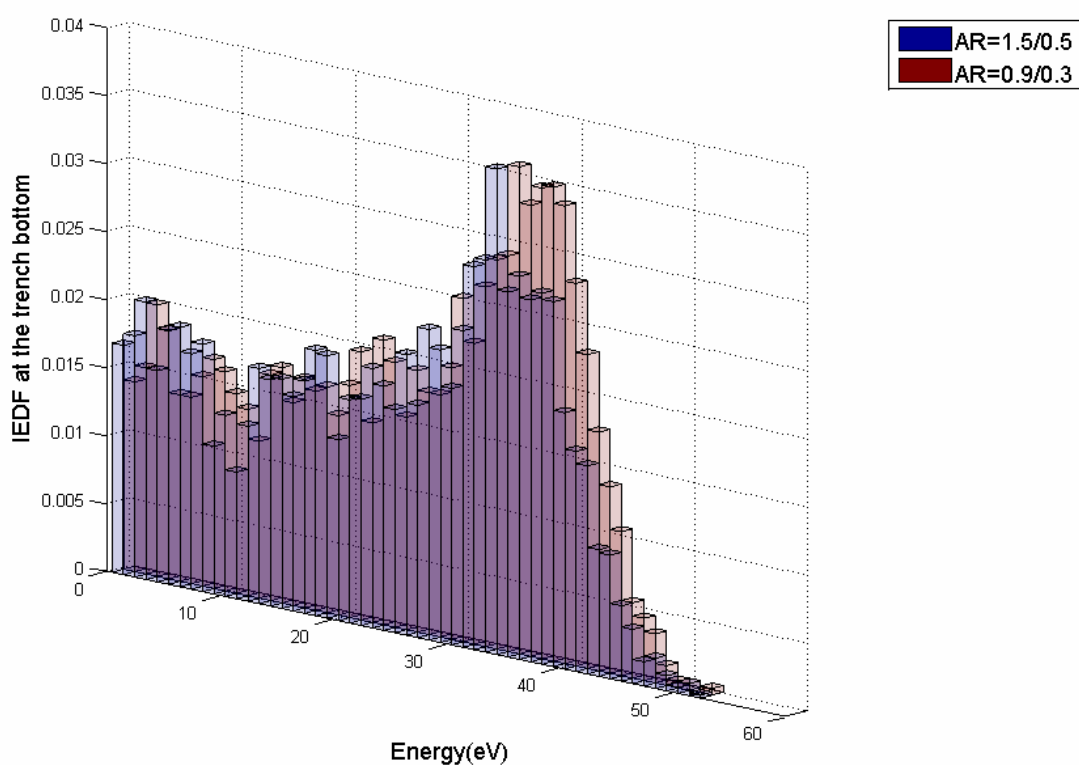


Figure 4.8: The energy distribution of ions arriving at the trench bottom as a function of the trench width (a) $0.5\mu\text{m}$ and (b) $0.3\mu\text{m}$ at constant AR (3). Apparently, etching rate does not change for microstructures of same AR, irrespective of the absolute feature size.

4.3.2.2 The effect of the simulation randomness on the results

Due to the fact that our model is a stochastic model the resulting, output values may vary depending on the stochastic variation of the input values. Since the variation of the input values is generated by random sampling from the given probability distributions, it is important to verify that the output values are not strongly affected by the simulation randomness.

In figure 4.9, the charging potential distribution along the trench surface for two different simulation runs conducted under the same conditions is presented. The only difference is the different seeds of the random numbers generation in each run. In figure 4.10, we compare the bottom IEDFs that ensue in each case. As it can be seen, the steady state condition is not significantly altered by the simulation randomness.

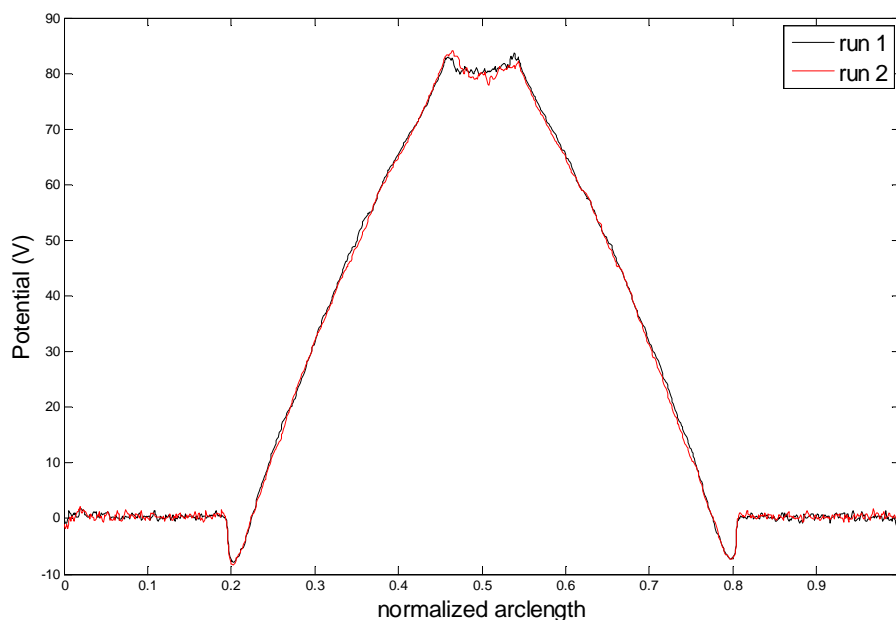


Figure 4.9: Charging potential distribution along the trench surface for two different runs conducted under the same conditions.

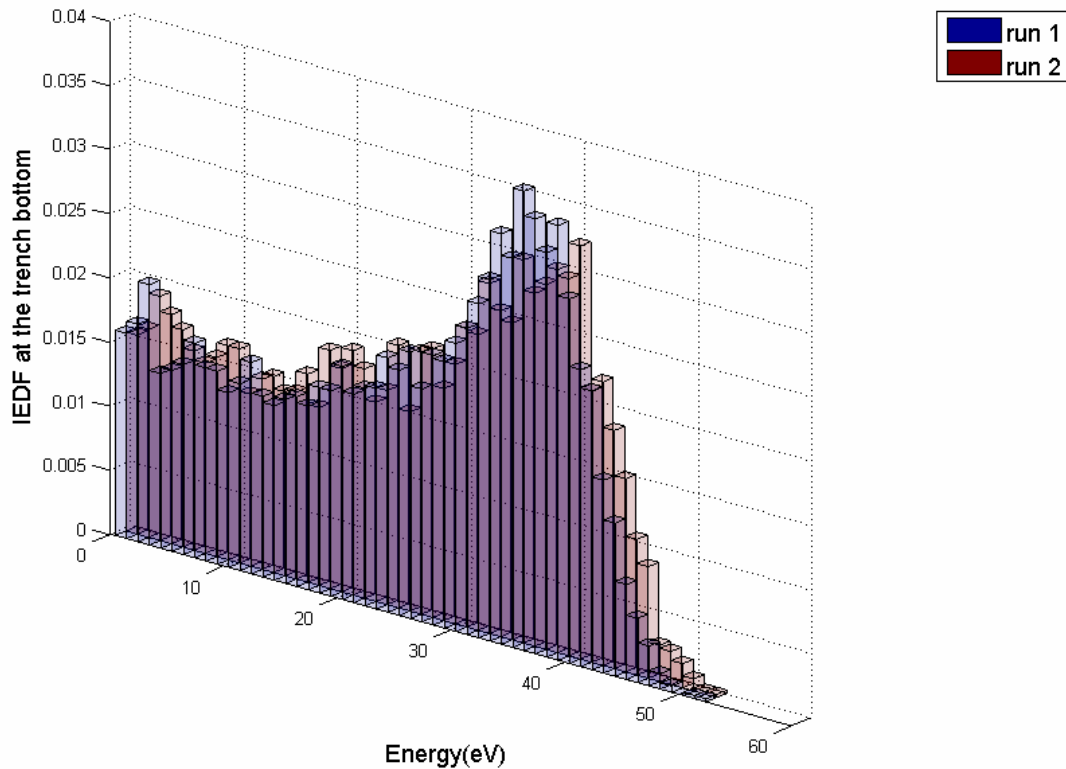


Figure 4.10: The energy distribution of ions arriving at the trench bottom for two different runs conducted under the same conditions.

4.3.3 The effect of the inlet position on the charging process

In this section, the influence of the inlet position on the charging process is investigated. For this purpose, the distance between the inlet and the dielectric boundary was gradually altered. Specifically, the distance suggested by the literature [12] is $2.2 \mu\text{m}$ (standard position, see figure 4.1). At this distance above the dielectric trench, the charging potential decays to zero [12, 19]. This distance was increased and subsequently decreased by $1.5 \mu\text{m}$. The particle distributions that were utilized during the conduction of the simulation have been described elsewhere (see section 3.2.2). In the following, the charging potential distribution along the dielectric surface as a function of the inlet position is demonstrated. There is a quit good coincidence among the results. Thus, it can be assumed that inlet position does not play an important role in the charging process.

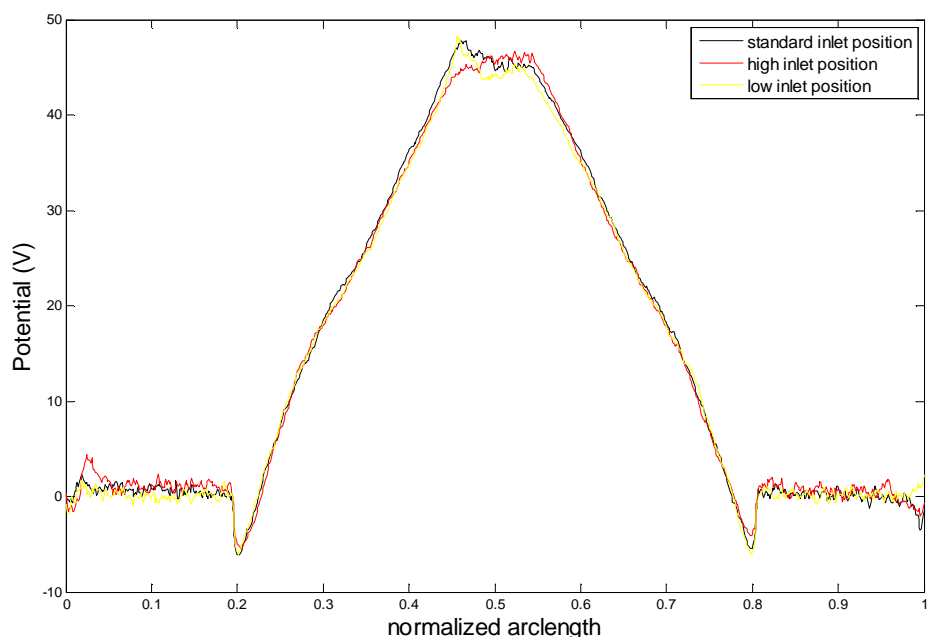


Figure 4.11: Charging potential distributions along the trench surface as a function of the inlet position.

4.4 The effect of the IEDF shape on microstructure charging

The effect of the IEDF shape on the charging process is investigated by utilizing wide, a moderate and a narrow bimodal as well as a monoenergetic IEDF (see figure 4.12). All of the aforementioned IEDFs have the same average ion energy which is 70eV. For this purpose, the impact of a wide, a moderate and a narrow bimodal IEDF on the steady state condition is compared.

Generally, at low pressure, the ion energy distribution at the wafer depends on the applied RF bias and RF frequency [12]. As the frequency increases, the width of the bimodal IEDF decreases [53]. As the RF bias increases, the IEDF is positively shifted to higher energies [38, 58]. To the best of our knowledge, literature provides analytical mathematical expressions [44, 53] which capture the IEDF shape behavior only for the low and high frequency regime respectively. For the intermediate frequency case, which is most applicable in plasma-processing technologies, the development of a sheath model is needed [12, 19, 38]. As the goal of this work is not to model the behaviour of the plasma and sheath regions, the IEDF shape was artificially modified by gradually reducing its width. For that purpose, the mathematical expression of reference [44] was utilized.

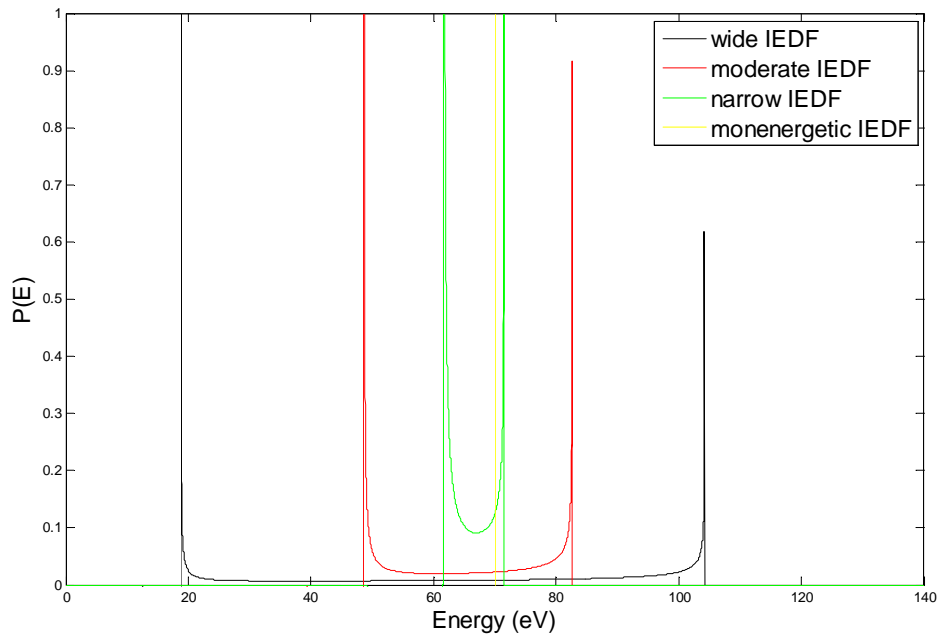


Figure 4.12: the four different energy distributions that are utilized in the charging process. Their common feature is the average ion energy which is equal to 70eV.

In figure 4.13, the ensuing steady state potential distributions along the trench surface as a function of the IEDF shape are demonstrated. The general conclusion of the results shown on figure 4.13 is that the average steady state potential increases as the width of the ion energy distribution is reduced. At the first place, the wide IEDF gives a maximum potential value of 60 eV. The same applies for the moderate IEDF but in that case there is a slight increase in the middle region of the sidewall potential. This indicates a larger number of energetic ions that are able to enter the trench. Indeed, for the wide IEDF, the probability for an ion to have energy larger or equal to 60 eV is 0.64.³⁴ On the other hand, in the case of the moderate IEDF, this probability value is 0.74.

³⁴ Integrate IEDF from 60eV to its last energy value.

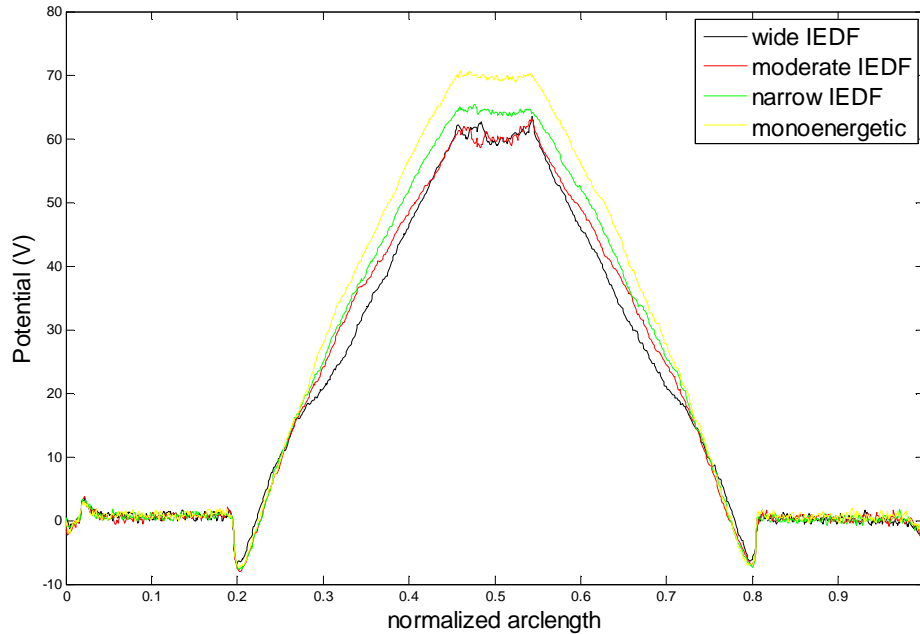


Figure 4.13: Charging potential distributions along the trench surface as a function of the IEDF shape.

As the two peaks of the IEDF approach each other, a larger potential value is acquired (~64V). Indeed, as the IEDF width is being reduced, more ions with energy above the average (70eV) enter the trench. Simultaneously, electron flux is still impeded by electron shadowing effect. Thus, in order to maintain current balance, the system must increase its potential.

The total ion flux is approximately the same in all cases as it is clearly presented in the figure 4.14. This is crucial for the system to maintain current balance. Indeed, as the electron flux is not altered significantly by the change in the IEDF shape (see figure 4.15), the total ion flux must be the same in all cases. For this reason the steady state potential is increased on the sidewalls (for instance, compare wide and moderate case in 4.12) and the trench bottom in order to repulse the larger amount of energetic ions that are able to enter the trench.

Interestingly enough, it seems that the total ion flux is not significantly affected by the shape of the IEDF as the controlling factor of the process is the invariable electron flux. On the contrary, as it is clearly depicted in figure 4.16, the ion energy distribution at the trench bottom is deeply influenced by the form of the ion energy distribution. As the initial IEDF width is reduced, the ions impinge the trench bottom with less energy.

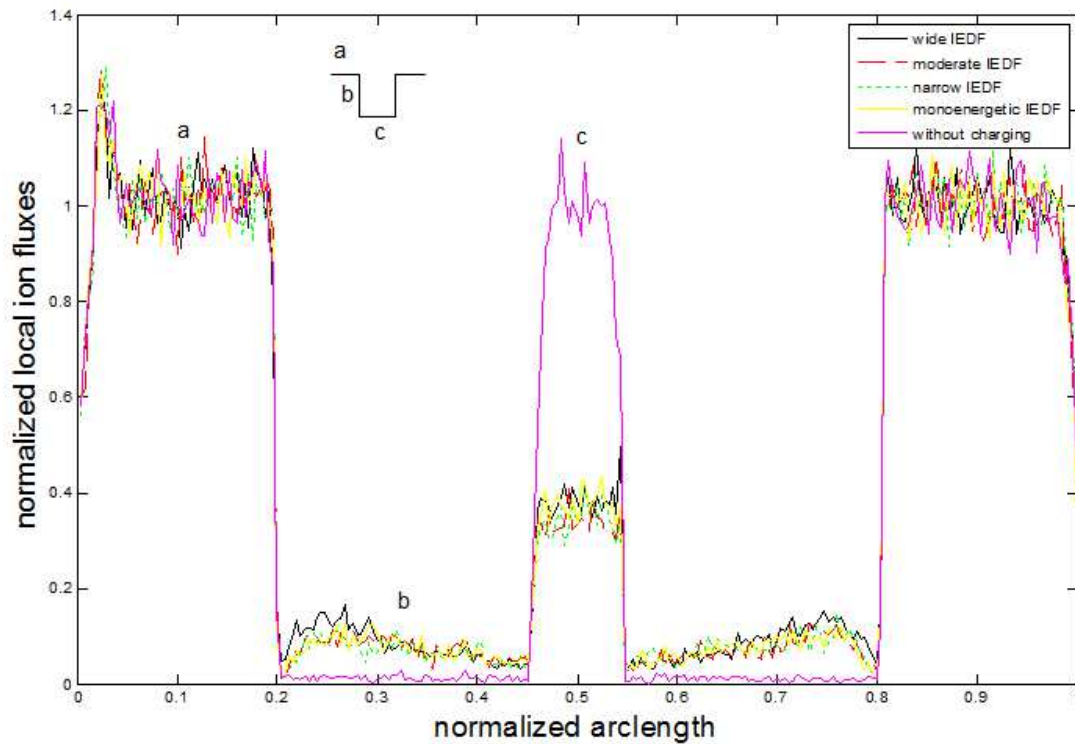


Figure 4.14: Normalized local ion fluxes along the trench surface as a function of IEDF shape. The flux in the case of no charging is also depicted. Charging has a severe impact on the ion flux. Namely, 60% of the ions that would reach trench bottom without charging, is repulsed either out of the trench or towards the sidewalls by the steady state potential. For that reason, ion flux is increased approximately by 10% to the sidewalls for all cases. Inset at the left top: the trench arclength. Inset at the left top: The top, sidewall, and bottom segments of the trench arclength are denoted by a, b, and c.

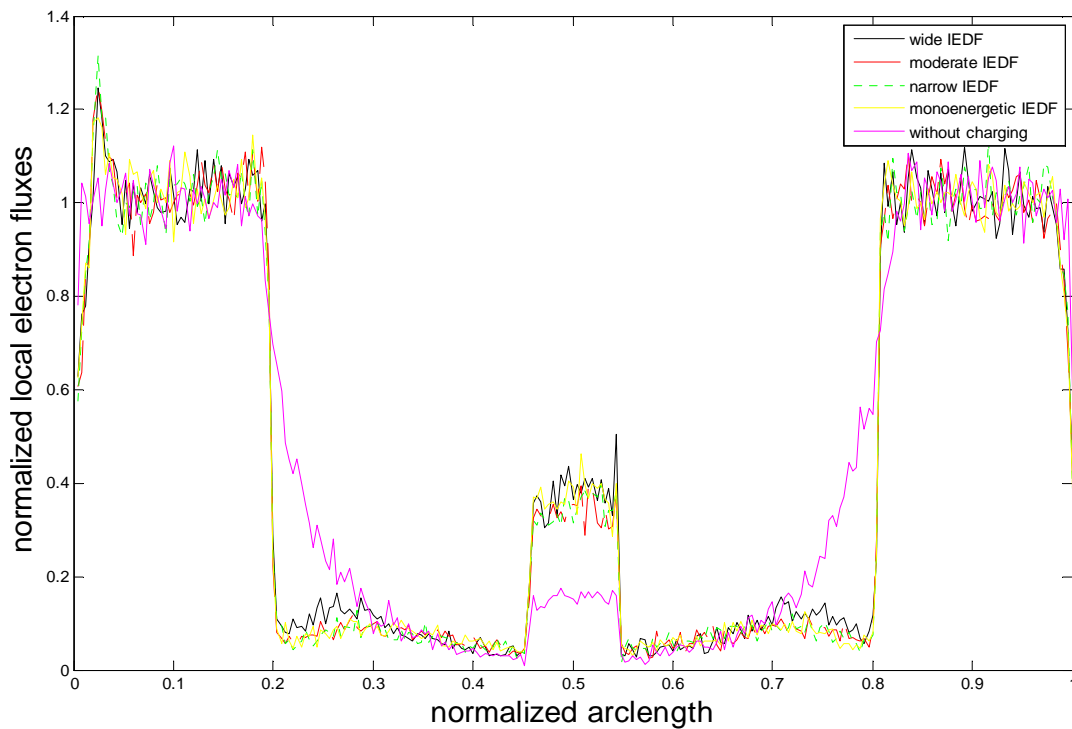


Figure 4.15: Normalized local electron fluxes along the trench surface as a function of IEDF shape. The no charging case flux is also depicted. Charging has a quite important impact on the electron flux. Electron shadowing seems to be restricted if a positive

potential exists. Indeed, the electron flux is increased at the trench bottom and simultaneously is reduced at the sidewalls due to attraction. However, the change in the IEDF shape seems to leave the electron flux unaffected.

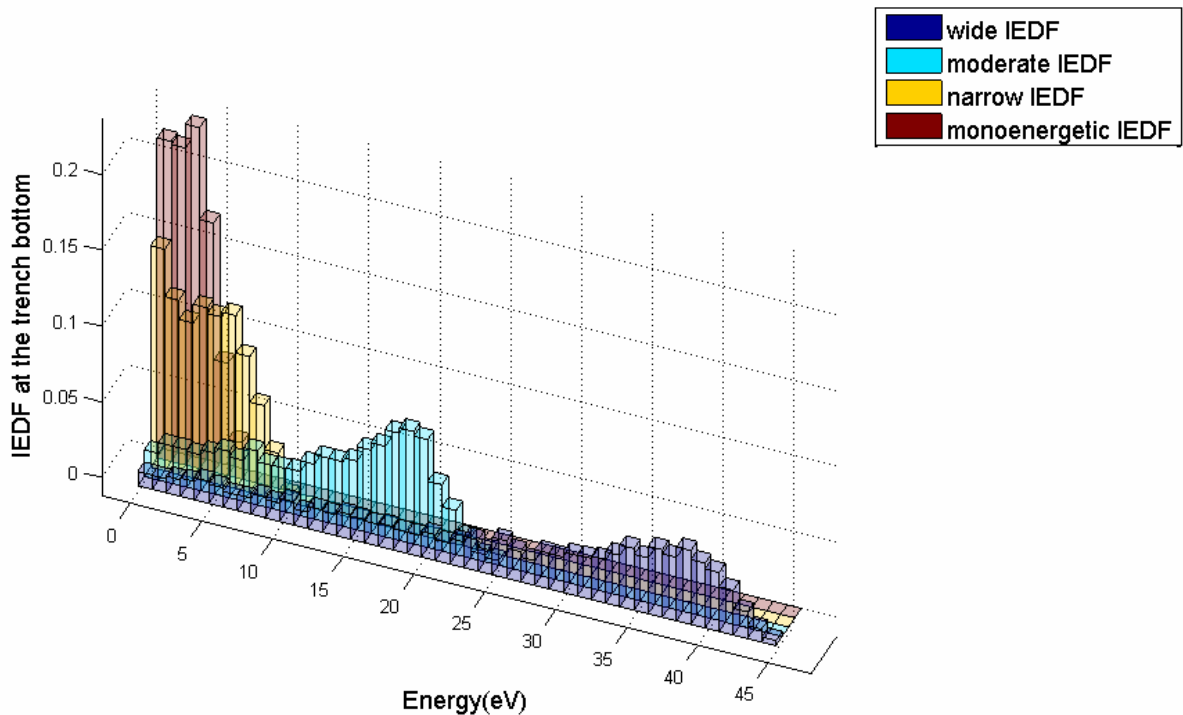


Figure 4.16: The energy distribution of ions arriving at the trench bottom as a function of the initial IEDF shape. The narrower the initial IEDF is, the less energetic the impinging ions at the trench bottom will be.

Figure 4.17 shows the normalized etching yield along the dielectric surface. For each IEDF shape, the etching yield at all positions is normalized by the maximum etching yield. The same applies for the etching rate, depicted on figure 4.18. The etching yield and the etching rate calculated without taking consideration the charging effect are also presented at the same diagrams. The purpose is to compare all cases and see how charging affects the etching of the dielectric structure.

As it was anticipated from figure 4.16, the etching rate is almost zero for the narrow and monoenergetic IEDF cases. Due to microstructure charging, it can be implied that an electrostatic etch stop occurs for that cases. Additionally, the fall of the etching rate for the other two cases in regard to the no charging etching rate cases is remarkable.

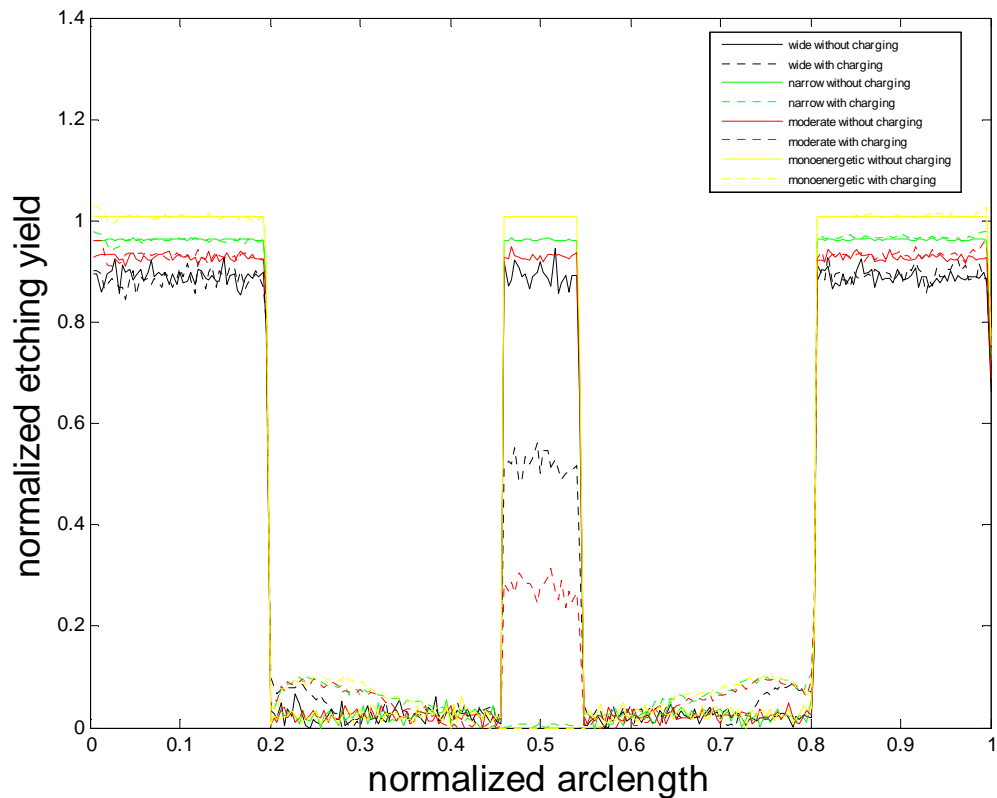


Figure 4.17: Normalized etching yield along the surface of structure as a function of the IEDF shape. The respective no charging cases are also depicted.

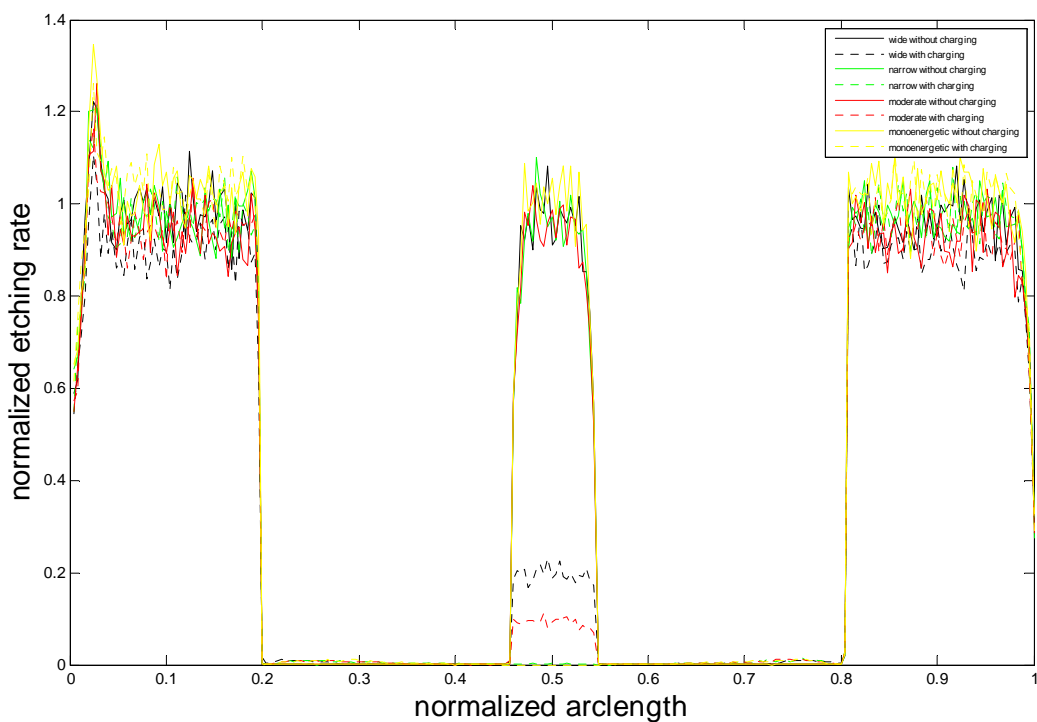


Figure 4.18: Normalized etching rate along the surface of structure as a function of the IEDF shape. The respective no charging cases are also depicted.

4.5 The effect of the average ion energy on the microstructure charging

In this section, the influence of the ion average energy on the microstructure charging is investigated. It has been experimentally verified [58] that in the case of an Ar plasma, the bimodal IEDF is quite extensive at a frequency of 13.56 MHz, a working pressure of 10 mtorr and at high discharge power. For that reason, the wide IEDF from the previous section was chosen for the calculations. With the purpose to examine the consequences of a larger average ion energy, the IEDF is gradually displaced towards higher energies. The increase of the RF amplitude voltage at the electrode can lead to such a positive shift [38]. The IEDFs used are shown in figure 4.19.

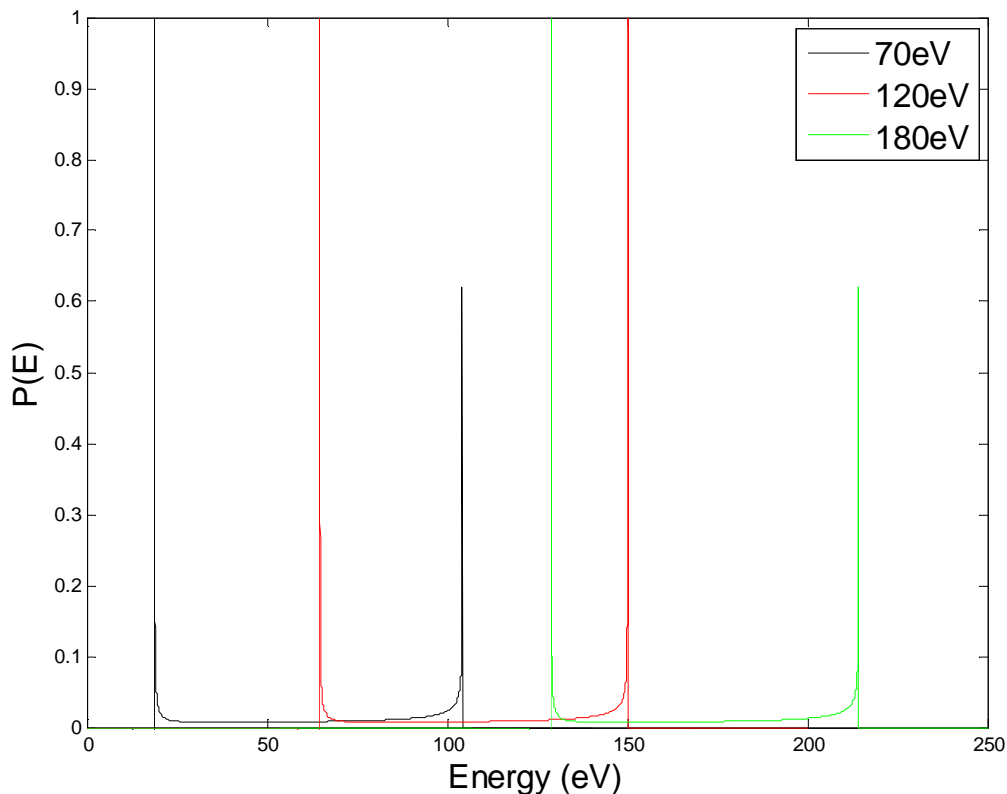


Figure 4.19: the three different energy distributions that are utilized in the charging process. The average ion energy is gradually increased (70eV,120eV,180eV).

In figure 4.20, the ensuing average steady state potential distributions along the trench surface as a function of the ion average energy are demonstrated. The general conclusion is that a larger ion average energy value involve a larger steady state potential. Indeed, a more energetic ion flux, will charge up the surface more positively. This can be easily understood if we assume no electron flux. In that case, for instance, a monoenergetic ion flux of 100 eV will lead to the formation of a 100 V steady state potential. This because owing to the absence of electron flux, the ion flux must be zero at the steady state. This is required for maintaining current balance principle. Similarly, a more energetic ion flux will involve the development of a larger steady state potential.

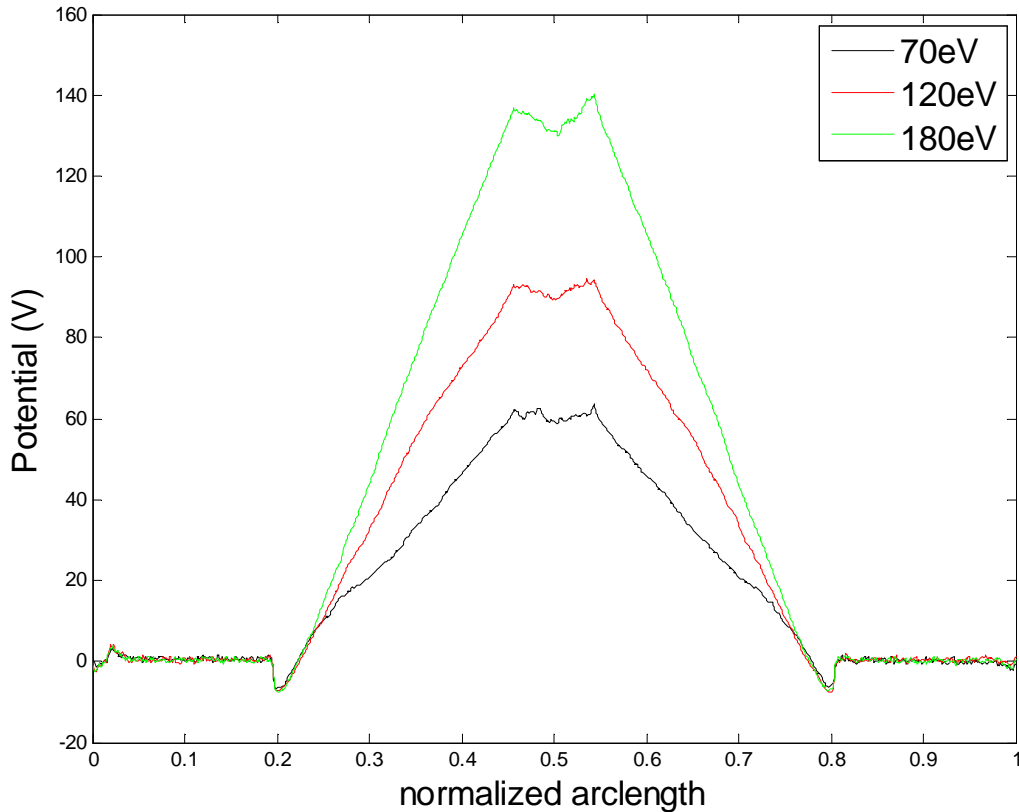


Figure 4.20: Charging potential distributions along the trench surface as a function of the ion average energy.

On the other hand, in the case of a simultaneous electron and ion flux, electrons will be attracted in order to compensate the initial current imbalance (due to electron shadowing). Provided that the initial current imbalance is overwhelming (see ion and electron flux without charging in figures 4.21 and 4.22 respectively) and a more energetic ion flux impinge gradually on the dielectric bottom surface, the potential is continually increasing until enough ions are deflected away to make current balance attainable. The figure 4.20 describes this process.

The total ion flux increases as the ion average energy rises. The same applies for the electron flux. The results are depicted in the figures 4.21 and 4.22. The system behavior can be comprehended in a more convenient way by demonstrating the evolution of ion and electron fluxes at the trench bottom during the whole charging process (figure 4.23). As the ion average energy increases, the ion flux decreases much more slower at the first stage (1-50 steps) of the charging process. Indeed, having larger energy, the number of ions that reach trench bottom is reduced at a slower pace by the developing potential. Concurrently, electron flux takes advantage of this fact by increasing rapidly due to the reinforcing attraction. When finally the ensuing potential establish current balance, the fluxes are stabilized. It is evident that

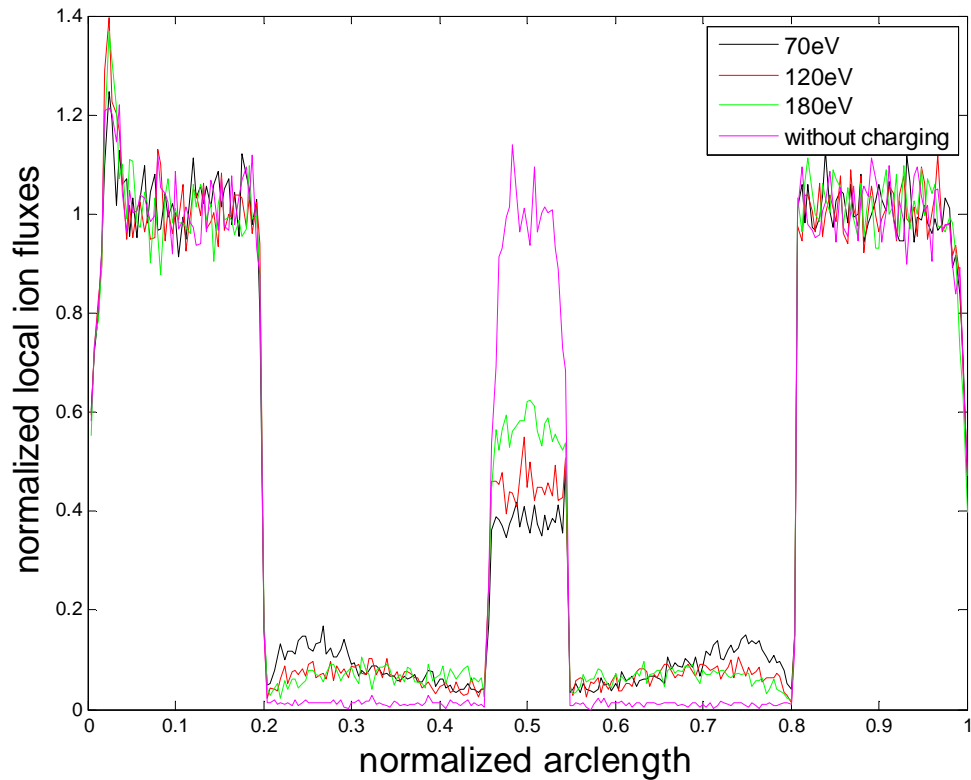


Figure 4.21: Normalized local ion fluxes along the trench surface as a function of the ion average energy. The flux in the case of no charging is also depicted. As the energy grows, the total ion flux augments. The system's delay to stabilize ion and electron fluxes is responsible for this fact.

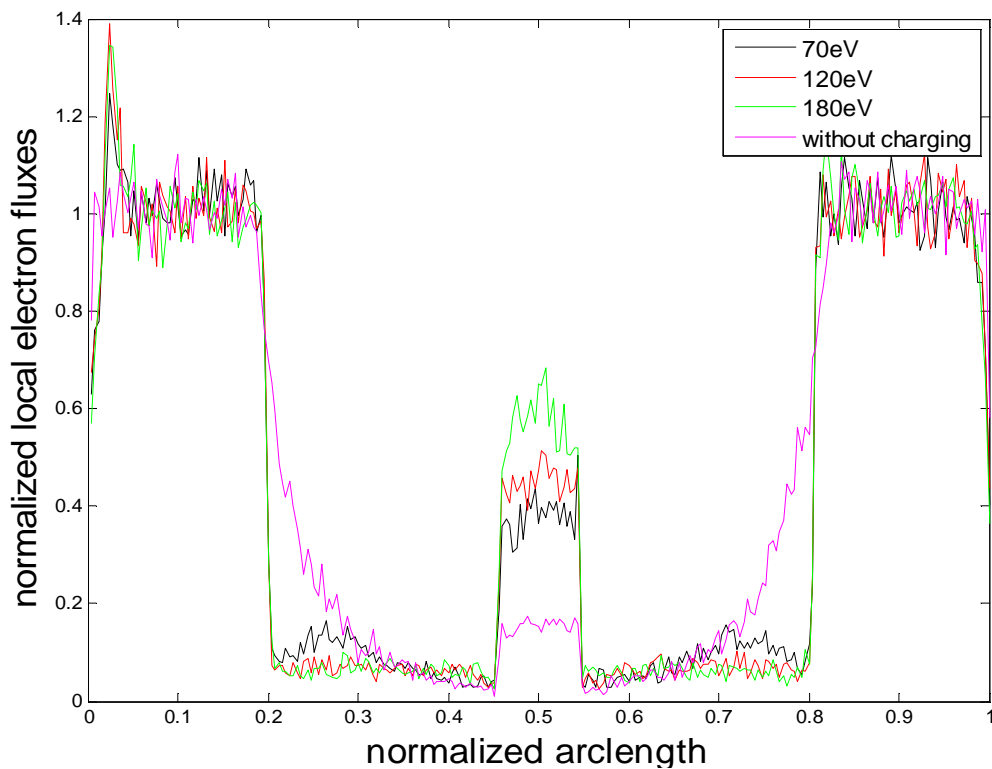


Figure 4.22: Normalized local electron fluxes along the trench surface as a function of ion average energy. The flux in the case of no charging is also depicted. As the energy grows, the total electron flux augments. The system's delay to stabilize ion and electron fluxes is responsible for this fact.

the more energetic are the ions, the more time is needed for the evolving potential to counterbalance the process. The consequence of such a delay is the establishment of larger equal ion and electron fluxes at the steady state regime something that lead ultimately to larger total fluxes.

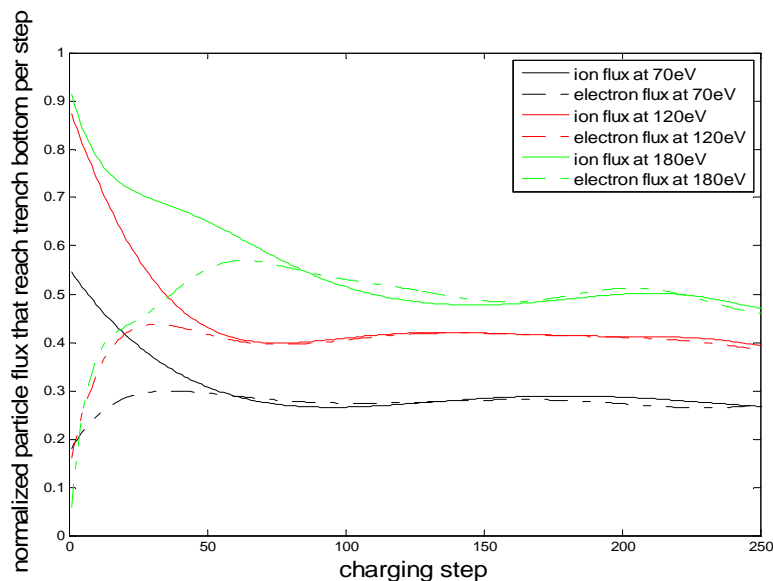


Figure 4.23: The evolution of the normalized ion and electron fluxes to the bottom SiO₂ surface of the trench during the charging process. During steady state, the fluctuations in the fluxes are a result of the stochastic nature of the process. The average steady-state charging potentials are insensitive to such small fluctuations.

Unsurprisingly, as the ion average energy is increased, the ions impinge the trench bottom with more energy. More precisely, due to electrostatic repulsion, the ions are decelerating as they enter the trench. The more energy they have at the inlet of the trench, the more energetic they will be when they impinge on the dielectric surface. This is clearly illustrated in figure 4.24.

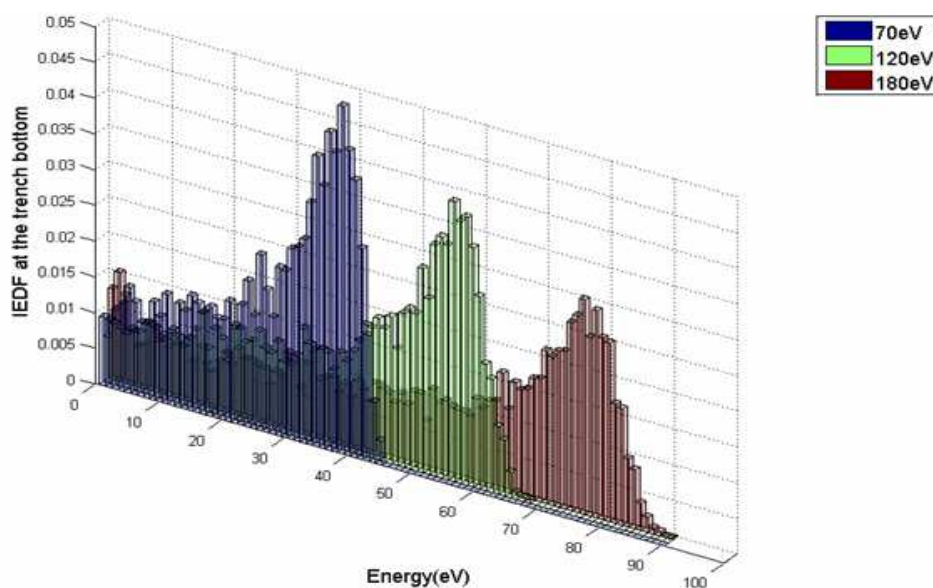


Figure 4.24: The energy distribution of ions arriving at the trench bottom as a function of the ion average energy. The smaller the ion average energy is, the less energetic the impinging ions at the trench bottom will be.

Figure 4.25 shows the normalized etching yield along the dielectric surface. For each IEDF shape, the etching yield at all positions is normalized by the maximum etching yield. The same applies for the etching rate, depicted on figure 4.26. The etching yield and the etching rate calculated without taking consideration the charging effect are also presented at the same diagrams. The purpose is to compare all cases and see how charging affects the etching of the dielectric structure.

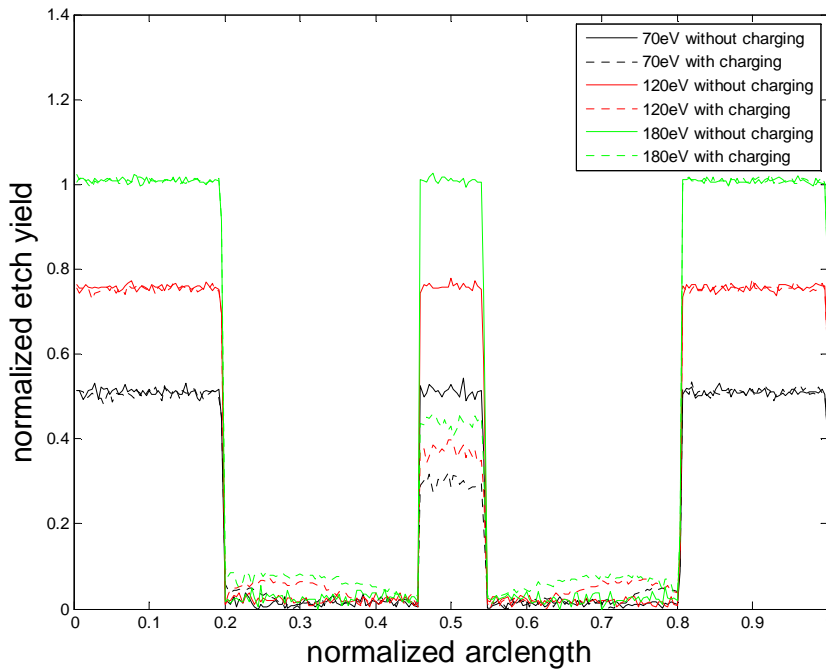


Figure 4.25: Normalized etching yield along the surface of the structure as a function of the ions average energy . The no charging respective cases are also depicted.

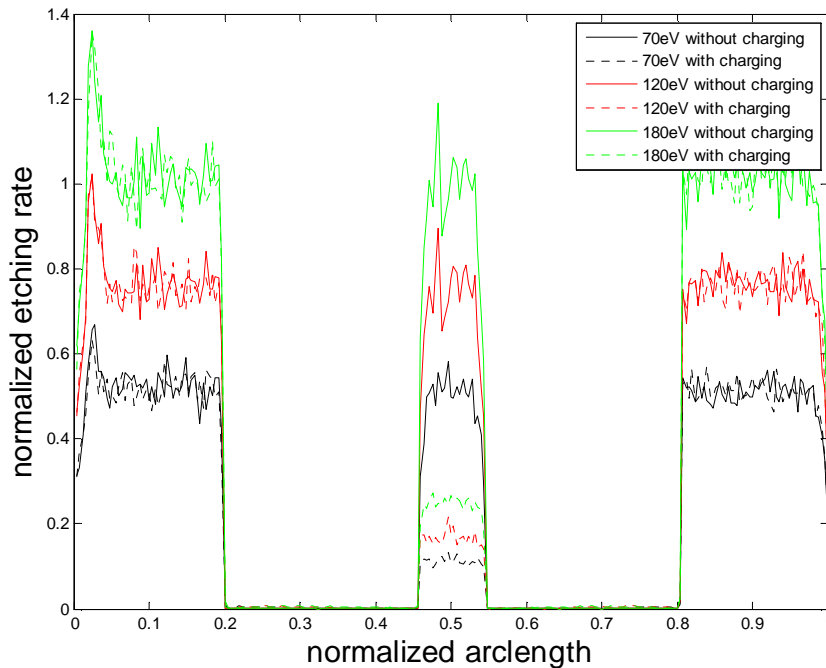


Figure 4.26: Normalized etching rate along the surface of structure as a function of the IEDF shape. The no charging respective cases are also depicted.

The etching rate is remarkably decreased for all average ion energies compared to cases with no charging. Besides, it should be mentioned that, in any case, sidewall etching rate is negligible.

4.6 The effect of the electron temperature on microstructure charging

The effect of the electron temperature on the charge-up potential distribution at the trench surface is investigated. For this purpose, the electron temperature is subsequently modified for the charging process. The electron energy distributions used are depicted in figure 4.27. Regarding the IEDF, the IEDF from the previous section with an average energy equal to 180 eV was used.

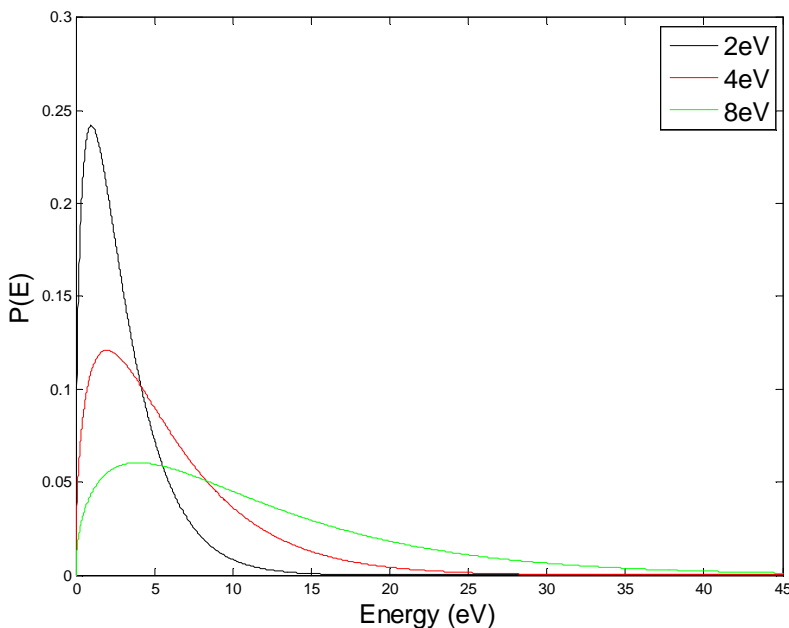


Figure 4.27: The corresponding electron energy distribution function (EEDF) for various electron temperatures, as indicated.

The average steady state potential is affected by the electron temperature. In particular, as it can be seen in figure 4.28, a higher steady state potential is generated as electron temperature increases. Note the gradual fall at the upper part of the trench sidewall potential. The ensuing larger negative entrance potential aggravates the electron shadowing problem.

Due to the higher electron temperature, more energetic electrons impinge on the microstructure. Due to the higher energy electrons, a more negative potential will rise at the upper sidewalls in order for the current balance to be restored at these regions. Consequently, the entrance potential becomes more negative,

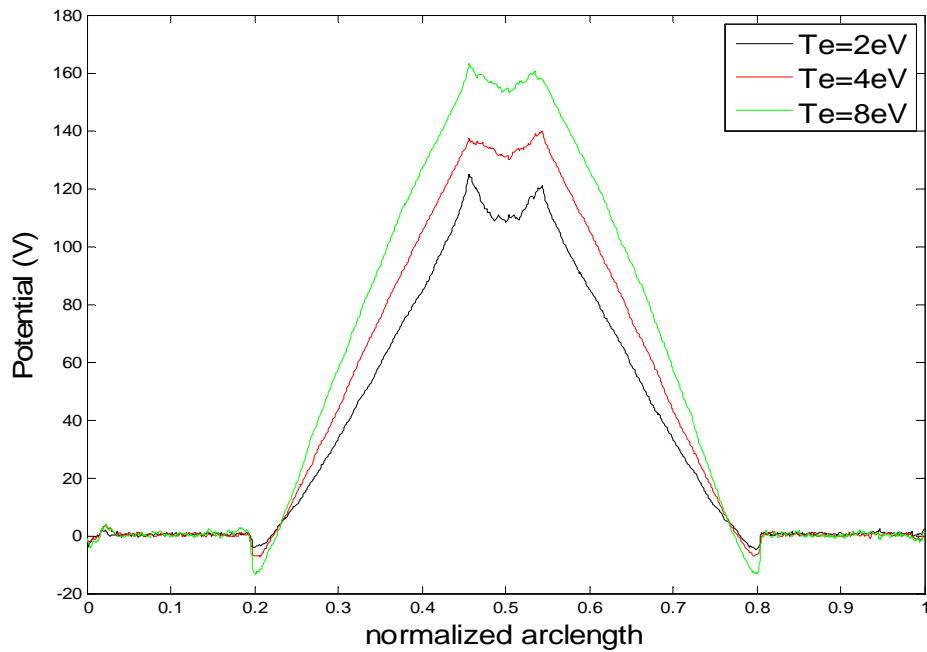


Figure 4.28: Charging potential distributions along the trench surface as a function of the electron temperature.

thus more electrons are prevented from entering the trench. Due to this fact, the current balance is achieved for a lower electron flux (see figure 4.29), so the potential increases until enough ions are deflected away to make current equalization attainable (figure 4.28).

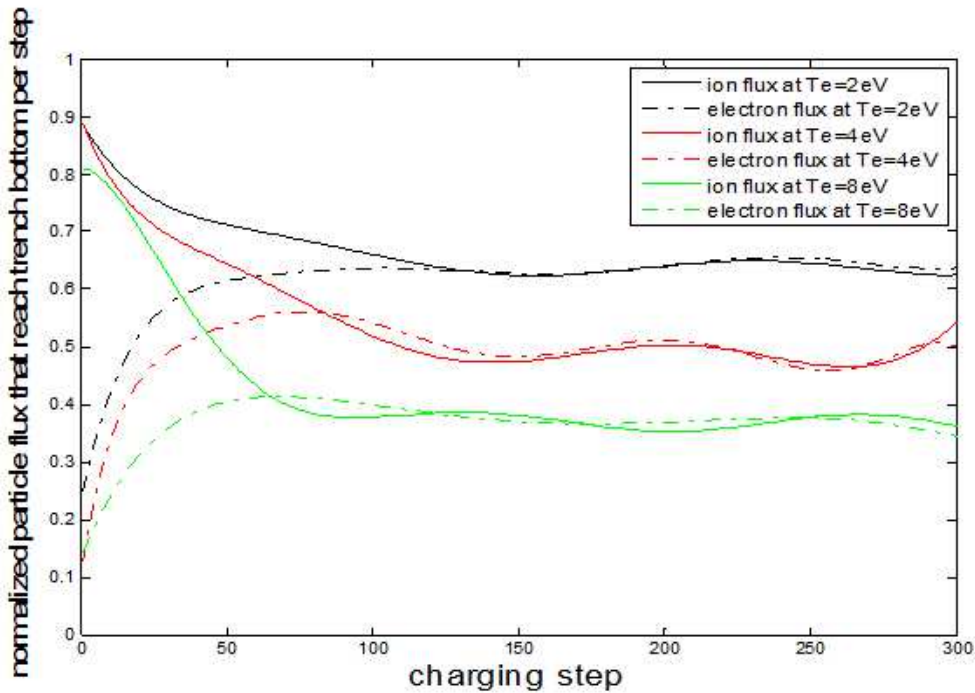


Figure 4.29: The evolution of the normalized ion and electron fluxes to the bottom SiO₂ surface of the trench during the charging process. During steady state, the fluctuations in the fluxes are a result of the stochastic nature of the process. The average steady-state charging potentials are insensitive to such small fluctuations.

The total steady state ion flux decreases as the electron temperature rises. The same applies for the electron flux. The results are depicted in the figures 4.30 and 4.31. The system behavior can be comprehended in a more convenient way by focusing on the evolution of ion and electron fluxes at the trench bottom during the whole charging process (figure 4.29). As the electron temperature increases, the ion flux decreases much more faster at the first stage (1-50 steps) of the charging process. Simultaneously, electron flux increases at a slower pace due to heavy electron shadowing. Indeed, the enhancement of electron shadowing establishes a more negative potential at the trench entrance something that impedes electrons to enter the trench. When finally the ensuing potential settles current balance, the fluxes are stabilized. It is evident that the more energetic are the electrons, the smaller their flux at the trench bottom will be. On the other hand, the potential must increase to counterbalance the fluxes. Conclusively, the effect of the potential decrease at the trench entry involves smaller ion and electron fluxes at the steady state regime and, in turn, smaller total fluxes.

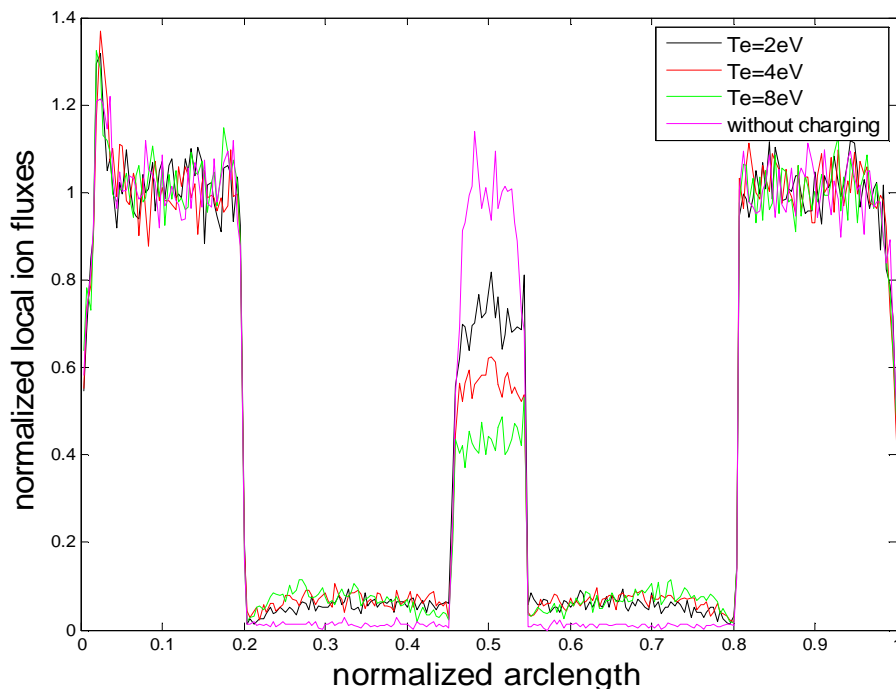


Figure 4.30: Normalized local ion fluxes along the trench surface as a function of the electron temperature. The flux in the case of no charging is also depicted. As the electron temperature grows, the total ion flux decreases. The electron flux decline due to the enlargement of the negative entrance potential is responsible for this fact.

Unsurprisingly, as the electron temperature is increased, the ions impinge the trench bottom with less energy. More precisely, due to the electrostatic repulsion, the ions are decelerating as they enter the trench. The larger the positive potential at the trench bottom is, the less energetic they will be when they impinge on it. This is clearly illustrated in figure 4.32.

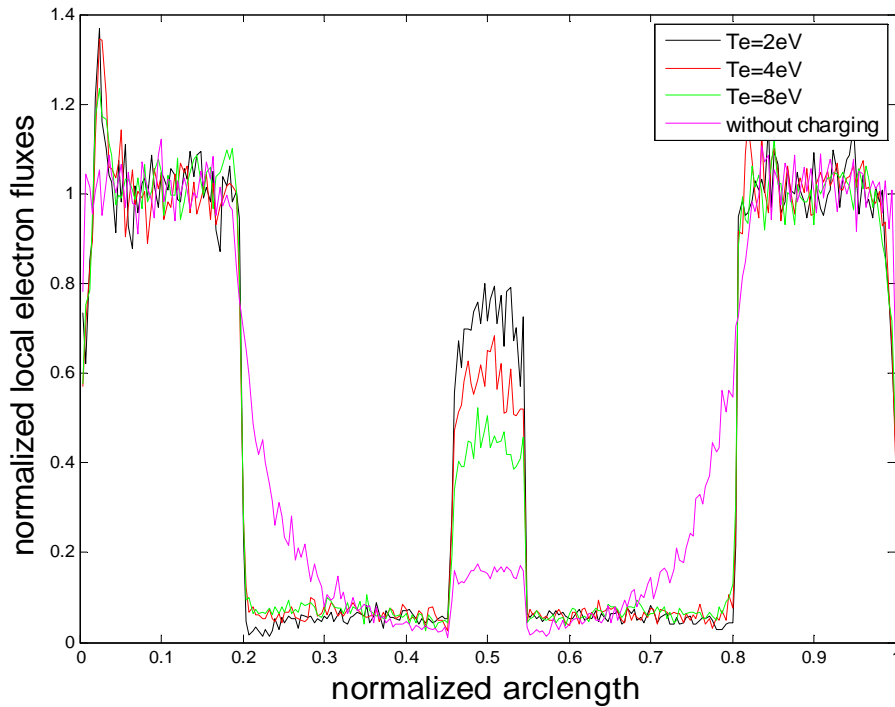


Figure 4.31: As the electron temperature grows, the total electron flux lessens. The more energetic electrons enhance electron shadowing effect.

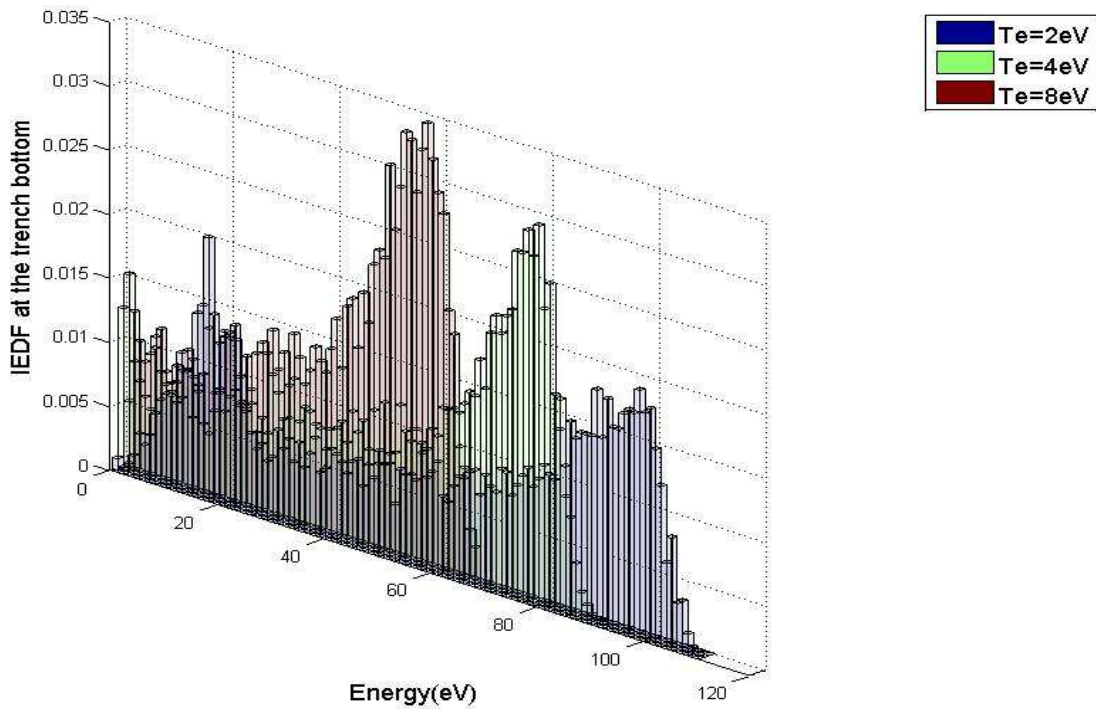


Figure 4.32: The energy distribution of ions arriving at the trench bottom as a function of the electron temperature. The larger the electron temperature is, the less energetic the impinging ions at the trench bottom will be.

In the following, figure 4.33 shows the normalized etching yield along the dielectric surface. For each electron temperature, the etching yield at all positions is normalized by the maximum etching yield. The same applies for the etching rate, depicted on figure 4.34. The etching yield and the etching

rate calculated without taking consideration the charging effect are also presented at the same diagrams. The purpose is to compare all cases and see how charging affects the etching of the dielectric structure.

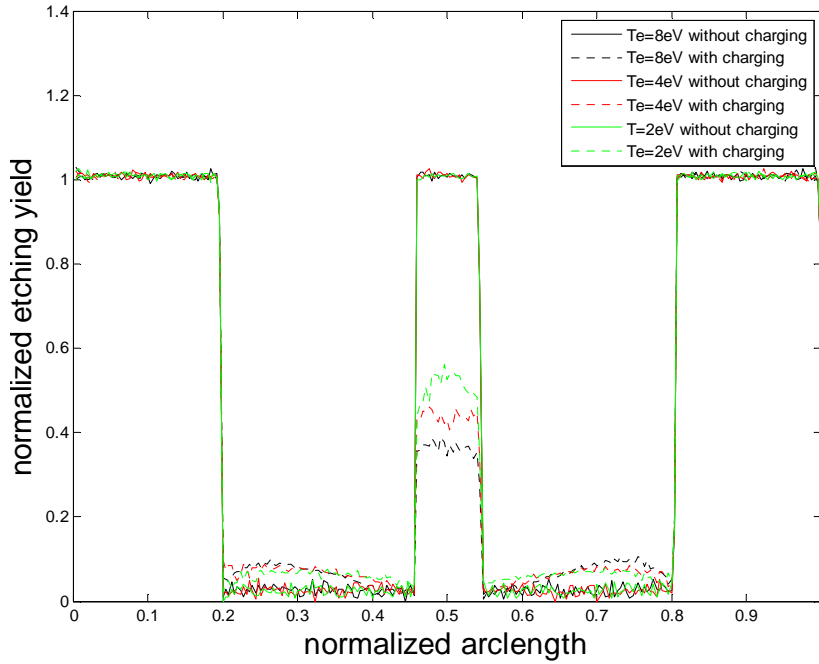


Figure 4.33: Normalized etching yield along the surface of structure as a function of the electron temperature. The respective no charging cases are also depicted.

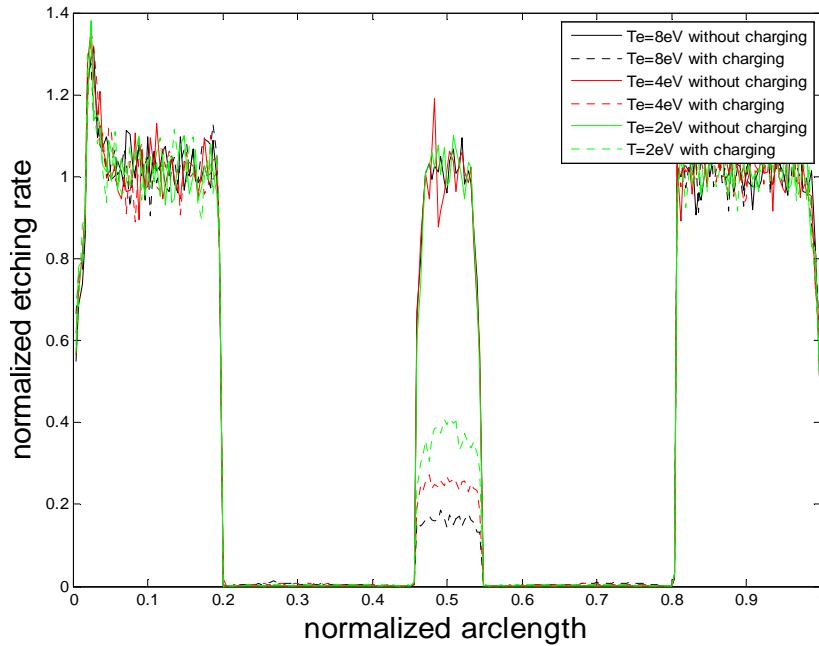


Figure 4.34: Normalized etching rate along the surface of structure as a function of the electron temperature. The respective no charging cases are also depicted.

The etching rate for the $T_e=2\text{eV}$ case is the highest of all three cases. Simultaneously, in any case, sidewall etching rate is negligible. The microstructure charging effect is most profound for 8eV electron temperature case as in that case the maximum trench bottom potential ensues.

4.7 The effect of the aspect ratio on microstructure charging

The effect of the AR on the charging potential distribution at the trench surface is investigated. For this purpose, the AR of the trench is subsequently modified for the charging process. Specifically, by gradually reducing the depth of the trench and concurrently holding the width constant and equal to $0.5\ \mu\text{m}$, the potential distribution along the trench surface is examined. The ensuing ARs are 1, 3 and 5. The IEDF with average ion energy $180\ \text{eV}$ from the previous section is utilized. The electron temperature is assumed to be $4\ \text{eV}$.

The average steady state potential is varied accordingly to the AR. Precisely, as it can be seen in figure 4.35, a higher steady state potential is generated as AR increases.

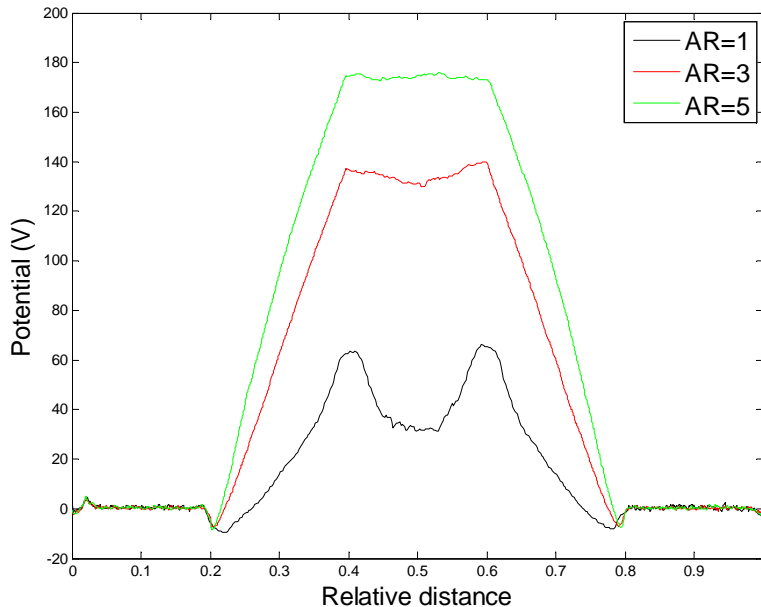


Figure 4.35: Charging potential distributions along the trench surface as a function of the trench AR. The length scales have been normalized by the length of the top segment of AR=3 case in order to facilitate comparisons.

Interesting appears to be the fact that the potential distribution profile at the trench bottom is also different. For AR equal to 1 and 3, the potential of the bottom central region is lower than that of the bottom's edge region. The potential difference is more profound for the AR=1 case. Due to light geometry shadowing, a larger electron flux impinges at the centre of the trench bottom than at the edges in the first case. Thus, in order for current balance to be restored at the edges, a higher potential is needed. As the AR increases, electron shadowing becomes more severe and the vast majority of electrons that reach trench bottom is due to electrostatic attraction. Thus, their flux is much more homogeneous and a smooth profile ensues. In any case however, the larger the AR is, the larger the steady state potential will be.

A larger AR means that the negatively charged upper sidewalls are in a larger distance from the positively charged dielectric bottom surface. This involves a

more negative entrance potential (see figure 4.36) something that in turn leads to a larger number of repelled electrons. Simultaneously, the longer sidewalls depletes further the electron flux to the trench bottom (note the electron flux without charging at the trench bottom in figures 4.38- 4.40).

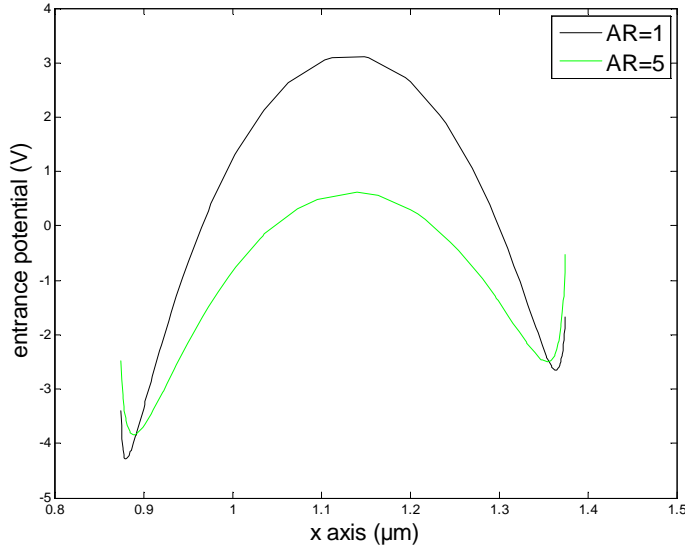


Figure 4.36: The potential distribution along the line connecting the top corners of the sidewalls. The trench width is $0.5\mu\text{m}$ in all cases. It starts at $0.875\mu\text{m}$ and ends at $1.375\mu\text{m}$.

Due to this fact, the current balance is achieved for a lower electron flux (see figure 4.37), thus the potential increases until enough ions are deflected away to make current equalization attainable (figure 4.35).

The total steady state ion flux decreases as the AR rises. The same applies for the electron flux. The results are depicted in the figures 4.38 to 4.40. The system's behavior can be comprehended in a more convenient way by focusing on the evolution of ion and electron fluxes at the trench bottom during the whole charging process (figure 4.37). As the AR increases, the ion flux decreases much more faster at the first stage (1-50 steps) of the charging process. Simultaneously, electron flux increases at a slower pace due to heavy electron shadowing. Indeed, a more negative potential at the trench entrance in combination with longer sidewalls further impede electrons to enter the trench. When finally the ensuing potential settles current balance, the fluxes are stabilized. It is evident that the larger the AR is, the smaller the electron flux at the trench bottom will be. On the other hand, the potential must increase to counterbalance the fluxes (this can be implicitly seen by the rapid decrease in the ion flux). Conclusively, the effect of the potential decrease at the trench entry involves smaller ion and electron fluxes at the steady state regime and, in turn, smaller total fluxes.

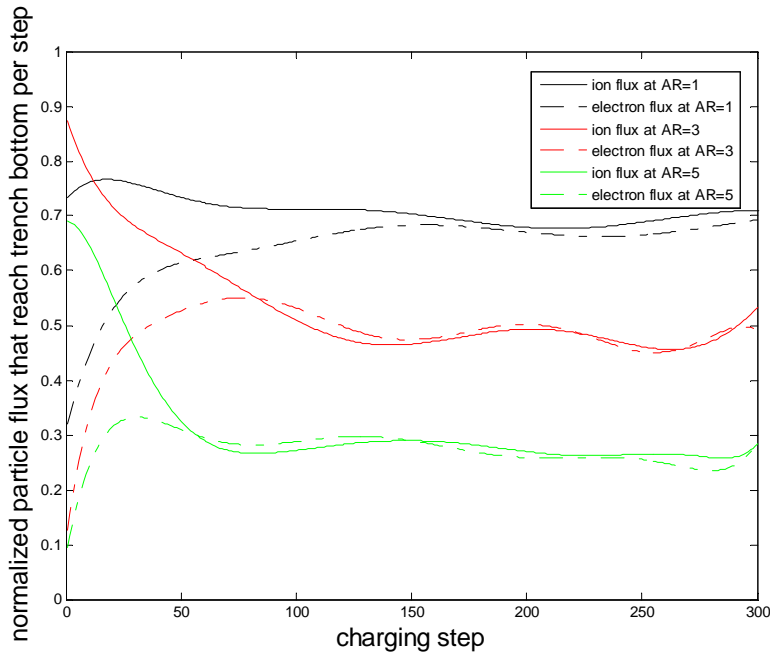


Figure 4.37: The evolution of the normalized ion and electron fluxes to the bottom SiO₂ surface of the trench during the charging process. During steady state, the fluctuations in the fluxes are a result of the stochastic nature of the process. The average steady-state charging potentials are insensitive to such small fluctuations.

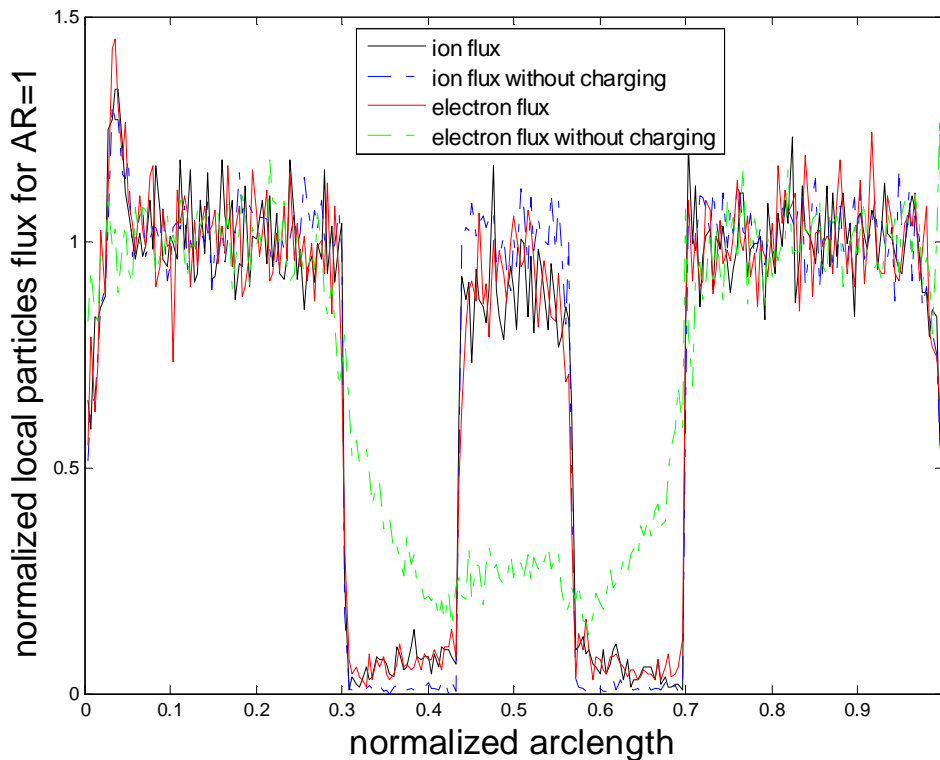


Figure 4.38: Normalized local ion and electron fluxes along the trench surface for the AR=1 case. The fluxes in the case of no charging is also depicted.

Note how electron shadowing affects ion and electron flux in all cases. The heavier is the geometric shadowing (cases without charging), the lower the total steady state fluxes at the trench bottom will be.

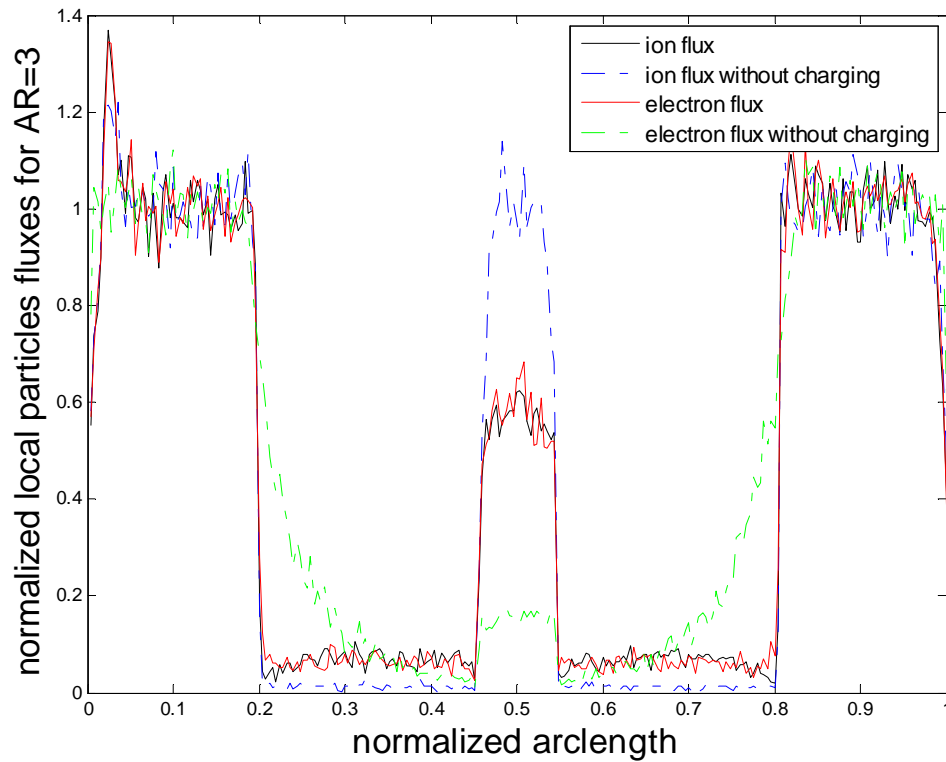


Figure 4.39: Normalized local ion and electron fluxes along the trench surface for the case of AR=3. The fluxes in the case of no charging is also depicted.

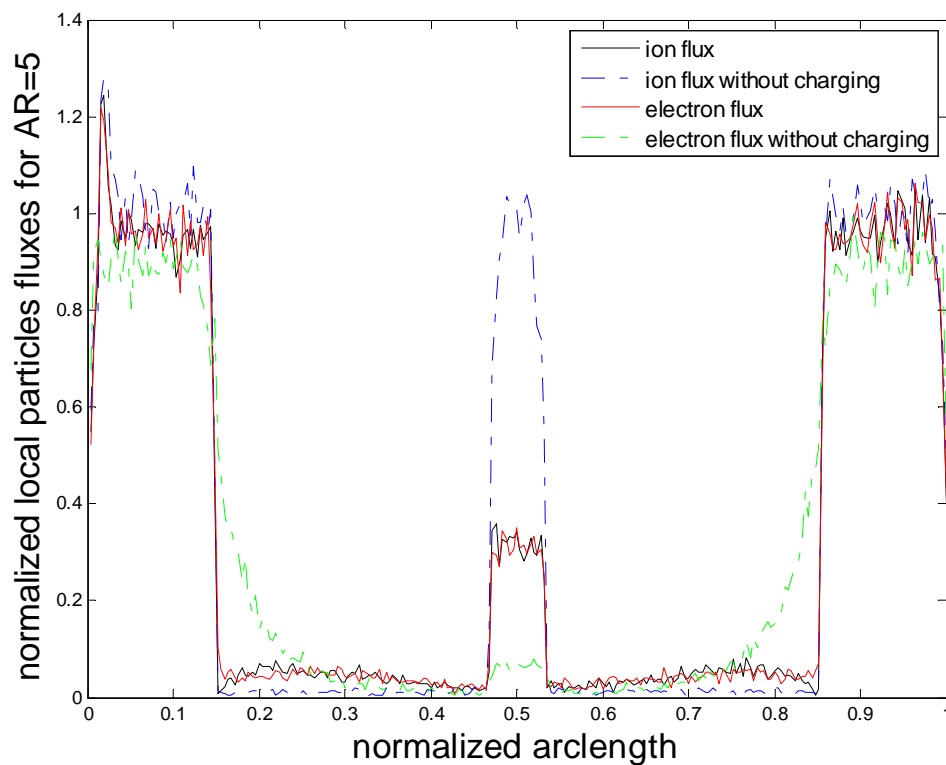


Figure 4.40: Normalized local ion and electron fluxes along the trench surface for the case of AR=5. The fluxes in the case of no charging is also depicted.

Unsurprisingly, as the AR is increased, the ions impinge the trench bottom with less energy. More precisely, due to the electrostatic repulsion, the ions are decelerating as they enter the trench. The larger the positive potential at the trench bottom is, the less energetic they will be when they impinge on it. This is clearly illustrated in figure 4.41.

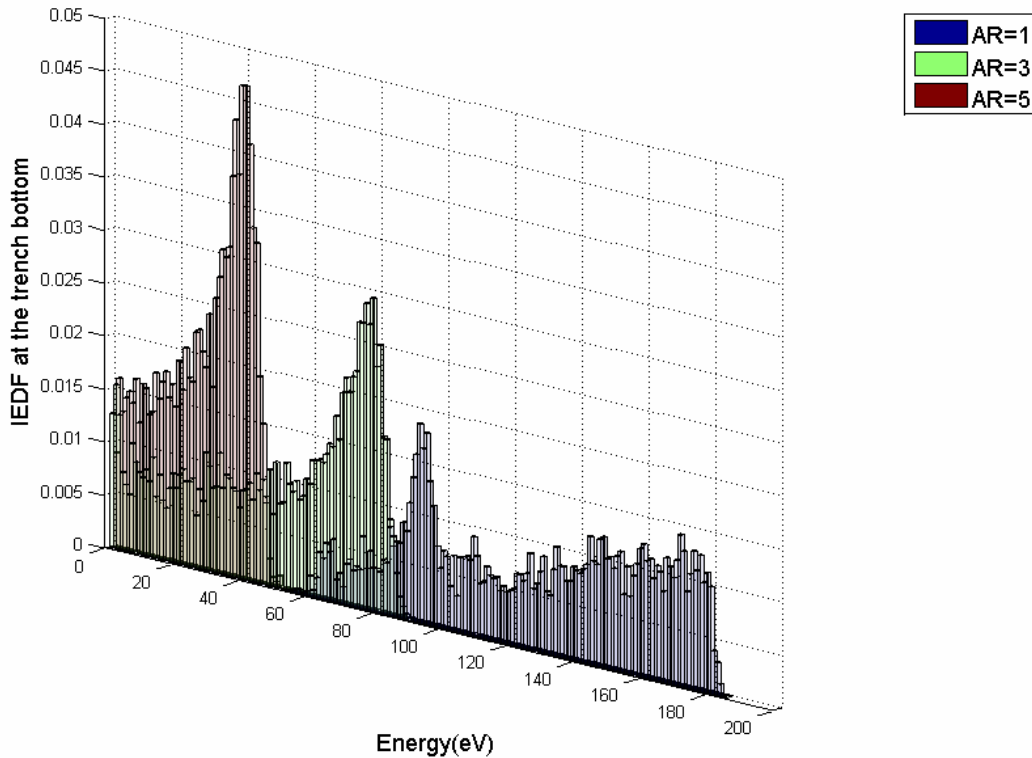


Figure 4.41: The energy distribution of ions arriving at the trench bottom as a function of the AR. The larger the AR is, the less energetic the impinging ions at the trench bottom will be.

In the following, figures 4.42, 4.44 and 4.46 shows the normalized etching yield along the dielectric surface. For each AR case, the etching yield at all positions is normalized by the maximum etching yield. The same applies for the etching rate, depicted on figures 4.43, 4.45 and 4.47. The etching yield and the etching rate calculated without taking consideration the charging effect are also presented at the same diagrams. The purpose is to compare all cases and see how charging affects the etching of the dielectric structure.

As it was anticipated from figure 4.40, the lowest etching rate is observed for the case where AR equals 5. Indeed, as the trench depth increases, the higher ion flux causes the build up of a larger bottom potential so that the ion and electron flux balance. Since the latter is heavily restricted by shadowing, it can be predicted that etching will not take place for larger AR structures.

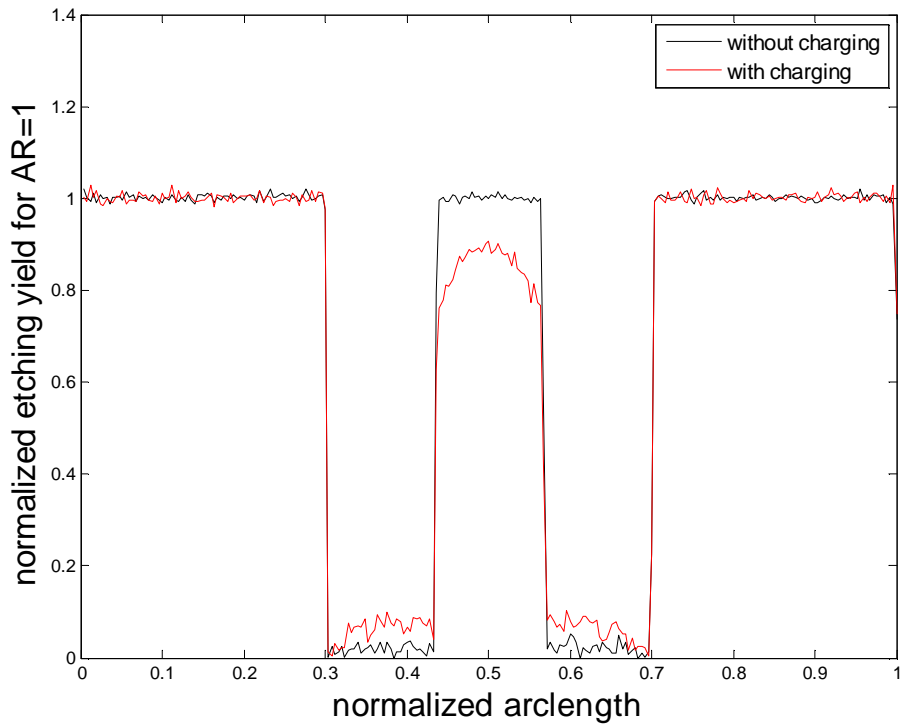


Figure 4.42: Normalized etching yield along the surface of structure for the AR=1 case. The respective no charging case is also depicted.

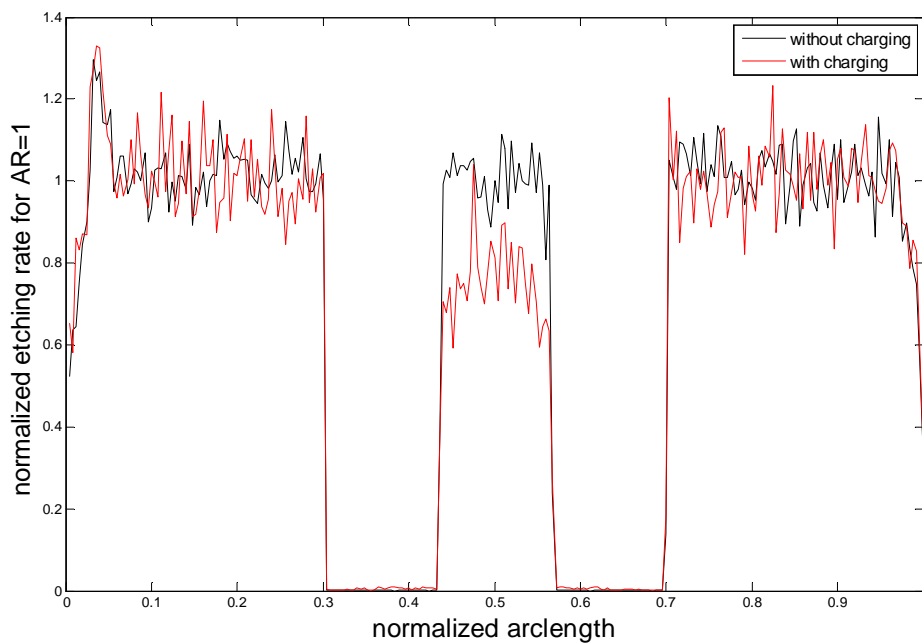


Figure 4.43: Normalized etching rate along the surface of structure for the AR=1 case. The respective no charging case is also depicted.

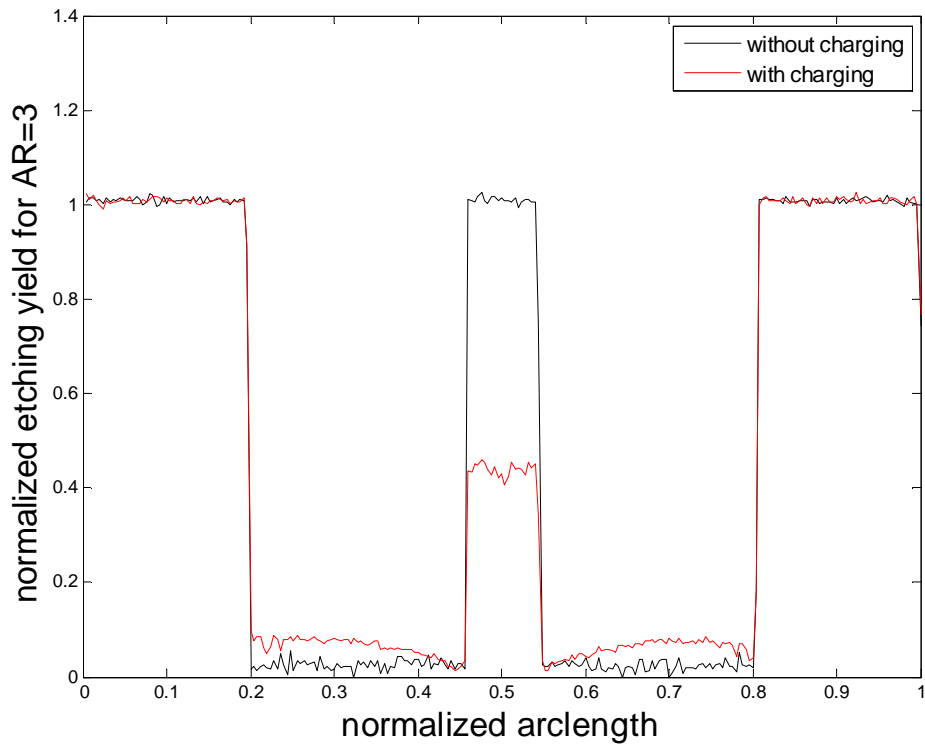


Figure 4.44: Normalized etching yield along the surface of structure for the AR=3 case. The respective no charging cases is also depicted.

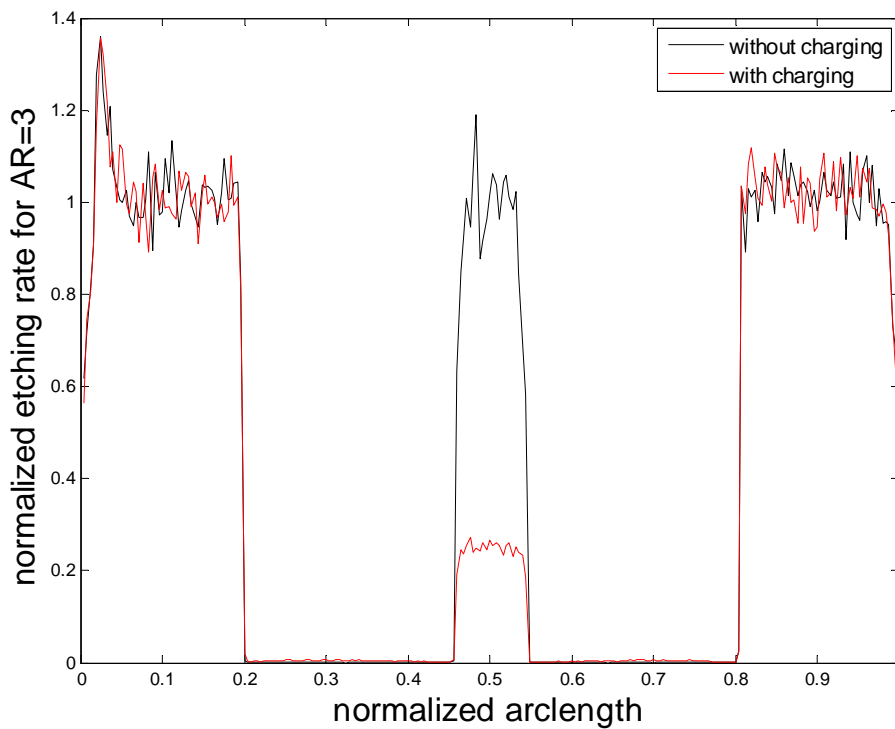


Figure 4.45: Normalized etching yield along the surface of structure for the AR=3 case. The no charging respective case is also depicted.

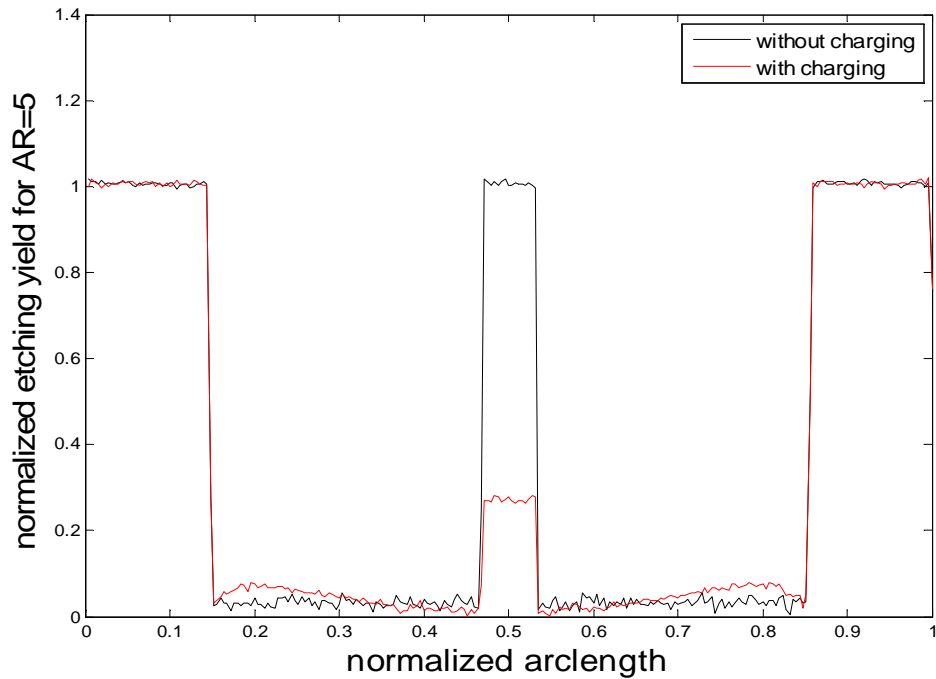


Figure 4.46: Normalized etching yield along the surface of structure for the AR=5 case. The no charging respective case is also depicted.

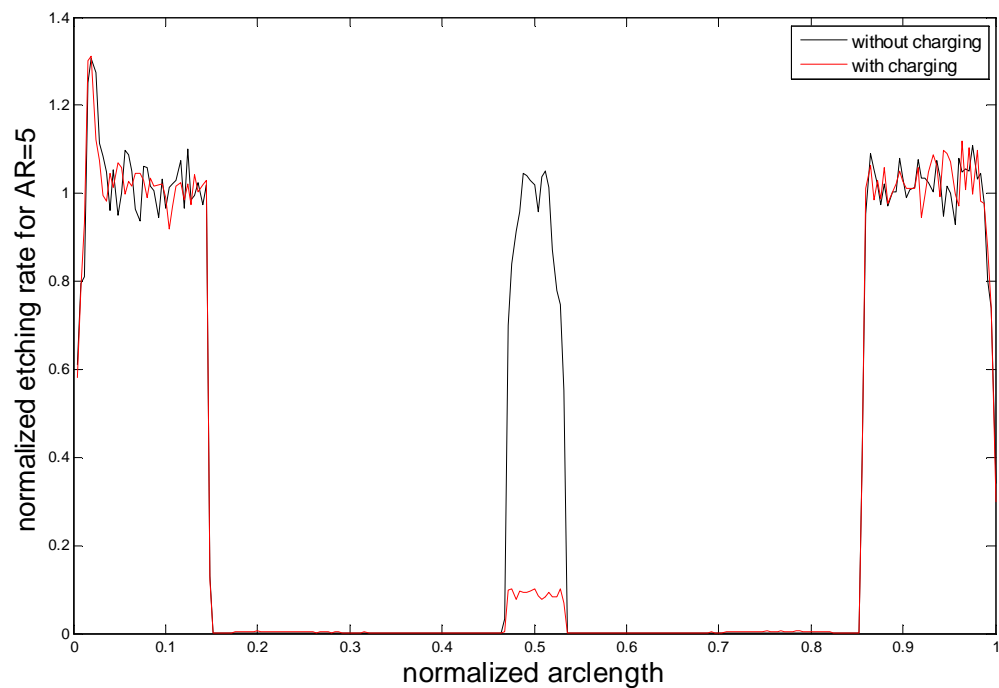


Figure 4.47: Normalized etching rate along the surface of structure for the AR=5 case. The no charging respective case is also depicted.

5 CONCLUSIONS AND FUTURE WORKS

5.1 Conclusions

We have developed a model for the simulation of surface charging on plasma "wetted" 2-dimensional (2d) microstructures. The model consists of three sub-models a) a particle trajectories calculation, b) a surface charge density, and c) charging potential model. The space potential calculated by the third sub-model is not only affected by the surface charge but it also affects it: the electric force coming from the potential affects the trajectory calculation in the first sub-model.

We examined the charging of dielectric trenches and analyzed how the electric potential and the ion energy distribution (at the bottom of a trench) depend on the initial ion energy distribution function (IEDF) shape, the average ion energy, the electron temperature (T_e) and also the trench aspect ratio (AR). We also calculated the charged local ion and electron fluxes inside the dielectric trench. Ultimately, based on a simple ion-enhanced etching model, the local etching yield and rate at each position on the trench surface were computed. In the following, we summarize our conclusions:

A) By gradually reducing the width of the bimodal IEDF and simultaneously holding the average ion energy constant (70 eV), the steady state charging potential at the trench bottom approaches the average ion energy (see Fig. 5.1). Besides, the total ion flux is not affected by the shape of the IEDF as the controlling factor of the process is the invariable (in all IEDF shape cases) electron flux. On the contrary, a wide IEDF results in a significantly larger (compared to the narrower IEDFs) average ion energy at the trench bottom. As far as the etching yield and rate is concerned, a narrower IEDF leads to a smaller etching rate (ER) at the trench bottom (see figure 5.2); an electric etch stop is predicted for the narrow bi-modal and mono-modal IEDF with an average ion energy of 70 eV.

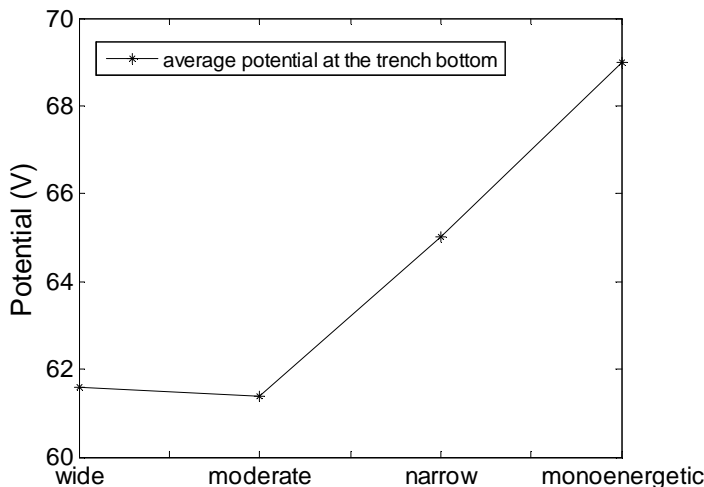


Figure 5.1: Average potential at the trench bottom as a function of the IEDF shape

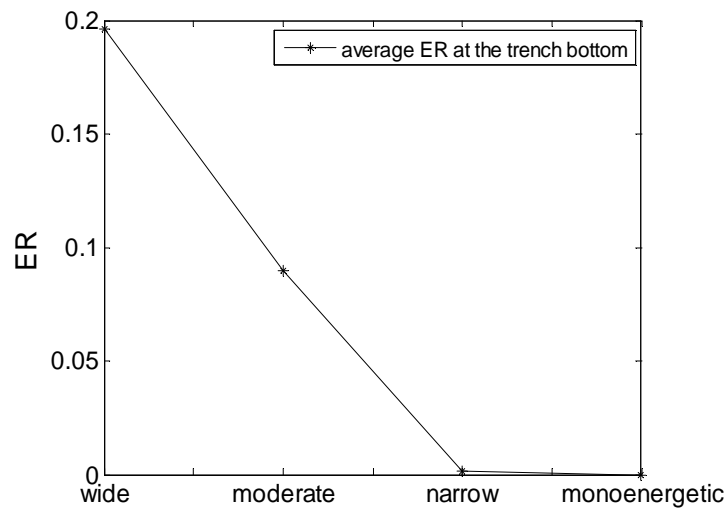


Figure 5.2: Average ER (normalized with respect to the value at open area) at the trench bottom as a function of the IEDF shape.

B) The results of the simulation show that the larger the average ion energy is (we investigated the cases of 70, 120, and 180 eV), the larger the steady state charging potential at the trench bottom will be (see Fig. 5.3). Besides, the total ion flux as well as etching yield and rate increase as the ion average energy increases (see Fig. 5.4).

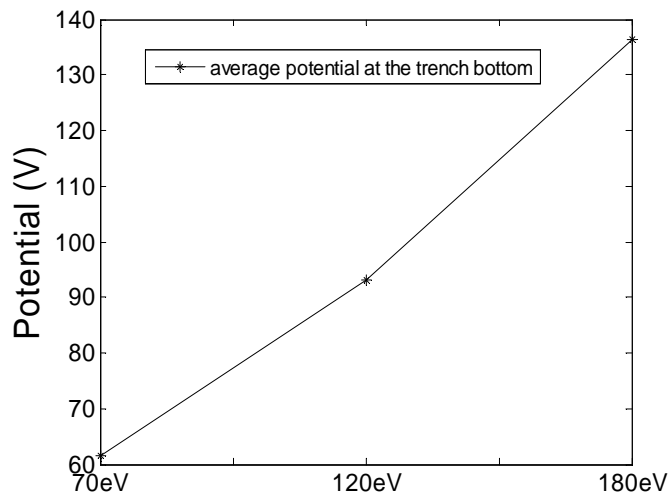


Figure 5.3: Average potential at the trench bottom as a function of the average ion energy.

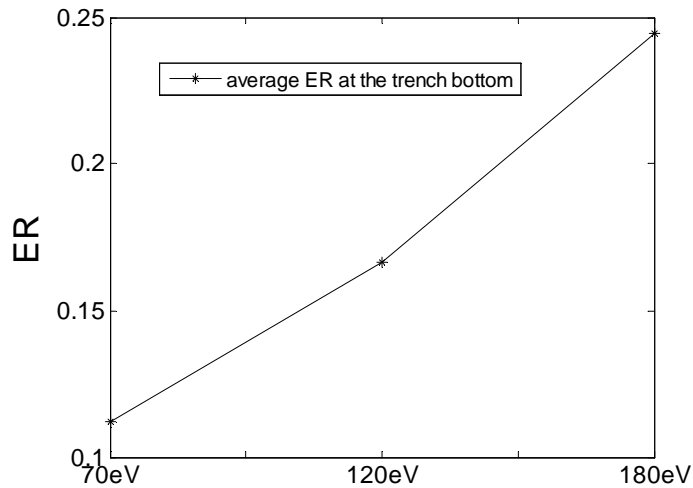


Figure 5.4: Average ER (normalized with respect to the value at open area) at the trench bottom as a function of the average ion energy.

C) The increase of T_e (we examined the cases of 2 eV, 4 eV, and 8 eV) is "added" to the shadowing effect and further reduces the electron flux at the trench bottom by making the potential at the trench entrance more negative. To balance ion and electron currents at the trench bottom, the charging potential at the bottom increases (see Fig. 5.5) so that the ion current is reduced by the same amount. The ion flux as well as the etching yield and rate (see Fig. 5.6) decreases when T_e increases.

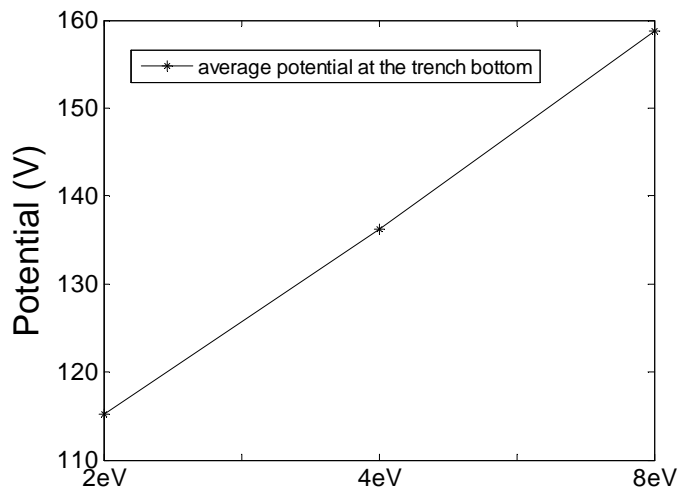


Figure 5.5: Average potential and at the trench bottom as a function of T_e .

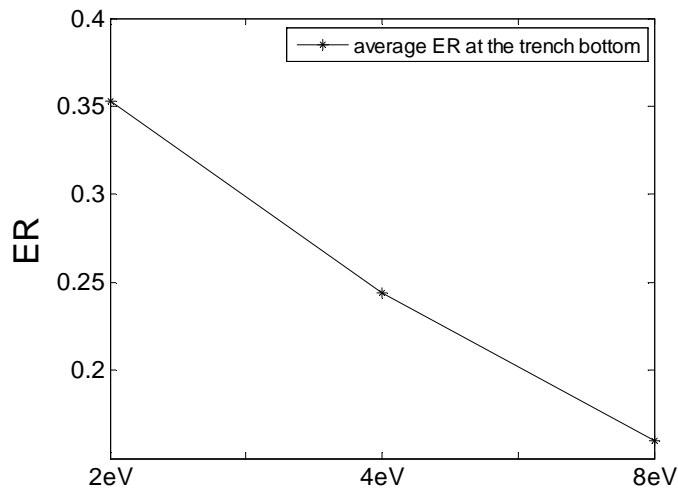


Figure 5.6: Average ER (normalized with respect to the value at open area) at the trench bottom as a function of T_e .

D) The increase of AR (we examined the cases of AR=1, AR=3, and AR=5) is "added" to the shadowing effect and further reduces the electron flux at the trench bottom by making the potential at the trench entrance more negative. To balance ion and electron currents at the trench bottom, the charging potential at the bottom increases (see Fig. 5.7) so that the ion current is reduced by the same amount. The ion flux as well as the etching yield and rate (see Fig. 5.8) decreases when AR increases.

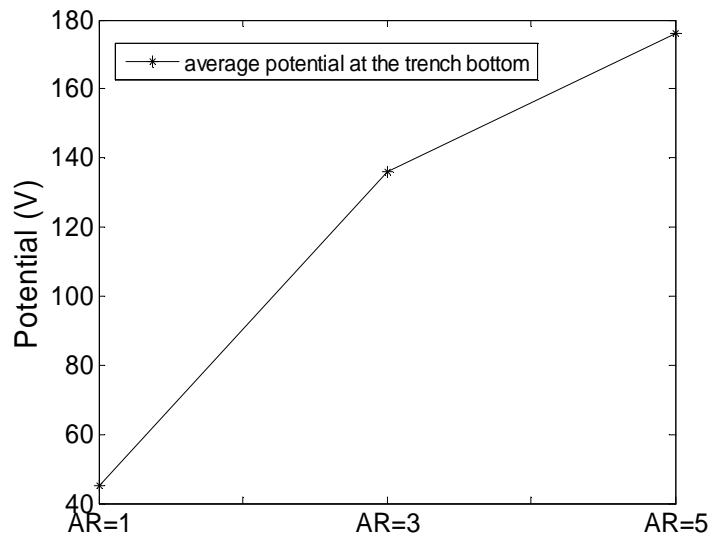


Figure 5.7: a) Average potential at the trench bottom as a function of the AR.

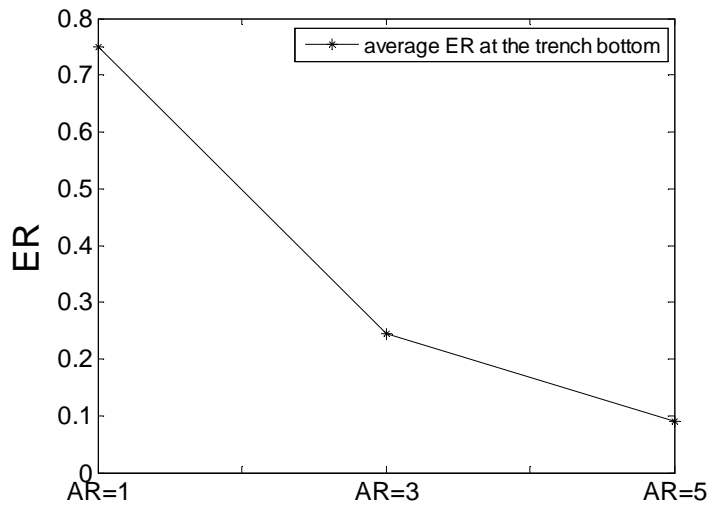


Figure 5.8: average ER (normalized with respect to the value at open area) at the trench bottom as a function of the AR.

5.2 Future work

The future work refers to both potential extensions and the potential applications of the model. The potential extensions of model are following:

A) The combination of the model with an available profile evolution algorithm based on the level set method [49]. This requires the acceleration of the calculations through parallel processing so as to have profile evolution results in realistic time scales.

B) The development of a sheath model [59] to produce coupled energy and angular distributions of ions and electrons.

C) The incorporation of the charging model into ϕ etch [42], i.e. an integrated simulation framework for feature profile evolution. This requires the development of source code instead of using Matlab and Comsol.

The potential applications of the model are following:

D) The combination of the charging model with a surface etching models for silicon oxide [60] or polymeric substrates.

E) Application of the model to random two dimensional (2d) surface morphologies in order to study the effect of charging on roughness formation and evolution on surfaces of insulating materials.

APPENDIX I

Acceptance-rejection method: It must be shown that Y is indeed distributed as F^{35} , i.e.

$$\begin{aligned} F(y) &= P(Y \leq y) \\ &= P(Y \leq y \mid U \leq \frac{f(Y)}{G(Y)}) \\ &= P(Y \leq y \mid \text{accept}). \end{aligned}$$

Now using Bayes' Theorem³⁶,

$$P(Y \leq y \mid \text{accept}) = \frac{P(\text{accept} \mid Y \leq y) \cdot P(Y \leq y)}{P(\text{accept})}. \quad (I.1)$$

Since U and Y are independent continuous random variables³⁷, the continuous version of the law of total probability³⁸ can be utilized. Namely, considering the denominator of equation (I.1) and conditioning on the value of Y ³⁹,

³⁵We call

$$P\{X \in (-\infty, x]\} = P\{X \leq x\} = \int_{-\infty}^x f(u)du$$

the cumulative distribution function (cdf) of X and write $F(x) = P\{X \leq x\}$.

³⁶ Mathematically, Bayes' theorem gives the relationship between the probabilities of A and B , $P(A)$ and $P(B)$, and the conditional probabilities of A given B and B given A , $P(A|B)$ and $P(B|A)$ respectively. By the way, a conditional probability is the probability that an event will occur, when another event is known to occur or to have occurred. In its most common form, Bayes' theorem is:

$$P(A \mid B) = \frac{P(A \cap B)}{P(B)} = \frac{P(B \mid A) \cdot P(A)}{P(B)}$$

³⁷ The joint distribution of (X, Y) can be described via a non negative joint density function $f(x, y)$ such that for any subset $A \subseteq \mathbb{R}^2$, $P((X, Y) \in A) = \iint_A f(x, y) dx dy$. If X and Y are independent random variables then $f(x, y) = f_x(x) \cdot f_y(y)$.

³⁸ When $\{B_i\}$ is a partition of the sample space $P(A) = \sum_i P(A \mid B_i) \cdot P(B_i)$. Suppose now X is a continuous random variable. For any $G \subseteq \mathbb{R}^2$, we have $P((X, Y) \in G) = \int_{\mathbb{R}} P((x, Y) \in G \mid X = x) \cdot f_x(x) \cdot dx$.

³⁹ The conditional pdf of Y given $X=x$ is defined by $f_{Y|X}(y \mid x) = \frac{f(x, y)}{f_x(x)}$. One must be careful

about the conditional probability such as $P(Y \leq a \mid X = x)$. Since $P(X=x)=0$ (for a continuous random variable X), the usual definition of conditional probability cannot be used (i.e. Bayes' theorem). Instead $P(Y \leq a \mid X = x) = \int_{-\infty}^a f_{Y|X}(y \mid x) \cdot dy$. Furthermore, if X and Y are independent

random variables then $f_{Y|X}(y \mid x) = \frac{f_x(x) \cdot f_y(y)}{f_x(x)} = f_y(y)$, thus $P(Y \leq a \mid X = x) = \int_{-\infty}^a f_y(y) \cdot dy$.

For the denominator of equation (I.1)

$$\begin{aligned}
 P(\text{accept}) &= P\left(U \leq \frac{f(Y)}{G(Y)}\right) \\
 &= P\left(U \leq \frac{f(Y)}{G(Y)} \mid Y = y\right) \\
 &= \int_a^b P\left(U \leq \frac{f(Y)}{G(Y)} \mid Y = y\right) \cdot g(y) \cdot dy \\
 &= \int_a^b P\left(U \leq \frac{f(y)}{G(y)} \mid Y = y\right) \cdot g(y) \cdot dy \\
 &= \int_a^b \left(\int_{-\infty}^{\frac{f(y)}{G(y)}} \text{pdf}_{U|Y} du \right) \cdot g(y) \cdot dy \\
 &= \int_a^b \left(\int_{-\infty}^{\frac{f(y)}{G(y)}} \frac{\text{pdf}_U \cdot g(y)}{g(y)} du \right) \cdot g(y) \cdot dy = \\
 &= \int_a^b \left(\int_0^{\frac{f(y)}{G(y)}} \text{pdf}_U \cdot du \right) \cdot g(y) \cdot dy
 \end{aligned}$$

Since $\text{pdf}_U=1$, it follows that

$$\begin{aligned}
 P(\text{accept}) &= \int_a^b \frac{f(y)}{G(y)} \cdot g(y) \cdot dy \\
 &= \frac{1}{\int_a^b G(y) dy} \int_a^b f(y) dy \\
 &= \frac{1}{\int_a^b G(y) dy} .
 \end{aligned}$$

For the numerator of equation (I.1)

Thus

$$P(Y \leq y \mid \text{accept}) = \frac{\frac{F(y)}{\int_a^b G(\xi) \cdot d\xi}}{1} = F(y)$$

as desired.

APPENDIX II

The magnitude and the number of superparticles: A study for the proper magnitude and number of the superparticles per charging step was conducted. The number of particles that used in total in all cases is $2.25 \cdot 10^{12}$ particles.

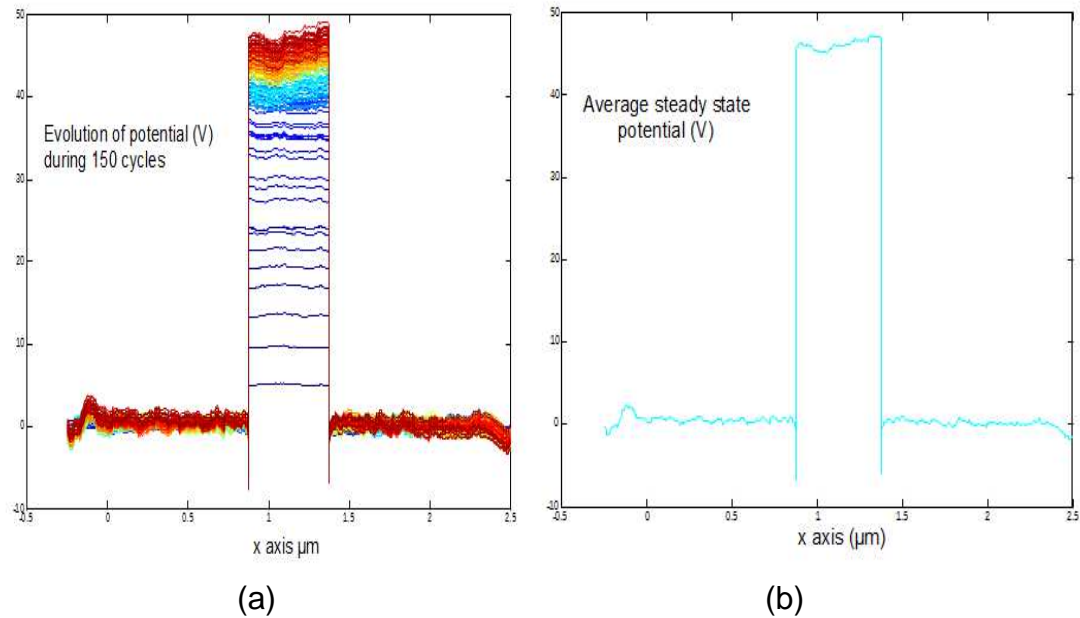


Figure II.1: a) Evolution and b) average steady state of charging potential. 1000 superparticles of ions and 1000 superparticles of electrons are released per step. The magnitude of a superparticle is $750 \cdot 10^3$ particles. Steady state is reached after 100 charging steps. The duration of simulation was 14.5 hours.

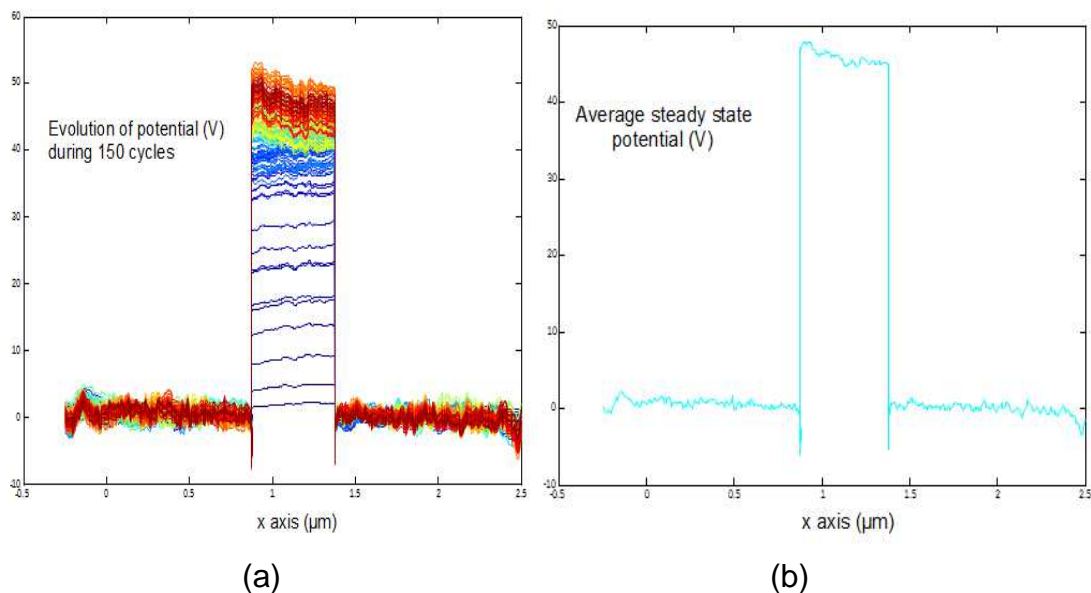


Figure II.2: a) Evolution and b) average steady state of charging potential. 250 superparticles of ions and 250 superparticles of electrons are released per step. The magnitude of a superparticle is $3000 \cdot 10^3$ particles. Steady state is reached after 50 charging steps. The duration of simulation was 4.5 hours.

Simulation of surface charging during plasma etching of dielectric microstructures

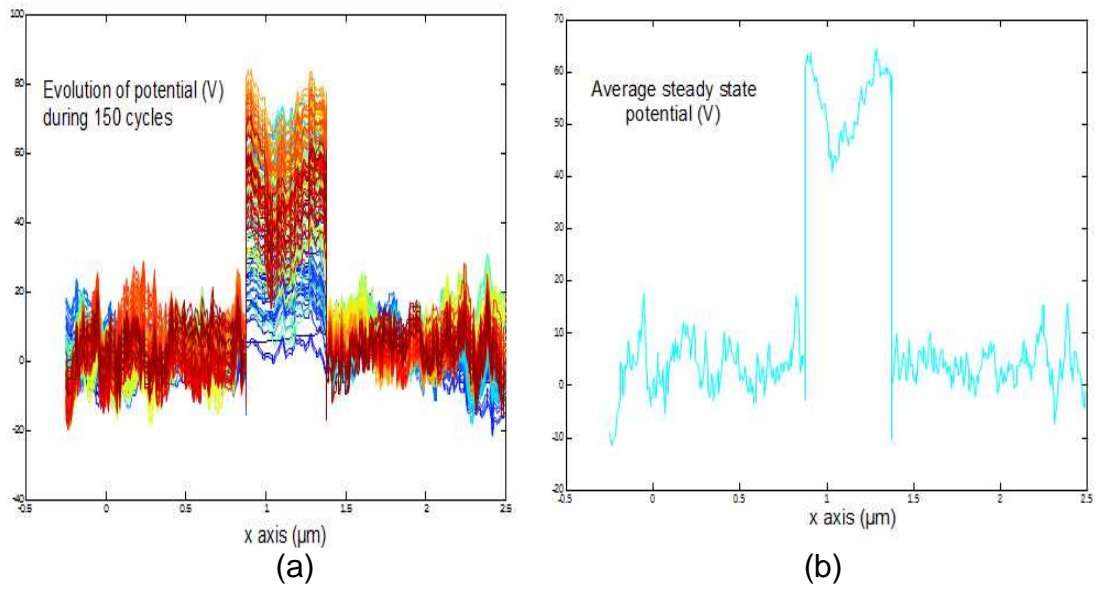


Figure II.3: a) Evolution and b) average steady state of charging potential. 10 superparticles of ions and 10 superparticles of electrons are released per step. The magnitude of a superparticle is $7.5 \cdot 10^7$ particles. Steady state is reached after 10 charging steps. The duration of simulation was 1 hour.

APPENDIX III

Algorithm for the particle distribution on the trench boundary: The boundary segment is represented by a vector in the two dimensional Cartesian space. Specifically, its components are equal to the differences $(xxi(i+1)-xxi(i), yyi(i+1)-yyi(i))$ or briefly (dx,dy) . Provided that the dot product of two vertical vectors must be zero, the components of the normal vector are $(-dy, dx)$.⁴⁰ (figure III.1).

Next, the vectors that represent the sides of the rectangle are calculated. Their positions are estimated by the following equations:

$$A1x = xxi(i) - n_x/2 \quad (III.1)$$

$$A1y = yyi(i) - n_y/2 \quad (III.2)$$

$$A2x = xxi(i) + n_x/2 \quad (III.3)$$

$$A2y = yyi(i) + n_y/2 \quad (III.4)$$

$$A4x = xxi(i+1) - n_x/2 \quad (III.5)$$

$$A4y = yyi(i+1) - n_y/2 \quad (III.6)$$

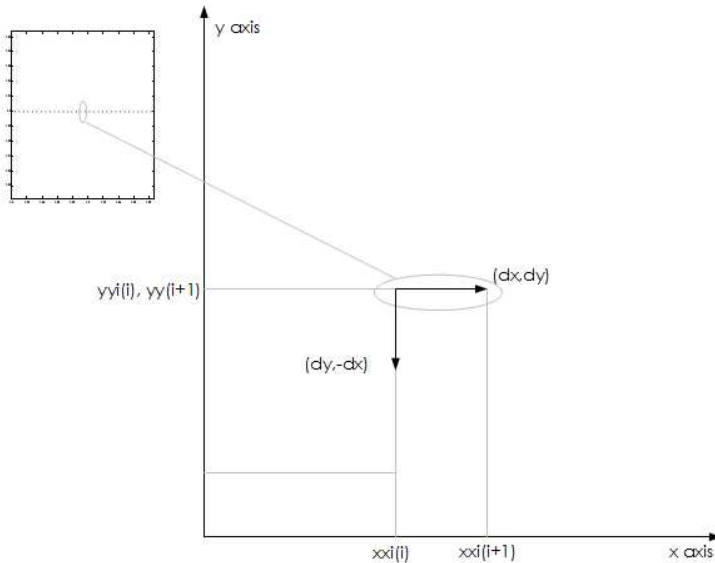


Figure III.1: Calculating the normal vector to the line segment $(xxi(i+1) - xxi(i), yyi(i+1) - yyi(i))$.

where n_x and n_y are the components of the normal vector multiplied by a constant equal to 4 (this constant defines the thickness of the boundary), thus $n_x = -4 \cdot dy$ and $n_y = 4 \cdot dx$. In figure III.2, \vec{r} and \vec{q} are the resulting vectors. In this way, a rectangle is determined. A particle is distributed to the segment if and

⁴⁰ $(dx,dy) \cdot (-dy,dx) = dx \cdot (-dy) + dy \cdot dx = 0$

only if it is inside this rectangle. The length of this rectangle, represented by \vec{r} , is specified by the above mentioned constant and can be changed by choosing a different constant value. Additionally, its width, determined by \vec{q} , is specified by the length of the segment.

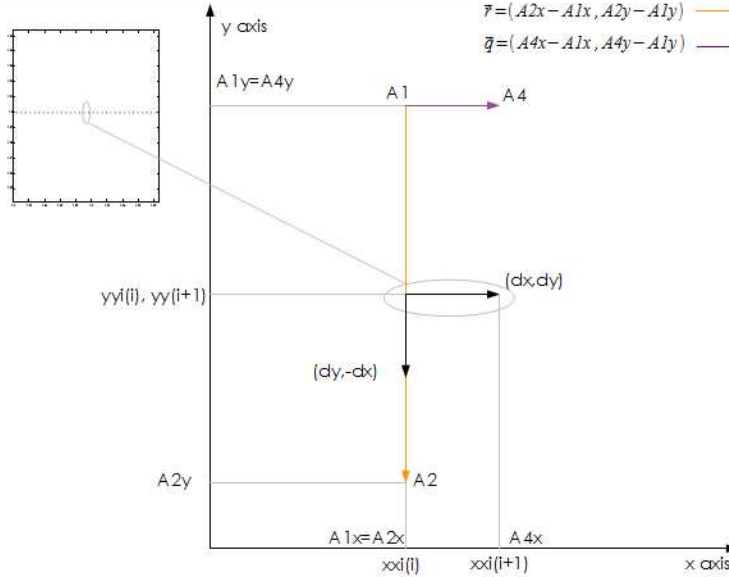


Figure III.2: Calculating the vectors of the parallelogram.

Assuming that the particle position is (q_x, q_y) , its position vector is determined by the following equation:

$$\vec{p} = (q_x - A1_x, q_y - A1_y) \quad (III.7)$$

Subsequently, the projection of \vec{p} to \vec{r} ⁴¹ and the projection of \vec{p} to \vec{q} ⁴² are investigated in order to verify if this particle is inside the parallelogram. More precisely, provided that

$$|\text{proj}_{\vec{r}} \vec{p}| \leq |\vec{r}| \quad (III.8)$$

and

$$|\text{proj}_{\vec{q}} \vec{p}| \leq |\vec{q}| \quad (III.9)$$

the particle is distributed to the segment. Otherwise, the particle is out of the parallelogram, thus, it is not distributed. This is clearly illustrated in the figure III.3.

⁴¹ $|\text{proj}_{\vec{r}} \vec{p}| = \frac{\vec{p} \cdot \vec{r}}{|\vec{r}|}$

⁴² $|\text{proj}_{\vec{q}} \vec{p}| = \frac{\vec{p} \cdot \vec{q}}{|\vec{q}|}$

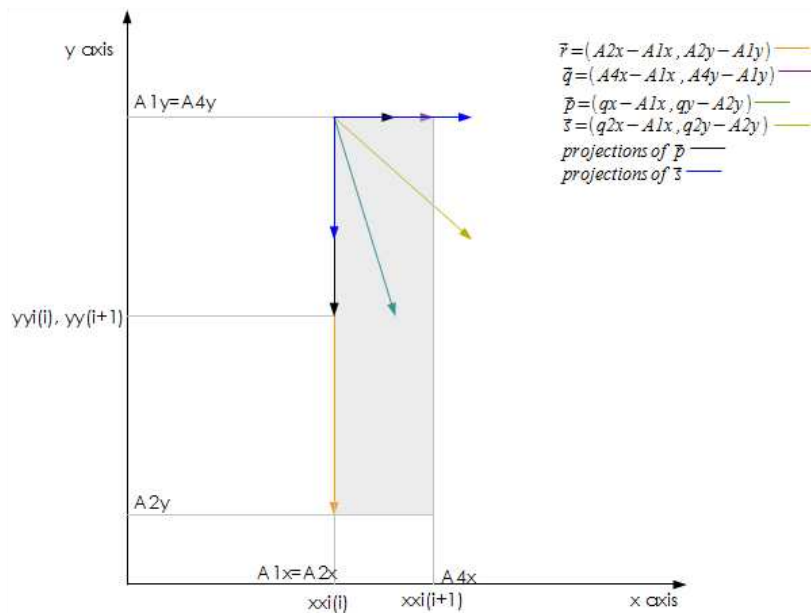


Figure III.3: Comparing the magnitude of positions vectors projection to \vec{r} and \vec{q} vectors with the magnitude of \vec{r} and \vec{q} vectors. Particle with position (q_x, q_y) is distributed to the segment. Particle with position (q_2x, q_2y) is not distributed to the segment.

Ultimately, for the sake of completeness, the application of the above mentioned method is presented for the case of an oblique segment. Particularly, the formation of the proper parallelogram in such a situation is illustrated.

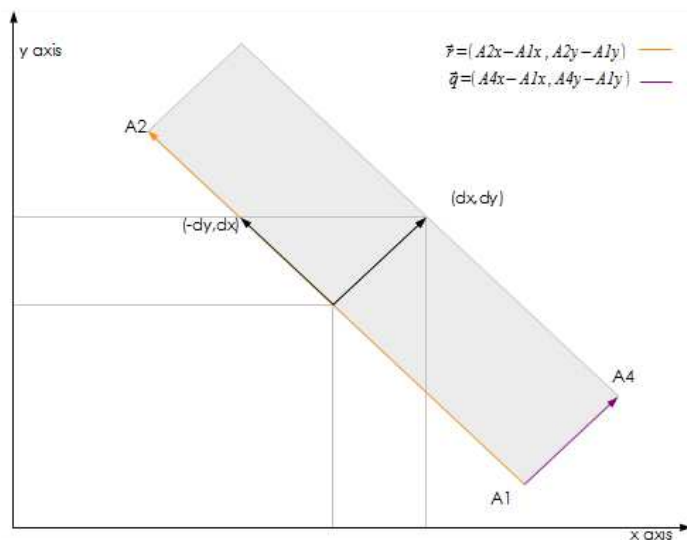


Figure III.4: Construction of the aforementioned parallelogram in the case of an oblique segment (dx, dy) .

APPENDIX IV

The finite element method: Comsol approximates the solution of the Laplace's equation with the utilization of the finite element method (FEM) [56]. One of the most important features of finite element method is that it is based on unstructured grids. This means that FEM is more flexible with respect to the geometry. For example, in two dimensions, the computational domain has not to be rectangular or something that can be mapped onto a rectangle (on the contrary, finite difference methods [56] use only structured grids).

The FEM methods basically split up the domain of the problem into small pieces, called elements, that have simple structure. A common approach for two-dimensional domains is to triangulate the domain into small triangles. The triangulation must be done in such a way that whenever two triangles touch, they will have either an entire common edge (and thus two common vertices) or just a common vertex. The reason for this is that the FEM approximate solution for the partial differential equation (PDE) will be made up of separate "pieces" on the various elements and they need to connect up (interpolate) together in a neat fashion.

Like finite difference methods, finite element methods will discretize the PDE into a linear system of equations. Thus, a FEM solution has the general form [61]

$$u_h(x, y) = \sum_j^N c_j \phi_j(x, y) \quad (\text{IV.1})$$

where c_j are coefficients and $\phi_j(x, y)$ are basis functions. The subscript h refers to the mesh that was used and is computed as the largest distance between two neighbouring points (a triangular element is consisted of three points (nodes)) in the mesh. The subscript j refers to the number of the mesh elements N . The coefficients c_j are found by solving the aforementioned linear system of equations. The most time-consuming step of the FEM is the construction of this linear system whose solution will give the values of the approximate solution. This process, known as "the assembly process," is broken up into an element-by-element computation involving the calculation of certain double integrals and (depending on the boundary data) line integrals.

So, the approximate solution, described by the equation (3.40), is found by restricting attention to a certain finite-dimensional space determined by basis functions corresponding to each of the elements. For two dimensional domains with triangulations, the type of basis function that turns out to be quite effective is linear functions. Over each element, the graph of such a basis function will be the triangular portion of a plane (sitting over the two-dimensional triangle). Mesh triangles that have common vertices or edges will have their graphs coinciding at common points. The resulting approximating functions will thus be continuous over the original domain.

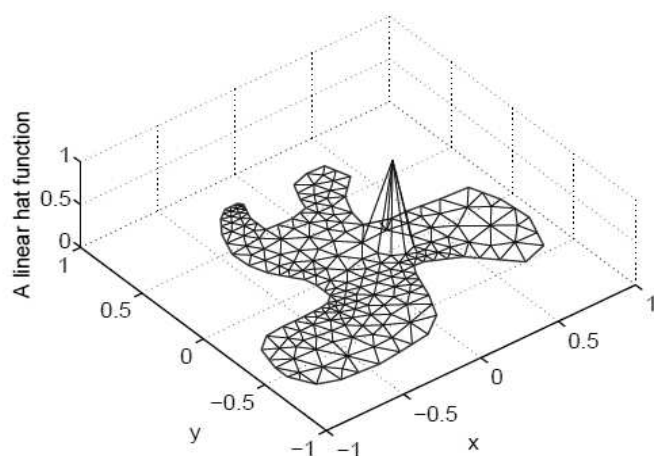


Figure IV.1: An example of an unstructured mesh and one basis function $\phi_j(x,y)$ are shown in the figures below. Basis functions can be of different types. The type shown above is called a linear hat function [61].

APPENDIX V

Comparison of Comsol results with the analytic solution of Laplace equation

The mathematical expression of the problem is

$$\nabla^2 V(x, y) = 0 \quad (V.1)$$

and the boundary conditions

$$\hat{n} \cdot \vec{D} \Big|_{y=0} = \sigma \quad (V.2)$$

$$u(x, b) = V_n = 100V \quad (V.3)$$

$$u(0, y) = 0 \quad (V.4)$$

$$u(a, y) = 0 \quad (V.5)$$

where $b=1\text{cm}$ (height of the rectangular) and $a=4\text{cm}$ (width of the rectangular). Using the method of separation of variables and the homogeneous conditions (V.4), (V.5) we come easily to the result

$$V(x, y) = \sum_{n=1}^{\infty} (A_n e^{\frac{n\pi}{a}y} + B_n e^{-\frac{n\pi}{a}y}) \sin \frac{n\pi}{a} x. \quad (V.6)$$

Using condition (V.2):

$$\sum_{n=1}^{\infty} \frac{n\pi}{a} (A_n - B_n) \sin\left(\frac{n\pi}{a} x\right) = \sum_{n=1}^{\infty} C_n \sin\left(\frac{n\pi}{a} x\right) = -\frac{\sigma}{\epsilon_0 \epsilon_r}, \quad (V.7)$$

where⁴³

$$C_n = \frac{2}{a} \int_0^a \left(-\frac{\sigma}{\epsilon_0 \epsilon_r}\right) \sin\left(\frac{n\pi}{a} x\right) dx = \frac{2\sigma}{\epsilon_0 \epsilon_r n\pi} [\cos(n\pi) - 1]. \quad (V.8)$$

Hence,

$$(A_n - B_n) = \frac{2\sigma\alpha}{\epsilon_0 \epsilon_r n\pi} [\cos(n\pi) - 1]. \quad (V.9)$$

⁴³ Multiply equation (V.7) by $\sin(n' \frac{\pi x}{a})$, where n' is a positive integer, and integrate from 0 to

a. It should be mentioned that $\int_0^a \sin\left(\frac{n\pi x}{a}\right) \cdot \sin\left(\frac{n'\pi x}{a}\right) dx = \begin{cases} 0, & \text{if } n' \neq n \\ \frac{a}{2}, & \text{if } n'=n \end{cases}$.

Condition (V.3) gives:

$$\begin{aligned}
 V(x,b) = V_n &= \sum_{n=1}^{\infty} (A_n e^{\frac{n\pi}{\alpha} b} + B_n e^{-\frac{n\pi}{\alpha} b}) \sin \frac{n\pi}{\alpha} x \\
 &= \sum_{n=1}^{\infty} \left\{ A_n e^{\frac{n\pi}{\alpha} b} + \left[A_n - \frac{2\sigma\alpha}{\epsilon_0 \epsilon_r n\pi} [\cos(n\pi) - 1] \right] e^{-\frac{n\pi}{\alpha} b} \right\} \sin \frac{n\pi}{\alpha} x \\
 &= \sum_{n=1}^{\infty} \left\{ 2 \cdot A_n \cosh\left(\frac{n\pi}{\alpha} b\right) - \frac{2\sigma\alpha}{\epsilon_0 \epsilon_r n\pi} [\cos(n\pi) - 1] e^{-\frac{n\pi}{\alpha} b} \right\} \sin \frac{n\pi}{\alpha} x \\
 &= \sum_{n=1}^{\infty} D_n \sin\left(\frac{n\pi}{\alpha} x\right), \tag{V.10}
 \end{aligned}$$

where

$$D_n = \frac{2}{a} \int_0^a V_n \sin\left(\frac{n\pi}{\alpha} x\right) dx = -\frac{2V_n}{n\pi} [\cos(n\pi) - 1]. \tag{V.11}$$

It yields

$$\begin{aligned}
 2 \cdot A_n \cosh\left(\frac{n\pi}{\alpha} b\right) - \frac{2\sigma\alpha}{\epsilon_0 \epsilon_r n\pi} [\cos(n\pi) - 1] e^{-\frac{n\pi}{\alpha} b} &= -\frac{2V_n}{n\pi} [\cos(n\pi) - 1] \Rightarrow \\
 A_n &= \frac{1}{2 \cosh\left(\frac{n\pi}{\alpha} b\right)} [\cos(n\pi) - 1] \left(\frac{2\sigma\alpha}{\epsilon_0 n^2 \pi^2} e^{-\frac{n\pi}{\alpha} b} - \frac{2V_n}{n\pi} \right) \tag{V.12}
 \end{aligned}$$

Using (V.12) and (V.9) :

$$B_n = [\cos(n\pi) - 1] \cdot \left[\frac{1}{2 \cosh\left(\frac{n\pi}{\alpha} b\right)} \left(\frac{2\sigma\alpha}{\epsilon_0 \epsilon_r n^2 \pi^2} e^{-\frac{n\pi}{\alpha} b} - \frac{2V_n}{n\pi} \right) - \frac{2\sigma\alpha}{\epsilon_0 \epsilon_r n^2 \pi^2} \right] \tag{V.13}$$

Finally, with the utilization of (V.6), (V.12) και (V.13) the potential in the domain is given by the expression :

$$V(x,y) = \sum_{n=1}^{\infty} [\cos(n\pi) - 1] \cdot \left[\frac{2 \cosh\left(\frac{n\pi}{\alpha} y\right)}{\cosh\left(\frac{n\pi}{\alpha} b\right)} \left(\frac{\sigma\alpha}{\epsilon_0 n^2 \pi^2} e^{-\frac{n\pi}{\alpha} b} - \frac{V_n}{n\pi} \right) - \frac{2\sigma\alpha}{\epsilon_0 n^2 \pi^2} e^{-\frac{n\pi}{\alpha} b} \right] \sin\left(\frac{n\pi}{\alpha} x\right) \tag{V.14}$$

Assuming $\sigma=1\text{C/m}^2$, the potential in the center of the rectangular is :

5.09114*10⁸V. This result is in good agreement with that obtained from comsol simulation. Particularly, Comsol, for the same point and using extremely fine mesh, gives 5.08873*10⁸ V.

Simulation of surface charging during plasma etching of dielectric microstructures

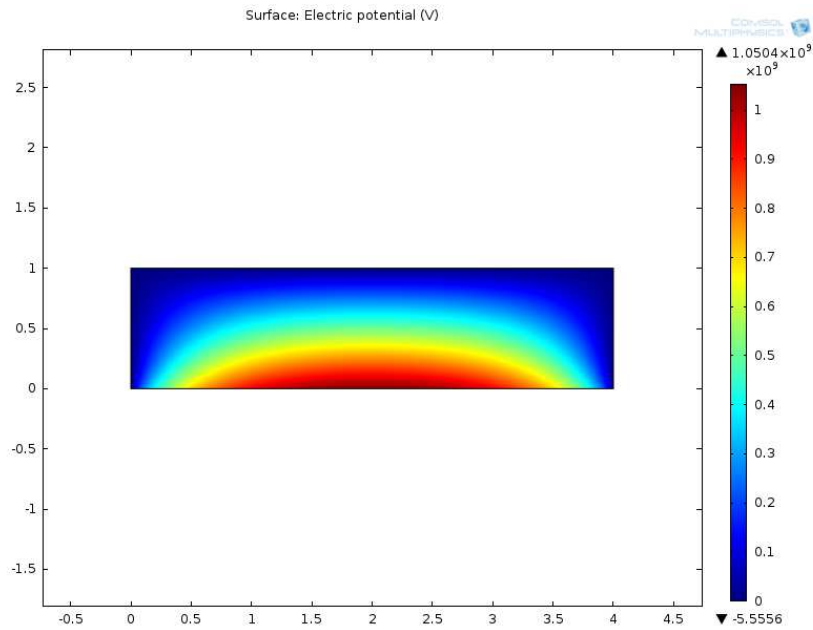


Figure V.1: Electric potential in the rectangular domain calculated with comsol. The Laplace equation is solved, subjected to mixed boundary conditions.

REFERENCES

- [1] S. M. S. C. Y. Chang, "*Ulsi Technology*," McGraw-Hill, pp. 329-330, 1996.
- [2] A. Piel, "*Plasma Physics: An Introduction to Laboratory, Space, and Fusion Plasmas*," Springer, pp. 1-43, 2010.
- [3] G. Kokkoris, "Ολοκληρωμένη προσομοίωση εξέλιξης τοπογραφίας κατά την εγχάραξη μικρο- και νανο-δομών με πλάσμα," 2005.
- [4] B. Chapman, "*Glow Discharge Processes*," John Wiley & Sons, pp. 49-74, 139-172, 1980.
- [5] U. S. Inan; and M. Gołkowski, "*Principles of Plasma Physics for Engineers and Scientists* ", Cambridge University Press, pp. 1-19, 2011.
- [6] http://en.wikipedia.org/wiki/Moore%27s_law.
- [7] A. J. L. Michael A. Lieberman, "*Principles of Plasma Discharges and Materials Processing*", John Wiley & Sons, p. 2, 2005.
- [8] B. R. Rogers and T. S. Cale, "Plasma processes in microelectronic device manufacturing," *Vacuum*, vol. 65, pp. 267-279, 2002.
- [9] G. Kokkoris, "Etching of open area surfaces. Mechanism and modeling," pp. 3-6, 2012.
- [10] J. W. Coburn and H. F. Winters, "Plasma-assisted etching in microfabrication," *Annual Review of Materials Science*, vol. 13, pp. 91-116, 1983.
- [11] T. G. Madziwa-Nussinov, D. Arnush, and F. F. Chen, "Ion orbits in plasma etching of semiconductors," *Physics of Plasmas*, vol. 15, 2008.
- [12] G. S. Hwang and K. P. Giapis, "On the origin of the notching effect during etching in uniform high density plasmas," *Journal of Vacuum Science and Technology B: Microelectronics and Nanometer Structures*, vol. 15, pp. 70-87, 1997.
- [13] G. S. Hwang and K. P. Giapis, "The influence of mask thickness on charging damage during overetching," *Journal of Applied Physics*, vol. 82, pp. 572-577, 1997.
- [14] J. C. Arnold and H. H. Sawin, "Charging of pattern features during plasma etching," *Journal of Applied Physics*, vol. 70, pp. 5314-5317, 1991.
- [15] G. S. Hwang and K. P. Giapis, "Aspect ratio independent etching of dielectrics," *Applied Physics Letters*, vol. 71, pp. 458-460, 1997.
- [16] J. Matsui, K. Maeshige, and T. Makabe, "Effect of aspect ratio on topographic dependent charging in oxide etching," *Journal of Physics D: Applied Physics*, vol. 34, pp. 2950-2955, 2001.
- [17] H. S. Park, S. J. Kim, Y. Q. Wu, and J. K. Lee, "Effects of plasma chamber pressure on the etching of micro structures in SiO₂ with the charging effects," *IEEE Transactions on Plasma Science*, vol. 31, pp. 703-710, 2003.
- [18] K. P. Giapis and G. S. Hwang, "Pattern-dependent charging and the role of electron tunneling," *Japanese Journal of Applied Physics, Part 1: Regular Papers and Short Notes and Review Papers*, vol. 37, pp. 2281-2290, 1998.
- [19] V. Ishchuk, B. E. Volland, M. Hauguth, M. Cooke, and I. W. Rangelow, "Charging effect simulation model used in simulations of plasma etching of silicon," *Journal of Applied Physics*, vol. 112, 2012.
- [20] H. Morioka, D. Matsunaga, and H. Yagi, "Suppression of notching by lowering the bias frequency in electron cyclotron resonance plasma with a divergent magnetic field," *Journal of Vacuum Science and Technology A: Vacuum, Surfaces and Films*, vol. 16, pp. 1588-1593, 1998.
- [21] M. Schaepkens and G. S. Oehrlein, "Asymmetric microtrenching during inductively coupled plasma oxide etching in the presence of a weak magnetic field," *Applied Physics Letters*, vol. 72, pp. 1293-1295, 1998.
- [22] R. A. Gottscho and C. W. Jurgensen, "Microscopic uniformity in plasma etching," *Vacuum Science & Technology B: Microelectronics and Nanometer Structures*, vol. 10, pp. 2133-2147, 1992.
- [23] "http://www.eng.nus.edu.sg/EResnews/0410/rd/rd_8.html."
- [24] T. Kinoshita, M. Hane, and J. P. McVittie, "Notching as an example of charging in uniform high density plasmas," *Journal of Vacuum Science and Technology B: Microelectronics and Nanometer Structures*, vol. 14, pp. 560-565, 1996.
- [25] K. P. Giapis, G. S. Hwang, and O. Joubert, "The role of mask charging in profile evolution and gate oxide degradation," *Microelectronic Engineering*, vol. 61-62, pp. 835-847, 2002.

- [26] G. S. Hwang and K. P. Giapis, "Pattern-dependent charging in plasmas: Electron temperature effects," *Physical Review Letters*, vol. 79, pp. 845-848, 1997.
- [27] G. S. Hwang and K. P. Giapis, "Ion mass effect in plasma-induced charging," *Applied Physics Letters*, vol. 71, pp. 1942-1944, 1997.
- [28] G. S. Hwang and K. P. Giapis, "On the link between electron shadowing and charging damage," *Journal of Vacuum Science and Technology B: Microelectronics and Nanometer Structures*, vol. 15, pp. 1839-1842, 1997.
- [29] G. S. Hwang and K. P. Giapis, "Aspect-ratio-dependent charging in high-density plasmas," *Journal of Applied Physics*, vol. 82, pp. 566-571, 1997.
- [30] G. S. Hwang and K. P. Giapis, "Prediction of multiple-feature effects in plasma etching," *Applied Physics Letters*, vol. 70, pp. 2377-2379, 1997.
- [31] G. S. Hwang and K. P. Giapis, "The influence of electron temperature on pattern-dependent charging during etching in high-density plasmas," *Journal of Applied Physics*, vol. 81, pp. 3433-3439, 1997.
- [32] G. S. Hwang and K. P. Giapis, "The influence of surface currents on pattern-dependent charging and notching," *Journal of Applied Physics*, vol. 84, pp. 683-689, 1998.
- [33] A. P. Palov, Y. A. Mankelevich, T. V. Rakhimova, and D. Shamiryan, "Charging of Submicron Structures during Silicon Dioxide Etching in One- and Two-Frequency Gas Discharges," *Plasma Physics Reports*, vol. 36, pp. 891-901, 2010.
- [34] M. F. Doemling, N. R. Rueger, and G. S. Oehrlein, "Observation of inverse reactive ion etching lag for silicon dioxide etching in inductively coupled plasmas " *Applied Physics Letters* vol. 68, pp. 10 - 12 1996.
- [35] J. A. Kenney and G. S. Hwang, "Prediction of stochastic behavior in differential charging of nanopatterned dielectric surfaces during plasma processing," *Journal of Applied Physics*, vol. 101, 2007.
- [36] B. M. Radjenović, M. D. Radmilović-Radjenović, and Z. L. Petrović, "Dynamics of the profile charging during SiO₂ etching in plasma for high aspect ratio trenches," *IEEE Transactions on Plasma Science*, vol. 36, pp. 874-875, 2008.
- [37] M. Radmilović-Radjenović, B. Radjenović, and M. Savić, "The surface charging effects in three-dimensional simulation of the profiles of plasma-etched nanostructures," *International Journal of Numerical Modelling: Electronic Networks, Devices and Fields*, vol. 24, pp. 535-544, 2011.
- [38] S. Q. Zhang, Z. L. Dai, Y. H. Song, and Y. N. Wang, "Effect of reactant transport on the trench profile evolution for silicon etching in chlorine plasmas," *Vacuum*, vol. 99, pp. 180-188, 2014.
- [39] <http://www.mathworks.com/products/matlab/>.
- [40] <http://www.comsol.com/>
- [41] <http://nessie.imel.demokritos.gr>.
- [42] <http://www.phietch.org/>
- [43] W. D. W. Stephen M. Rosnagel , Jerome J. Cuomo "Handbook of Plasma Processing Technology: Fundamental, Etching, Deposition and Surface Interactions (Materials Science and Process Technology)," *Noyes Publications*, pp. 58-66, 1990.
- [44] J. P. C. Francis F. Chen, "*Principles of plasma processing*," Plenum/Kluwer Publishers, pp. 31-47, 2002.
- [45] P. Chabert and N. Braithwaite, "*Physics of Radio-Frequency Plasmas*," Cambridge University Press, pp. 96-130, 2011.
- [46] S. Chapra, "*Applied Numerical Methods with MATLAB: for Engineers & Scientists*," McGraw-Hill Science, 2011.
- [47] A. R. M. Wendy L. Martinez, "*Computational Statistics Handbook with MATLAB®*," Chapman & Hall/CRC, 2002.
- [48] S. Osher and R. Fedkiw, "*Level Set Methods and Dynamic Implicit Surfaces* " Springer, 2003.
- [49] G. Kokkoris, A. Tserepi, A. G. Boudouvis, and E. Gogolides, "Simulation of SiO₂ and Si feature etching for microelectronics and microelectromechanical systems fabrication: A combined simulator coupling modules of surface etching, local flux calculation, and profile evolution," *Journal of Vacuum Science and Technology A: Vacuum, Surfaces and Films*, vol. 22, pp. 1896-1902, 2004.
- [50] C. K. Birdsall and A. B. Langdon, "*Plasma Physics via Computer Simulation*," Taylor & Francis, 2004.

- [51] Z. Zhao, Z. Dai, and Y. Wang, "Feature profile evolution during etching of SiO₂ in radio-frequency or direct-current plasmas," *Plasma Science and Technology*, vol. 14, pp. 64-70, 2012.
- [52] <http://www.comsol.com/livelink-for-matlab>.
- [53] E. Kawamura, V. Vahedi, M. A. Lieberman, and C. K. Birdsall, "Ion energy distributions in rf sheaths; review, analysis and simulation," *Plasma Sources Science and Technology*, vol. 8, pp. R45-R64, 1999.
- [54] V. Georgieva and A. Bogaerts, "Negative ion behavior in single- and dual-frequency plasma etching reactors: Particle-in-cell/Monte Carlo collision study," *Physical Review E - Statistical, Nonlinear, and Soft Matter Physics*, vol. 73, 2006.
- [55] D. J. Griffiths, "Introduction to Electrodynamics," Addison Wesley, 1999.
- [56] A. Stanoyevitch, "Introduction to Numerical Ordinary and Partial Differential Equations Using MATLAB," Wiley-Interscience, 2005.
- [57] A. Metze, D. W. Ernie, and H. J. Oskam, "The energy distribution of ions bombarding electrode surfaces in rf plasma reactors," *Journal of Applied Physics*, vol. 65, pp. 993-998, 1989.
- [58] D. Gahan, S. Daniels, C. Hayden, P. Scullin, D. O'Sullivan, Y. T. Pei, *et al.*, "Ion energy distribution measurements in rf and pulsed dc plasma discharges," *Plasma Sources Science and Technology*, vol. 21, 2012.
- [59] M. A. Lieberman, "Analytical solution for capacitive rf sheath," *IEEE Transactions on Plasma Science*, vol. 16, pp. 638-644, 1988.
- [60] E. Gogolides, P. Vauvert, G. Kokkoris, G. Turban, and A. G. Boudouvis, "Etching of SiO₂ and Si in fluorocarbon plasmas: A detailed surface model accounting for etching and deposition," *Journal of Applied Physics*, vol. 88, pp. 5570-5584, 2000.
- [61] "http://www.it.uu.se/. Lab Introduction to Finite Element Methods and COMSOL Multiphysics. Using a finite element method to compute the shape of a soap film."